TECHNISCHE UNIVERSITÄT MÜNCHEN

WALTHER-MEISSNER-INSTITUT

BAYERISCHE AKADEMIE DER WISSENSCHAFTEN

Distribution of quantum states in a microwave local area network

Master's Thesis

Simon Gandorfer

Supervisor: Prof. Dr. Rudolf Gross

Advisor: Dr. Kirill Fedorov

November 3, 2022

Contents

Chapter 1

Introduction

Within the last couple of decades, the development of quantum information science gave rise to many novel and active fields of research. These fields are unified by a common goal to exploit fundamental properties imposed by quantum mechanics, such as superposition or quantum entanglement, in order to achieve a quantum advantage in solution of various practical problems. For example, this advantage can come in the form of an unconditional security, in the case of quantum cryptography and quantum communication [1, 2], or in the form of an ability to deal with classically-unsolvable problem, in the case of quantum computing [3]. In order to experimentally implement these concepts, various physical platforms must be developed. While each platform has its own advantages and disadvantages, superconducting circuits operating in the quantum regime are a particularly promising platform, especially due to the recent advances with superconducting quantum information processors with few tens of quantum bits [4].

Experimental applications of the superconducting circuits are not limited to quantum bits - they also can be used for generation and investigations of quantum microwave radiation. Here, state-of-the-art experiments have demonstrated successful applications of propagating microwaves as carriers of quantum information, for example, in secure communication with remote state preparation [5], quantum teleportation [6], or quantum key distribution [7]. This entire field is of great importance with respect to future quantum communication between superconducting quantum processors. The absence of frequency conversion losses due to the natural frequency match between the propagating microwaves and the superconducting quantum processors can be the decisive factor especially in local area networks. However, despite many advantages of utilizing the microwave regime for quantum information processing, experimental implementations hold many challenges. First of all, the employed superconducting circuits require cryogenic operation temperatures, typically, below 10 Kelvin, to be in the superconducting state. Moreover, comparatively low energies of microwave photons in the gigahertz range imply the requirement of even lower temperatures around a few tens of millikelvin in order to avoid excessive thermal noise. Furthermore, the low energies of microwave photons makes their detection a challenging task. The lack of efficient single-photon detectors in the microwave regime requires us to amplify the weak microwave signals with a chain of linear amplifiers before conversion into digital signals. State-of-the-art commercially available semiconductor-based microwave amplifiers, such as cryogenic high-electron-mobility transistors (HEMTs), inevitably add 10-20 noise photons to the incoming signal. This makes the task of quantum tomography of microwave states with very few photons quite challenging. Here, superconducting parametric amplifiers are extremely important and useful [3]. These amplifiers provide access to the quantum-limited noise performance, corresponding to 0.5 added noise photons in the phase-insensitive regime.

First proposals for parametric amplifiers based on the nonlinear inductance of Josephson junctions date back to the early 1980s [8]. By the end of that decade, Josephson junction-based amplification reaching the near quantum-limited performance was demonstrated for the first time by Bernard Yurke *et al.* [9, 10]. In the early 2000s, with a renewed interest stemming from the field of circuit quantum electrodynamics (c-QED) [11–13], microwave quantum-limited amplification became the basis for many applications, such as single-shot qubit readout. Over the last couple of years, flux-driven JPAs [14, 15] have seen extensive use in various different fields of research, including, but not limited to, high-fidelity qubit readout [16], generation of squeezed microwave fields [17], or as sources of quantum entanglement in continuous-variable systems [18]. However, despite of years of improvements, Josephson-based amplifiers struggled to overcome bandwidth, gain, and compression limitations imposed by the original resonator paradigm. These issues have strongly motivated the development of superconducting traveling wave parametric amplifier (TWPA) devices in the microwave regime. These TWPAs make use of resonator-free geometries with distributed nonlinear elements and are able to overcome the gain-bandwidth limit of the resonator-based JPAs.

In this thesis, we experimentally measure and compare flux-driven JPA designs with a superconducting TWPA device in the context of their nondegenerate gain and bandwidth, 1 dB-compression point, and ability to create squeezed states. For the quantum state tomography of these squeezed states of light, an accurate calibration of the system's amplification chain is of utmost importance. To this end, we introduce a so-called two-dimensional Planck spectroscopy. It improves the existing calibration techniques based on the black-body radiation approach [19] and provides an *in-situ* access to microwave losses present inside of a closed cryogenic system at millikelvin temperatures.

The ability of superconducting JPAs and TWPAs to generate propagating squeezed states, in perspective, allows one to build local area quantum network [20], generate cluster states [21], and, in general, implement paradigms of continuous-variable quantum information processing [22–24] in the microwave regime.

In order to experimentally investigate a potential of such distributed microwave quantum networks, an accompanying cryogenic infrastructure needs to be created and tested. To this end, in close collaboration with Oxford Instruments, we have designed a cryogenic link, that connects two dilution cryostats spatially separated by 6.5 m. This link contains a 6 m long superconducting microwave cable, which is cooled to the temperatures of less than 100 mK, forming a quantum local area network (QLAN) in the microwave regime. We demonstrate the potential of this QLAN implementation by successfully transferring microwave squeezed states and distributing quantum entanglement across the link.

This thesis is divided into four main chapters, preceded by introduction and concluded by the summary. In Chapter 2, we give an introduction into the fundamental theory of the flux-driven JPAs and TWPAs. To this end, we introduce Gaussian states which provide the basis for the description of quantum states used in our experiments. Afterwards, we present the nonlinear Josephson elements (dc-SQUIDs and SNAILs) used to construct the JPAs and TWPAs. We describe the parametric amplification process and its limitations. We conclude this chapter by theoretically describing the superconducting TWPA. In Chapter 3, we focus on the employed cryogenic and room temperature setups. Here, we present the data acquisition, processing, and calibration procedures. Chapter 4 is dedicated to the experimental measurements and characterization of the JPAs and TWPA. We discuss their properties in the framework of quantum-limited phase-insensitive amplifiers and as generators of squeezed light. We conclude this chapter by introducing different techniques used to calibrate losses and noise in closed cryogenic microwave systems and present the novel two-dimensional Planck spectroscopy. We discuss the experimental results obtained with this method and use them to determine the noise performance of the TWPA. In Chapter 5, we introduce the cryogenic link, discuss its technical details, and present its temperature performance. We conclude this chapter by demonstrating microwave entanglement distribution over the cryogenic link at elevated temperatures (up to 1 K) through the superconducting cable. Chapter 6 concludes the thesis by providing a short summary with a related outlook.

Chapter 2

Propagating quantum microwaves and superconducting circuits

In this chapter, we present the theoretical foundations necessary for this thesis. First, we discuss a theory to describe propagating quantum microwaves. To this end, we present the Wigner function as a quasi-probability distribution. Furthermore, we introduce Gaussian states and provide important examples of such states. Second, we discuss different superconducting elements needed to construct Josephson parametric amplifiers (JPAs) and Josephson traveling wave parametric amplifiers (JTWPAs). These are the coplanar waveguide (CPW), the direct current superconducting quantum interference device (dc-SQUID), and the superconducting nonlinear asymmetric inductive element (SNAIL). We also discuss related amplification mechanisms and how these amplifiers can be used as a source of nonclassical microwave signals.

2.1 Propagating quantum microwaves

Superconducting JPAs and TWPAs are meant to operate with propagating microwave signals in the quantum regime. Here, we provide basic concepts and mathematical tools for describing such quantum microwaves. To this end, we introduce a concept of propagating microwave signals. We employ the Wigner quasi-probability distribution as the main tool for describing Gaussian microwave states and discuss most typical Gaussian states. We conclude the section by introducing a negativity criterion as a measure for quantum entanglement.

2.1.1 Representation of quantum states

Throughout this thesis, we are interested in studying electromagnetic signals with frequencies laying in the range from 3 to 12 GHz propagating along quasi one-dimensional structures, such as coaxial cables or coplanar waveguides. All these frequencies are located well within the microwave regime spanning from 300 MHz to 300 GHz. These propagating waves obey Maxwell's equations, which provide the basis for their classical description. Such signals $A(r,t)$ can be described by introducing their in-phase and out-of-phase quadrature components, $I(t)$ and $Q(t)$, respectivley. We can express an arbitrary propagating single-mode signal at position x as

$$A\left(x,t\right) = I(t)\cos(\omega t - kx) + Q(t)\sin(\omega t - kx) \ , \tag{2.1}$$

where k is the wave vector. We limit the discussion to signals propagating only in one dimension, as we mainly employ signals propagating along quasi one-dimensional structures throughout our experiments. We see, that for a given position, wave vector, and frequency, knowledge over the in- and out-of-phase quadratures gives us access to all relevant information about the signal. However, if one wants to describe quantum-mechanical properties of propagating signals, quantization of the electromagnetic field must be performed. In this context, the amplitude operator for a one-dimensional, quantized, single-mode electrical field is given by [25]

$$\hat{A}(x,t) = C\left[\hat{a}^\dagger e^{i(\omega t - kx)} + \hat{a}e^{-i(\omega t - kx)}\right] = 2C\left[\hat{q}\cos(\omega t - kx) + \hat{p}\sin(\omega t - kx)\right] \ . \tag{2.2}$$

Here, we have introduced the bosonic creation and annihilation operators, $\hat{a}^\dagger$ and $\hat{a}$, respectively. The normalization constant C is chosen in such a way that $\hat{a}^\dagger$ and $\hat{a}$ obey the usual bosonic commutation relation, $\left[\hat{a},\hat{a}^\dagger\right] = 1$. Utilizing these operators, we can define the canonical quadrature operators $\hat{q}$ and $\hat{p}$

$$\hat{q} = \frac{\hat{a}+\hat{a}^\dagger}{2}, \quad \hat{p} = \frac{\hat{a}-\hat{a}^\dagger}{2i}, \quad [\hat{q},\hat{p}] = \frac{i}{2} \ . \tag{2.3}$$

In contrast to the classical quadratures I and Q, we are not able to achieve absolute knowledge of the expectation values of $\hat{q}$ and $\hat{p}$ simultaneously, due to their non-zero commutation relation. The achievable precision is bounded by the Heisenberg-uncertainty relation [26]

$$\Delta q \cdot \Delta p \leq \frac{1}{2}|\langle[\,\hat{q},\hat{p}]\rangle| = \frac{1}{4} \ , \tag{2.4}$$

where the variance ΔO of an observable $\hat{O}$ is defined as

$$(\Delta O)^2 \equiv \langle\hat{O}^2\rangle - \langle\hat{O}\rangle^2 \ . \tag{2.5}$$

Therefore, a complete description of propagating quantum states with only the expectation values of the quadrature components is not possible and an alternative method relying on the full quantum description is needed.

Density matrix

One of the most general ways of describing quantum states utilizes the density matrix formalism, as any quantum-mechanical state is completely described by its density matrix $\hat{\rho}$

$$\hat{\rho} = \sum_{\mathrm{j}=1}^{N} P_{\mathrm{j}} \left|\Psi_{\mathrm{j}}\right\rangle \left\langle\Psi_{\mathrm{j}}\right| \quad , \tag{2.6}$$

where N is the dimension of the Hilbert-space describing the system. With $P_{\mathrm{j}} \leq 1$ and $\sum_{\mathrm{j}}^{N} P_{\mathrm{j}} = 1$, P_{j} represents the classical probability of finding the system in the eigenstate $|\Psi_{\mathrm{j}}\rangle$. The expectation value of an observable $\hat{O}$ can be calculated using the density matrix

$$\langle\hat{O}\rangle = \sum_{\mathrm{j}} P_{\mathrm{j}} \langle\Psi_{\mathrm{j}}|\hat{O}|\Psi_{\mathrm{j}}\rangle = \mathrm{Tr}\left(\hat{O}\hat{\rho}\right) \quad . \tag{2.7}$$

In general, the density matrix approach is very universal and powerful but may lead to significant mathematical complications. Therefore, for a more limited class of quantum states, such as the Gaussian states, one may use certain simplifications. These Gaussian states yield a more practical description of the continuous variable systems we are interested it, as it is possible to express them in terms of phase space quasi-probability distributions such as the Wigner function [27]. This quasi-probability distribution can be seen as an extension of the classical probability distributions, where we have a well-defined probability to find a system in a given state (p, q), to quantum systems, where the Heisenberg uncertainty prohibits precise knowledge of q and p at the same time.

Wigner function

The Wigner function is a quasi-probability distribution function, which gives an equivalent description to the density matrix formalism. In general, the Wigner function of a density matrix $\hat{\rho}$ is defined as [27, 28]

$$W(q,p) = \frac{1}{\pi\hbar} \int_{-\infty}^{\infty} \langle q-y|\, \hat{\rho}\, |q+y\rangle\, e^{2ipy/\hbar} \mathrm{d}y \quad , \tag{2.8}$$

where $\hbar = h/2\pi$ is the reduced Planck constant. Here, as for any probability distribution, the normalization condition $\int_{-\infty}^{\infty}\int_{-\infty}^{\infty} W(p,q)\mathrm{d}p\mathrm{d}q = 1$ must be fulfilled. However, contrary to a classical probability distribution, the Wigner function can take negative values, which makes it a quasi-probability distribution [29].

2.1.2 Gaussian states

Gaussian states are defined as states whose quasi-probability distributions can be fully captured by the Gaussian distribution in the Wigner phase space. Any arbitrary N-mode Gaussian state can be fully described using the statistical moments of its quadratures.

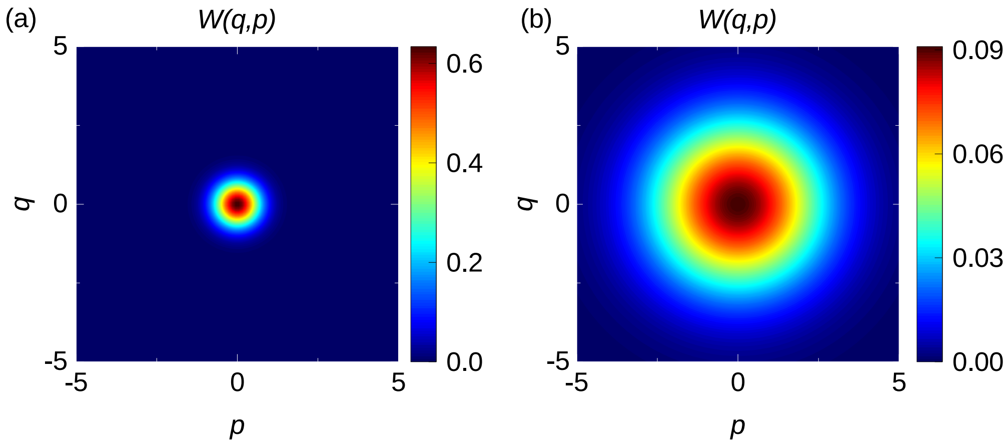

Figure 2.1: (a) Wigner function of a vacuum state with symmetric quadrature variances, $(\Delta p)^2 = (\Delta q)^2 = 1/4$. (b) Wigner function of a thermal state with the photon number $n_{\text{th}} = 4$ corresponding to $(\Delta p)^2 = (\Delta q)^2 = 17/4$. Such a thermal state corresponds to a microwave mode at the frequency of 5 GHz and at the temperature around 1.1 K.

We define the first order statistical moment as the mean, $\bar{\mathbf{x}} = \langle \mathbf{x} \rangle = \mathrm{Tr}\,(\hat{\rho}\hat{\mathbf{x}})$. Here, $\mathbf{x} = (\hat{q}_1, \hat{p}_1, ..., \hat{q}_N, \hat{p}_N)$ is a vector containing the quadrature field operators of each of the N modes. The second order moment is a $2N \times 2N$ real symmetric matrix, also known as the covariance matrix $\mathbf{V}$. Its elements, V_{ij}, are defined as

$$V_{ij} = \langle \hat{x}_i \hat{x}_j + \hat{x}_j \hat{x}_i \rangle / 2 - \langle \hat{x}_i \rangle \langle \hat{x}_j \rangle \ . \tag{2.9}$$

A full quantum description of an arbitrary Gaussian state requires knowledge of only first and second order statistical quadrature moments, $\mathbf{x}$ and $\mathbf{V}$ [30, 31]. The Wigner function of a N-mode Gaussian state can be written as [32]

$$W(\mathbf{x}) = \frac{\exp\left[-\frac{1}{2}(\mathbf{x} - \bar{\mathbf{x}})\,\mathbf{V}^{-1}\,(\mathbf{x} - \bar{\mathbf{x}})^T\right]}{(2\pi)^N \sqrt{\det \mathbf{V}}} \ . \tag{2.10}$$

Equation 2.10 demonstrates, that the Wigner function of a N-mode Gaussian state is always positive. Negative values of the Wigner function correspond to non-Gaussian quantum states.

Vacuum and thermal states

As the first example of Gaussian states, we consider the ground state of the electromagnetic field, also known as the vacuum state, $|0\rangle$. The vacuum state corresponds to the zero equilibrium temperature, $T = 0$. Although the mean expectation values of quadratures are zero in the vacuum state, their variances remain profoundly non-zero, giving rise to vacuum field fluctuations. These fluctuations are a direct consequence of the bosonic commutation relation. The statistical moments of the vacuum state are [33]

$$\bar{\mathbf{x}}_{\mathrm{vac}} = 0 \quad \text{and} \quad \mathbf{V}_{\mathrm{vac}} = \mathbb{1}_2 \ , \tag{2.11}$$

where $\mathbb{1}_2$ is the 2×2 identity matrix. This state has minimum uncertainty with equal variances for both quadratures $(\Delta p)^2 = (\Delta q)^2 = 1/4$. Figure 2.1(a) shows the Wigner function of the vacuum state.

In the finite temperature regime, $T > 0$, the ideal vacuum state is transformed into the thermal state. The thermal states are characterized by their mean number of photons, n_{th}, in the bosonic mode, which follows the Bose-Einstein statistics [34]

$$n_{\mathrm{th}} = \frac{1}{\exp\left(\frac{hf}{k_{\mathrm{B}}T}\right) - 1} \ . \tag{2.12}$$

Here, k_{B} is the Boltzmann constant. The density matrix of the thermal state is given by [35]

$$\hat{\rho}_{\mathrm{th}} = \sum_n \frac{n_{\mathrm{th}}^n}{(1 + n_{\mathrm{th}})^{(n+1)}} \left|n\right\rangle \left\langle n\right| \ , \tag{2.13}$$

which only depends on the mean photon number n_{th}. The mean and covariance matrix of the thermal state are given by

$$\bar{\mathbf{x}}_{\mathrm{th}} = 0 \quad \text{and} \quad \mathbf{V}_{\mathrm{th}} = (2n_{\mathrm{th}} + 1)\frac{\mathbb{1}_2}{4} \ . \tag{2.14}$$

The Wigner function of a thermal state with $n_{\mathrm{th}} = 4$ is plotted in Fig. 2.1(b). Even though it is impossible to reach $T = 0$, often, microwave thermal states in our experiments can approximated as vacuum states if the condition $k_{\mathrm{B}}T \ll hf$ is fulfilled.

Coherent states

The third class of Gaussian states is represented by coherent states, $\left|\alpha\right\rangle$, which are also minimum uncertainty states just like the vacuum states. Mathematically, a coherent state is defined as the eigenstate of the annihilation operator $\hat{a}$, with a corresponding eigenvalue α

$$\hat{a}\left|\alpha\right\rangle = \alpha\left|\alpha\right\rangle \ . \tag{2.15}$$

Since the annihilation operator $\hat{a}$ is not a Hermitian operator, the displacement amplitude, $\alpha = Q + iP$, can be complex. Creating a coherent state is realized by applying the displacement operator

$$\hat{D}(\alpha) = \exp(\alpha\hat{a}^\dagger - \alpha^*\hat{a}) \tag{2.16}$$

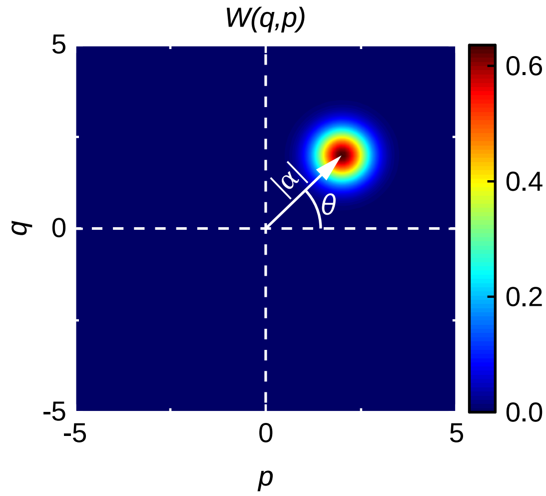

Figure 2.2: Wigner function of the ideal coherent state with $|\alpha| = 4$ and $\theta = \pi/4$.

to the vacuum state $|0\rangle$. If we consider the phase space representation, the covariance matrix of the coherent state is that of the vacuum state, but its mean is displaced to the phase space coordinates (Q, P), as can be seen in Fig. 2.2. The coherent states are described by

$$\bar{\mathbf{x}}_{\rm coh} = (Q, P) \quad \text{and} \quad \mathbf{V}_{\rm coh} = \mathbb{1}_2 \ . \tag{2.17}$$

Single- and two-mode squeezed states

The last class of Gaussian states are squeezed states. Here, we can differentiate between single-mode squeezed (SMS) and two-mode squeezed (TMS) states. SMS states have different variances along different quadratures, as shown in Fig. 2.3, giving them a distinct ellipsoidal shape which is "squeezed" along a certain direction, as compared to that of coherent, vacuum, or thermal states. Mathematically, they can be described by applying a single-mode squeezing operator [36]

$$\hat{S}(\xi) = \exp\left(\frac{1}{2}\xi^*\hat{a}^2 - \xi(\hat{a}^\dagger)^2\right) \tag{2.18}$$

to the vacuum state $|0\rangle$, where $\xi = re^{i\varphi}$ is the complex squeezing amplitude, with r being the squeezing factor and φ the squeezing phase. The latter describes a squeezing orientation in the phase space. Here, it is more common to give a squeezing angle, $\gamma = -\varphi/2$, which represents the angle between the anti-squeezed quadrature direction and the p-axis, as depicted in Fig. 2.3. The variances along the squeezed and anti-squeezed quadratures are given by $\sigma_{\rm s}^2 = {\rm e}^{-2r}/4$ and $\sigma_{\rm as}^2 = {\rm e}^{2r}/4$, respectively. Here, it can be seen, that the variance of the squeezed quadrature can drop below $1/4$, which is that of the vacuum state. As the Heisenberg uncertainty relation has to be fulfilled, the variance of

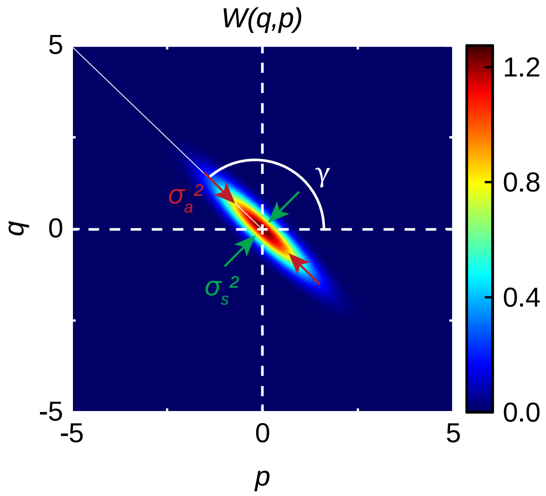

Figure 2.3: Wigner function of a single-mode squeezed state with $r = 0.8$ and $\theta = 3\pi/4$. This corresponds to the squeezed variance of $\sigma_s^2 = 0.05$ and the squeezing level of $S = 6.9\,\mathrm{dB}$ below the vacuum level.

the orthogonal quadrature must be increased accordingly.

In our experiments, SMS states can be created by using JPAs or TWPAs in the degenerate regime, acting as phase-sensitive amplifiers with the vacuum state as their input. To quantify the amount of squeezing and anti-squeezing generated by these devices, we introduce the squeezing and anti-squeezing levels, S and A, respectively

$$S = -10\log_{10}\left(\frac{\sigma_\mathrm{s}^2}{0.25}\right) \quad \text{and} \quad A = 10\log_{10}\left(\frac{\sigma_\mathrm{a}^2}{0.25}\right) \ , \tag{2.19}$$

where the factor 0.25 stems from the quadrature variance of the vacuum, originating from our definition of quadrature operators. Therefore, positive levels of S indicate squeezing below the vacuum limit. The quadrature mean and covariance matrix of a single-mode squeezed state are [33]

$$\bar{\mathbf{x}}_\mathrm{sms} = 0 \text{ and } \mathbf{V}_\mathrm{sms} = \begin{pmatrix} \cosh(2r) + \cos(\varphi)\sinh(2r) & \sin(\varphi)\sinh(2r) \\ \sin(\varphi)\sinh(2r) & \cosh(r) - \cos(\varphi)\sinh(2r) \end{pmatrix} \ . \tag{2.20}$$

A particularly important extension of the squeezed states are two-mode squeezed (TMS) states. These states represent a particular realization of quantum entangled states and can be readily generated in many experiments with superconducting quantum circuits. In our experiments, the TMS state are created by sending squeezed states at the same frequency to a symmetric beam splitter, which leads to the creation of an entangled, frequency-degenerate, state at its outputs [32, 37]. Another way of creating the TMS states involves using broadband parametric amplifiers, such as the TWPA. In doing so, we generate pairs of entangled, frequency-nondegerate, photons in the output modes, where the correlations between these modes establish the two-mode squeezing [35]. An arbitrary TMS state can be described by the two-mode squeezing operator [35]

$$\hat{S}_2(\xi) = \exp\left[\xi^*\left(\hat{a}\hat{b} - \hat{a}^\dagger\hat{b}^\dagger\right)\right] \quad , \tag{2.21}$$

where $\hat{a}$ and $\hat{b}$ are the annihilation operators of the different modes and $\xi = re^{i\varphi}$ is the complex two-mode squeezing amplitude, identical to the SMS operator definition. For $\varphi = 0$, the quadrature mean and covariance matrix of an ideal TMS state are given by [35]

$$\mathbf{x}_{\text{tms}} = 0 \quad \text{and} \quad \mathbf{V}_{\text{tms}} = \frac{1}{4}\begin{pmatrix} \cosh(2r) & 0 & \sinh(2r) & 0 \\ 0 & \cosh(2r) & 0 & -\sinh(2r) \\ \sinh(2r) & 0 & \cosh(2r) & 0 \\ 0 & -\sinh(2r) & 0 & \cosh(2r) \end{pmatrix} \quad . \tag{2.22}$$

The two-mode squeezed vacuum state does not imply any local squeezing in individual modes and the two-mode squeezing is present between the different modes. Locally, these modes look like thermal states. The Wigner function of this TMS state can be written as [38]

$$W(q_1, q_2.p_1, p_2) = \frac{4}{\pi^2}\exp\left(-\frac{(q_1+q_2)^2+(p_1-p_2)^2}{\mathrm{e}^{2r}} - \frac{(q_1-q_2)^2+(p_1+p_2)^2}{\mathrm{e}^{-2r}}\right) \quad . \tag{2.23}$$

For $r \to \infty$, this Wigner function takes the form $W(q_1, q_2, p_1, p_2) \propto \delta(q_1 - q_2)\delta(p_1 + p_2)$, where δ denotes the Dirac delta-function. This state is the basis of the quantum nonlocality paradox, which has been proposed by Einstein, Podolsky, and Rosen [39].

Two-mode squeezing is tightly related to the concept of quantum entanglement. In general, a state shared by two parties A and B can be described by a joint density matrix $\hat{\rho}_{\text{AB}}$. This state is separable, if $\hat{\rho}_{\text{AB}}$ can be decomposed into a convex sum of product states. Each of these product states fully describes the respective local subsystems. A bipartite quantum state is defined to be quantum-entangled if its density matrix is not separable. This bipartite quantum entanglement can be quantified by the so-called negativity measure, N. It is an entanglement monotone based on the Peres-Horodecki positive partial transpose (PPT) criterion [40], making it rather easy to calculate from the covariance matrix. For bipartite Gaussian states, the negativity can be expressed as [41]

$$N = \max\left(0, \frac{1}{8\tilde{\nu}_-} - \frac{1}{2}\right), \tag{2.24}$$

where $\tilde{\nu}_-$ is the smallest symplectic eigenvalue of the partially transposed density matrix. A positive negativity, $N > 0$, indicates the presence of quantum-entanglement. In order to calculate the symplectic eigenvalues from the covariance matrix, we first introduce the covariance matrix of a two-mode Gaussian state. It can be expressed in the form

$$\mathbf{V} = \begin{pmatrix} \mathbf{A} & \mathbf{C} \\ \mathbf{C}^{\mathrm{T}} & \mathbf{B} \end{pmatrix} \ , \tag{2.25}$$

where $\mathbf{A}$, $\mathbf{B}$, and $\mathbf{C}$ are 2×2 matrices. Here, $\mathbf{A}$ and $\mathbf{B}$ describe the local states A in the first mode and B in the second mode, respectively. The matrix $\mathbf{C}$ contains the information about cross-correlations between both parties. In order to calculate the symplectic eigenvalues, it is useful to first define the local symplectic invariants of the covariance matrix [42]

$$I_1 = \det(\mathbf{A}), \ \ I_2 = \det(\mathbf{B}), \ \ I_3 = \det(\mathbf{C}), \ \ I_4 = \det(\mathbf{D}) \ . \tag{2.26}$$

With access to the symplectic invariants, we can define the two symplectic eigenvalues of the two-mode Gaussian state

$$\tilde{\nu}_{\pm} = \sqrt{\frac{\Delta \pm \sqrt{\Delta^2 - 4I_4}}{2}} \ , \tag{2.27}$$

where $\Delta = I_1 + I_2 + 2I_3$.

2.2 Superconducting parametric amplifiers

In this section, we theoretically describe parametric amplification in the microwave regime with a flux-driven JPA, as well as with a JTWPA. These devices rely on the interaction between a signal and nonlinear medium. For the JPA, this interaction is achieved by placing the dc-SQUID inside a cavity, which enhances the interaction time. For the JTWPA, the long interaction times are achieved by long chains of nonlinear elements embedded in the center conductor of a transmission line. Both devices allow for parametric amplification of microwave signals with a noise performance close to the standard quantum limit. They can also serve for the generation of quantum microwave signals.

2.2.1 Superconductivity and Josephson junctions

In order to preserve quantum states, low losses are of utmost importance. To this end, we utilize superconducting materials throughout our experimental setups which minimize dissipation, and thus, coupling to a noisy environment. The superconductivity itself is a consequence of perfect diamagnetism below a certain transition temperature, known as the Meißner-Ochsenfeld effect [43]. Another fundamental phenomenon in superconductors which is central to our work is the Josephson effect [44]. The latter occurs when two bulk superconductors are weakly coupled to each other. To explain this effect, we need to consider superconductivity as a quantum phenomenon. This allows

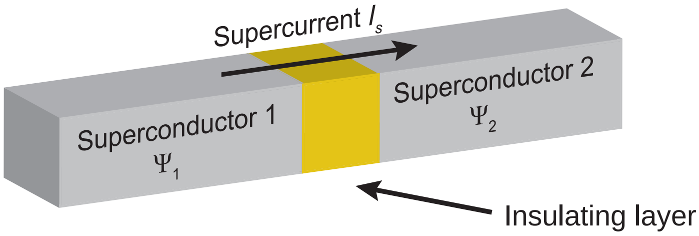

Figure 2.4: Schematic of a Josephson junction consisting of two bulk superconductors (grey) coupled via an insulating layer (yellow). The symbol $\Psi_{1,2}$ denotes the macroscopic wave function of the respective bulk superconductor.

us to assign a macroscopic wave function $\Psi_i(\mathbf{r},t) = \sqrt{n_{\mathrm{s},i}}e^{i\theta_i(\mathbf{r},t)}$, where $i = 1,2$ denotes superconductor 1 or 2 , to each of the bulk superconductors [45, 46]. Here, $\sqrt{n_{\mathrm{s},i}}$ refers to the density of Cooper pairs and $\theta_i(\mathbf{r},t)$ is the global phase of the wave function in each superconductor. By placing a thin layer of non-superconducting material, such as an insulator, between the two superconductors, an overlap of the two wavefunctions can be established and a Josephson junction (JJ) is formed. Such a structure is illustrated in Fig. 2.4. Considering that both wavefunctions posses different global phases, one can define a gauge invariant phase difference across the Josephson junction given by [47]

$$\varphi(\mathbf{r},t) = \theta_2(\mathbf{r},t) - \theta_1(\mathbf{r},t) - \frac{2\pi}{\Phi_0}\int_1^2 \mathbf{A}(\mathbf{r},t)d\mathbf{l} \ , \tag{2.28}$$

where $\Phi_0 = \frac{h}{2e}$ is the magnetic flux quantum and $\mathbf{A}(\mathbf{r},t)$ is a magnetic vector potential. The Josephson effect can be described using two equations, the first and the second Josephson equations. The first Josephson equation is also known as the current-phase relation and connects the Josephson phase difference φ with the supercurrent I_s across the Josephson junction [48]

$$I_\mathrm{s} = I_\mathrm{c}\sin(\varphi) \ , \tag{2.29}$$

where I_c is the critical current which determines the maximum amplitude of the supercurrent. The second Josephson equation, also known as the voltage-phase relation, can be derived from the gauge invariant phase difference and gives a link between the voltage V across the Josephson junction and the time-derivative of the Josephson phase [48]

$$\frac{\partial\varphi}{\partial t} = \frac{2\pi}{\Phi_0}V(t) \ . \tag{2.30}$$

By using $V = L\frac{\mathrm{d}I_\mathrm{s}}{\mathrm{d}t}$ and the Josephson equations one can derive the inductance of the Josephson junction [48]

$$L_\mathrm{s}(\varphi) = \frac{\Phi_0}{2\pi I_\mathrm{c}\cos\varphi} = \frac{L_\mathrm{J}}{\cos\varphi} \ , \tag{2.31}$$

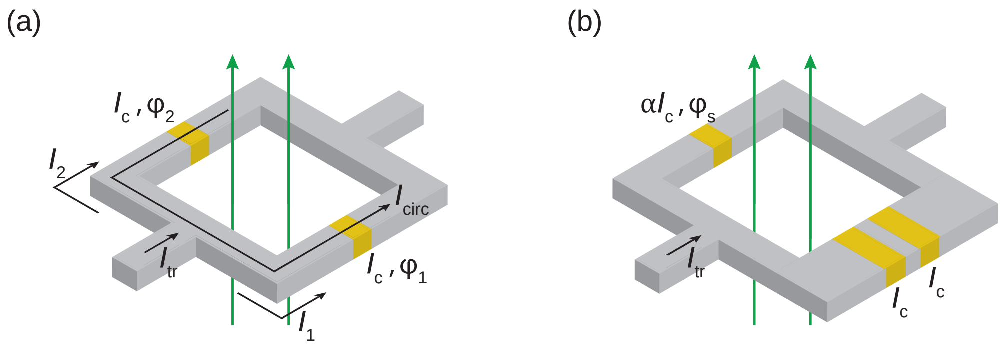

Figure 2.5: (a) Schematic drawing of a dc-SQUID consisting of a superconducting loop interrupted by two Josephson junctions with equal critical currents I_c and related phase difference $\varphi_{1,2}$. (b) Schematic drawing of a SNAIL consisting of two large Josephson junctions and one that has a critical current that is smaller by a factor $\alpha < 1$. For both panels (a) and (b), the green arrows indicate the external magnetic flux density through the superconducting loop.

where we have introduced the Josephson inductance $L_J = L_s(\varphi = 0) = \frac{\Phi_0}{2\pi I_c}$ as a characteristic parameter of the Josephson junction. Consequently, the junction behaves as a nonlinear inductor, which is particularly useful in many applications of superconducting circuits.

2.2.2 dc-SQUID and SNAIL

In the following section we will introduce two Josephson junction-based devices: a dc-SQUID and a SNAIL. These superconducting devices are central parts of JPAs and TWPAs.

dc-SQUID

One of the main building blocks of a JPA is the dc-SQUID. Its basic structure is shown in Fig. 2.5(a). Here, two Josephson junctions are connected in parallel and linked via a superconducting loop. We assume that both junctions are identical with the same critical current $I_{c,1} = I_{c,2} = I_c$. Due to boundary conditions, the gauge invariant phase differences φ_1 and φ_2 of each Josephson junction are not independent of each other and the total phase change along the closed dc-SQUID loop has to be $\oint_C \nabla\theta \cdot \mathrm{d}r = 2\pi n, n \in \mathbb{Z}$. By utilizing the gauge invariant phase difference introduced in Eq. 2.28, the phase gradient across the superconductor can be written as [48]

$$\nabla\theta = \frac{2\pi}{\Phi_0}(\Lambda \mathbf{J}_s + \mathbf{A}) \ , \tag{2.32}$$

where $\mathbf{J}_\mathrm{s}$ is the supercurrent density, $\mathbf{A}$ is the vector potential, and Λ is the London parameter. Assuming that the superconducting loop is much thicker than the London penetration depth, one can always find an integration path deep inside the superconductor, where the supercurrent density $\mathbf{J}_\mathrm{s} = 0$, such that we can neglect the integral part over $\mathbf{J}_\mathrm{s}$. In this case, the only contribution comes from the integral over $\mathbf{A}$, which yields the magnetic flux Φ enclosed in the loop. Using this we obtain

$$\varphi_2 - \varphi_1 = \frac{2\pi\Phi_\mathrm{total}}{\Phi_0} + 2\pi n \ , \tag{2.33}$$

where Φ_total is the total magnetic flux threading the dc-SQUID loop. This total flux consists of the externally applied flux Φ_ext and the self-induced flux $L_\mathrm{loop}I_\mathrm{circ}$,

$$\Phi_\mathrm{total} = \Phi_\mathrm{ext} + L_\mathrm{loop}I_\mathrm{circ} \ . \tag{2.34}$$

Here, L_loop is the geometric inductance of the superconducting loop and I_circ is the screening current circulating in the loop defined as

$$I_\mathrm{circ} = \frac{I_1 - I_2}{2} = I_\mathrm{c} \cos\left(\frac{\varphi_1 + \varphi_2}{2}\right) \sin\left(\frac{\varphi_1 - \varphi_2}{2}\right) \ , \tag{2.35}$$

where I_1 and I_2 are the supercurrents flowing through the respective junction. Furthermore, we can calculate the total transport current I_tr through the dc-SQUID by adding the currents through each of the Josephson junctions

$$I_\mathrm{tr} = I_1 + I_2 = 2I_\mathrm{c} \sin\left(\frac{\varphi_1 + \varphi_2}{2}\right) \cos\left(\frac{\varphi_1 - \varphi_2}{2}\right) \ . \tag{2.36}$$

Using these results, we can rewrite the total magnetic flux through the loop as

$$\frac{\Phi_\mathrm{total}}{\Phi_0} = \frac{\Phi_\mathrm{ext}}{\Phi_0} - \frac{\beta_L}{2} \cos\left(\frac{\varphi_1 + \varphi_2}{2}\right) \sin\left(\frac{\varphi_1 - \varphi_2}{2}\right) \ , \tag{2.37}$$

where we introduce the screening parameter $\beta_L = 2L_\mathrm{loop}I_c/\Phi_0$ [49] which describes the screening properties of the dc-SQUID. Here, two distinct regimes can be found. First, for $\beta_L \approx 0$, the self-induced flux by the dc-SQUID can be neglected and, thus, the total flux can be approximated with the externally applied flux $\Phi_\mathrm{total} \approx \Phi_\mathrm{ext}$. In this case, we can define a nonlinear flux-dependent inductance of the dc-SQUID [50]

$$L_\mathrm{S}(\Phi_\mathrm{ext}) = \frac{\Phi_0}{4\pi I_\mathrm{c}} \left|\cos\left(\pi \frac{\Phi_\mathrm{ext}}{\Phi_0}\right)\right| \ . \tag{2.38}$$

From this we can see, that a dc-SQUID with $\beta_L \approx 0$ behaves like a a single Josephson junction with a flux-dependent maximum supercurrent. For $\beta_L > 0$, the self inductance of the loop is not negligible anymore, thus requiring a self-consistent solution of Eq. 2.36 and

Eq. 2.37, while fulfilling the fluxiod quantization introduced in Eq. 2.33. In most cases of finite screening, analytical expressions cannot be derived and one needs to perform numerical simulations of the system.

SNAIL

In general, it is instructive to study a potential energy $U(\varphi)$ of an arbitrary Josephson circuit expanded in the Taylor series

$$U(\varphi) = E_J \left[c_2(\Phi_{\text{ext}})\,\varphi^2 + c_3(\Phi_{\text{ext}})\,\varphi^3 + c_4(\Phi_{\text{ext}})\,\varphi^4 + ... \right] \quad , \tag{2.39}$$

where $E_J = \frac{\Phi_0 I_c}{2\pi}$ is the Josephson energy of the single Josephson junction. Here, the expansion coefficient c_2 relates to the linear part of the Josephson inductance, the c_3 term relates to three-wave mixing (3WM), and the c_4 term relates to four-wave mixing (4WM) [51, 52]. The latter two terms are fundamental for the performance of any parametric amplifier, as they determine the mixing process present. The four-wave mixing process is promoted by the third order nonlinearity in the Josephson inductance, which corresponds to the fourth order in the potential energy. As this is equivalent to the Kerr-nonlinearity in optical fibers, it is often referred to as Kerr-like nonlinearity. During the four-wave mixing process, a total of four photons interact: two pump photons (with frequency ω_p and wave vector k_p) are converted into one signal $(\omega_\text{s}, k_\text{s})$ and one idler photon $(\omega_\text{i}, k_\text{i})$ under both energy $(2\omega_\text{p} = \omega_\text{s} + \omega_\text{i})$ and momentum $(2k_\text{p} = k_\text{s} + k_\text{i})$ conservation. Three-wave mixing, on the other hand, is promoted by the third order nonlinearity in the potential energy. Here, only one pump photon interacts with a signal and an idler photon, leading to the according relations $\omega_\text{p} = \omega_\text{s} + \omega_\text{i}$ and $k_\text{p} = k_\text{s} + k_\text{i}$. Different Josephson circuits will result in different expansion coefficients, for example $c_2 = 1$, $c_3 = 0$ and $c_4 = -\frac{1}{12}$ for the single Josephson junction. Another Josephson circuit we want to consider is the SNAIL. In general, it consists of a superconducting loop interrupted by n large Josephson junctions and a single smaller junction with the Josephson energies E_J and αE_J, $\alpha < 1$, respectively. As for the dc-SQUID, we can bias the SNAIL with an external magnetic flux Φ_ext. For $\alpha \approx 0.8$ and $\Phi_\text{ext} \approx 0.5\,\Phi_0$, this circuit can be used as the flux qubit [53, 54] with a double-well potential. Additionally, in the limit of $n \gg 1$ the potential approaches the fluxonium qubit regime [55]. The SNAILs used for the TWPA in this work contain two large, $n = 2$, and one small junction, $\alpha < 1$. Therefore, we will limit our discussion to this case. A scheme of the SNAIL is illustrated in Fig. 2.5(b). In contrary to the flux qubit, we aim for a set of parameters which creates a potential with a single minimum, limiting the SNAIL asymmetry α to in the range of $0 < \alpha < 0.5$. In order to derive the potential energy of the SNAIL, we denote the phase across the small Josephson junction as φ_s, and the total phase traversing the SNAIL loop as $\varphi_\text{ext} = 2\pi\Phi_\text{ext}/\Phi_0$. Using Kirchhoff's law,

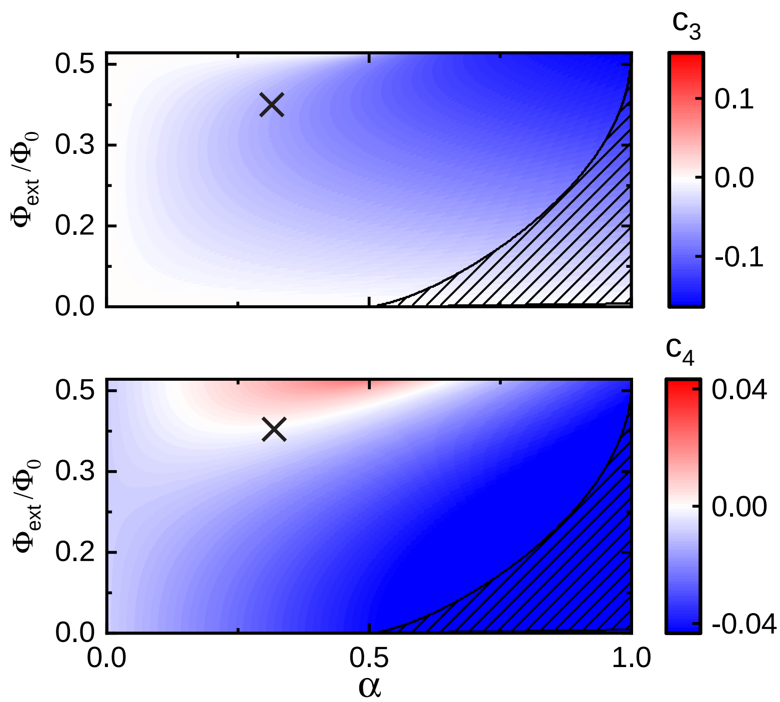

Figure 2.6: Dependence of the coefficients c_3 and c_4 on the external magnetic flux and the SNAIL asymmetry α. We can see, that it is possible to have finite 3WM (i.e. $c_3 \neq 0$) and simultaneously vanishing 4WM (i.e. $c_4 \to 0$) for $\alpha \approx 0.3$ and an external flux of roughly $0.4\,\Phi_{\mathrm{ext}}/\Phi_0$. This optimal regime is marked by the black crosses. The black-hatched regions correspond to unwanted double well behavior.

the transport current I_{tr} across the SNAIL is given by [56]

$$I_{\mathrm{tr}} = \alpha I_c \sin(\varphi_s) - I_c \sin\left(\frac{\varphi_{\mathrm{ext}} - \varphi_s}{2}\right), \tag{2.40}$$

where we assume a uniform phase drop across the two large junctions. This assumption is based on the fact that internal capacitances of the junctions are small and the self-resonance frequencies of the element are expected to be above 30 GHz. Therefore, it behaves as a nonlinear inductor at typical frequencies of circuit QED experiments of around 5 GHz [57]. Utilizing Eq. 2.30, the voltage-phase relation, we obtain the potential energy $U_S(\varphi_s)$ of the SNAIL

$$\begin{aligned} U_S(\varphi_s) = E_J \int \left(\alpha I_c \sin(\varphi_s) - I_c \sin\left(\frac{\varphi_{\mathrm{ext}} - \varphi_s}{2}\right)\right) \mathrm{d}\varphi_s = \\ -\alpha E_J \cos(\varphi_s) - 2E_J \cos\left(\frac{\varphi_{\mathrm{ext}} - \varphi_s}{2}\right) \quad . \end{aligned} \tag{2.41}$$

Next, we expand the potential energy into the Taylor series around its minimum located at $\varphi_{\min}$. Introducing $\tilde{\varphi} = \varphi_s - \varphi_{\min}$, we obtain

$$U_S(\tilde{\varphi})/E_J = c_1\tilde{\varphi} + c_2\tilde{\varphi}^2 + c_3\tilde{\varphi}^3 + c_4\tilde{\varphi}^4 + \ldots \ . \tag{2.42}$$

The individual flux-dependent coefficients are given by

$$c_n = \frac{E_J}{n!}\frac{\partial^n U_S(\varphi_s)}{\partial \varphi_s^n}\bigg|_{\varphi_{\min}} \ . \tag{2.43}$$

The linear inductance of the SNAIL is given as $L_{\mathrm{SNAIL}}(\varphi_{\mathrm{ext}}) = L_{\mathrm{J}}/c_2(\varphi_{\mathrm{ext}})$. Furthermore, expanding U_S around its minimum leads to a vanishing transport current through the SNAIL, since $c_1 = 0$ at $\varphi_s = \varphi_{\min}$. The coefficients c_3 and c_4 are shown in Fig. 2.6 for various flux and SNAIL asymmetry values. For $\alpha > 0.5$, a double well behavior of the potential energy emerges. The potential energy as a function of φ_s for the Kerr-free situation, as well as for parameters leading to a double well potential can be seen in Fig. 2.7.

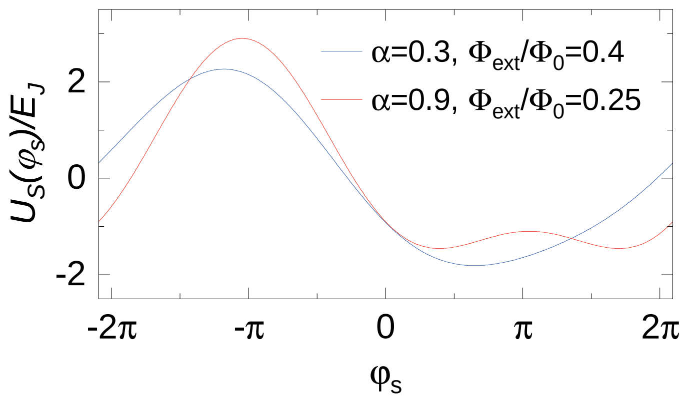

Figure 2.7: Potential energy of a single SNAIL for $\alpha = 0.3$, $\Phi_{\mathrm{ext}} = 0.4\,\Phi$ (blue) and $\alpha = 0.9$, $\Phi_{\mathrm{ext}} = 0.25\,\Phi$ (red). The blue line corresponds to the optimal regime marked by the crosses in Fig. 2.6. Here, $\varphi_{\min} \approx 0.6\pi$. The red line corresponds to a point inside the hatched region of Fig. 2.6, where a double-well potential emerges.

2.2.3 Narrow-band amplification with Josephson parametric amplifiers

Josephson parametric amplifiers are important building blocks for many experiments with quantum microwaves, as they can be used for low noise amplification of signals, as well as for generation of squeezed states of light [6, 58, 59]. In order to understand the JPA amplification mechanism, we first introduce a CPW resonator and briefly describe its characteristics using a distributed element approach. We continue with the description of

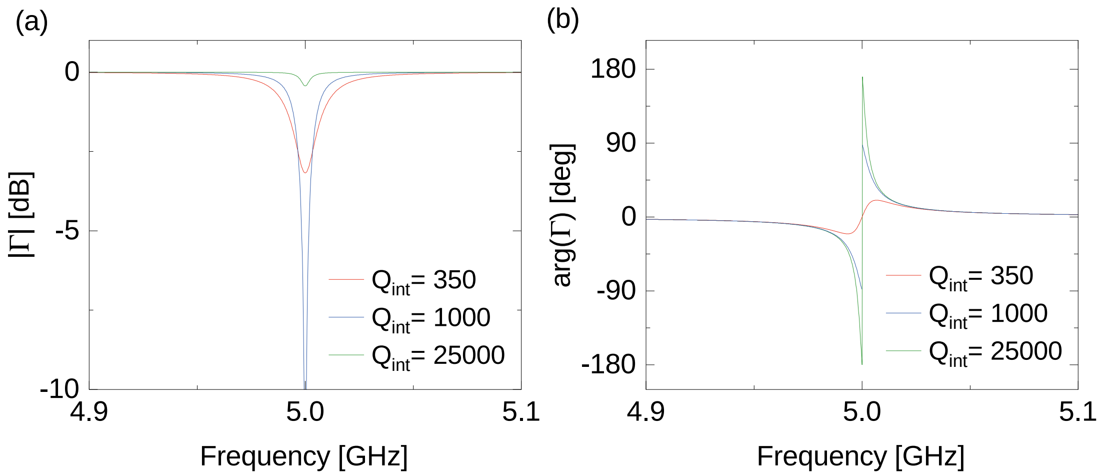

Figure 2.8: Magnitude (a) and phase (b) of the reflection coefficient Γ as a function of frequency for a CPW with the external quality factor $Q_{\mathrm{ext}} = 1000$ and resonance frequency $f_r = 5.0$ GHz. Red lines correspond to an undercoupled resonator and the green lines describe the case of an overcoupled resonator. Blue lines indicate the case when the internal and external quality factors are equal, corresponding to a critically coupled resonator.

parametric amplification process and conclude this subsection by discussing generation of squeezed states using JPAs.

CPW resonator

Besides the dc-SQUID, a coplanar waveguide resonator is the second important part of a typical JPA. To describe the behaviour of the CPW resonator, we start by introducing the CPW itself, which acts as a quasi one-dimensional transmission line. Its fundamental structure is similar to a coaxial cable, as it consist of a groundplane and a center conductor separated by an insulating gap. To create a resonator from this transmission line, one needs to impose length restrictions with corresponding boundary conditions. Typically, these boundary conditions are either zero voltage, or zero current at the ends of the transmission line. The zero current condition can be realized by introducing a gap in the center conductor with a corresponding coupling capacitance C_{c}. This gap also serves as a coupling port and can be used to couple an external signal field to the resonator. The zero voltage condition can be achieved by connecting the CPW to ground. To create a reflection type $\lambda/4$ resonator, we employ both of these boundary conditions. The fundamental resonance frequency of the corresponding quarter-wavelength resonator with the length l is given by [60]

$$f_r = \frac{1}{4l\sqrt{L_0 C_0}} \;, \tag{2.44}$$

where L_0 and C_0 are the inductance and capacitance per unit length of the transmission line. An important parameter characterizing a resonator is its quality factor Q which describes its loss rate. Generally, it is defined as [61]

$$Q = 2\pi \frac{\text{average energy stored}}{\text{energy loss/cycle}} = \frac{f_r}{\text{FWHM}} \ , \tag{2.45}$$

where the full width at half maximum (FWHM) describes the linewidth of the resonant mode. If we consider the different loss channels of a resonator, we can distinguish between internal and external losses. The internal losses can be described by considering a resonator, that is not coupled to any other parts of the circuit. Therefore, losses are determined solely by imperfections (parasitic coupling to various environmental modes) of the resonator itself. These can be related to a finite surface resistance [62], two-level fluctuators [63], or radiative losses. All these loss mechanisms are taken into account by the internal quality factor Q_{int}. If we now consider a perfect cavity, which is coupled to the other parts of the circuit via a coupling capacitance C_{c}, the loss rate is described by the external quality factor Q_{ext}. The internal and external quality factors can be combined into the loaded quality factor Q_{l}

$$\frac{1}{Q_{\text{l}}} = \frac{1}{Q_{\text{ext}}} + \frac{1}{Q_{\text{int}}} = \frac{\kappa_{\text{int}} + \kappa_{\text{ext}}}{2\pi f_r} = \frac{\kappa_{\text{total}}}{2\pi f_r} \ . \tag{2.46}$$

Here, we can differentiate between two cases: the overcoupled regime, $Q_{\text{ext}} \ll Q_{\text{int}}$, and the undercoupled regime, $Q_{\text{ext}} \gg Q_{\text{int}}$. In order to experimentally probe the quarter-wavelength resonator, one needs to measure its reflection coefficient Γ. As the reflected output signal can vary in amplitude and phase, Γ is a complex function [64]

$$\Gamma = \frac{4\pi^2(f - f_r)^2 + i\kappa_{\text{int}} 2\pi(f - f_r) + (\kappa_{\text{ext}}^2 - \kappa_{\text{int}}^2)/4}{[2\pi(f - f_r) + i(\kappa_{\text{ext}} + \kappa_{\text{int}})/2]^2} \ , \tag{2.47}$$

where κ_{int} and κ_{ext} are the internal and external loss rates, respectively. These loss rates can be converted to quality factors via $Q_{\text{int}} = 2\pi f_r/\kappa_{\text{int}}$ and $Q_{\text{ext}} = 2\pi f_r/\kappa_{\text{ext}}$. Figure 2.8 shows the magnitude as well as the phase of the reflection coefficient Γ for different internal quality factors as a function of frequency. In our experiments, we determine the resonance frequency via the detection of the 360° phase shift in case of an overcoupled resonator, or by the detection of the Lorentzian dip in the transmission magnitude in case of an undercoupled resonator.

Resonance frequency of the JPA

From Eq. 2.44 we see that changing the inductance of the resonator leads to a change of its fundamental resonance frequency. For the JPA, we implement an in-situ flux-tunablity of the resonance frequency by short-circuiting a quarter-wavelength CPW to ground via a dc-SQUID, as shown in Fig. 2.9. Here, the dc-SQUID acts as a flux-tunable inductor

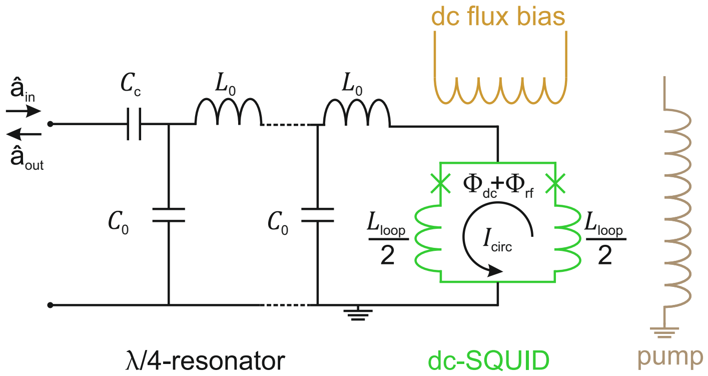

Figure 2.9: Distributed element diagram of a JPA consisting of a CPW resonator short-circuited to ground via a dc-SQUID. The crosses indicate the Josephson junctions. An external coil can be used to create a constant dc-flux bias, Φ_{dc}, while a microwave contribution Φ_{rf}, can be generated by the pump line which is inductively coupled to the dc-SQUID loop.

and we can use the external magnetic flux, $\Phi_{\mathrm{ext}} = \Phi_{\mathrm{dc}}$ threading the SQUID loop to tune the resonance frequency f_0 of the whole JPA circuit. Taking into account the distributed nature of the quarter-wavelength resonator and the lumped element nature of the dc-SQUID, one can derive a transcendental equation for the resonance frequency of the JPA [65–67]

$$\left(\frac{\pi f_0}{2 f_{\mathrm{r}}}\right) \tan\left(\frac{\pi f_0}{2 f_{\mathrm{r}}}\right) = 2\frac{4\pi^2}{\Phi_0^2} L_{\mathrm{res}} E_S\left(\Phi_{\mathrm{ext}}\right) - \frac{2C_{\mathrm{s}}}{C_{\mathrm{res}}}\left(\frac{\pi f_0}{2 f_{\mathrm{r}}}\right)^2 , \tag{2.48}$$

where L_{res} and C_{res} are the total inductance and capacitance of the bare resonator, respectively, $E_S\left(\Phi_{\mathrm{ext}}\right)$ is the flux-dependent energy of the dc-SQUID [68] and C_s is the capacitance of the single Josephson junction. As the capacitance of the Josephson junctions is typically much smaller than the one of the resonator, $C_{\mathrm{s}} \ll C_{\mathrm{res}}$, the last term of Eq. 2.48 can usually be neglected in order to simplify the equation.

Parametric amplification with a flux driven JPA

In order to achieve parametric amplification with the JPA, we need to apply a strong external pump tone. Depending on the choice of the pump frequency, different types of wave mixing processes can be enabled. In our case, we apply a microwave signal at the frequency $\omega_{\mathrm{p}} = 2\omega_0 = 4\pi f_0$, close to twice the frequency of the input signal $\omega_{\mathrm{s}} = \omega_0 - \delta\omega$. This choice of frequencies results in the 3WM process. The pump tone is inductively coupled to the dc-SQUID via a nearby pump line. By applying this pump tone, the magnetic flux through the dc-SQUID is varied periodically with the amplitude Φ_{rf}. This flux contribution adds to the constant magnetic flux Φ_{dc} created by a coil located in the vicinity of the JPA. The periodic modulation of the flux leads to a periodic modulation of the inductance of the dc-SQUID, which in turn, results in a modulation of the resonance frequency of the whole circuit. From a theoretical point of view, this situation can be modelled as a parametric oscillator. In the case of the flux-driven JPA, the incoming signal at the frequency of $\omega_0 - \delta\omega$ is amplified with a gain G and reflected back. Simultaneously, an idler mode with frequency $\omega_\mathrm{i} = \omega_0 + \delta\omega$ is created. The phase relation between the signal and idler modes is determined by the momentum conservation, whereas energy conservation demands $\omega_\mathrm{p} = \omega_\mathrm{s} + \omega_\mathrm{i}$. Intuitively, one can imagine this process as splitting of the pump photon into the pair of signal and idler photons [69].

In order to analytically describe the flux-driven JPA, a linear, semi-classical theory proposed by Yamamoto *et al.* [64] can be applied. This theory utilizes the input-output formalism borrowed from quantum optics. Starting from a classical harmonic oscillator, whose resonance frequency is modulated with the amplitude of $\epsilon/2$ and the frequency of $\alpha_\mathrm{p}\omega_0$, such that $\omega_0 \to \omega_0 \left[1 + \epsilon/2 \cos\left(\alpha_\mathrm{p}\omega_0 t\right)\right]$, one can derive the quantum mechanical Hamiltonian of the parametrically-modulated harmonic oscillator in terms of the creation and annihilation operators, $\hat{a}^\dagger$ and $\hat{a}$, respectively [64]

$$\hat{\mathcal{H}}\left(t\right) = \hbar\omega_0 \left[\hat{a}^\dagger\hat{a} + \epsilon\cos\left(\alpha_\mathrm{p}\omega_0 t\right)\left(\hat{a} + \hat{a}^\dagger\right)^2\right] \quad . \tag{2.49}$$

After adding a fictitious signal and loss ports connected to the oscillator and changing into a rotating frame, solving the Heisenberg equation of motion for the resonator field $\hat{a}$ allows us to obtain the characteristics of the JPA, such as its gain or bandwidth. Here, two cases can be differentiated: the nondegenerate and degenerate operating modes. In the nondegenerate mode, the pump frequency is not exactly twice the frequency of the input signal. There is a small offset $\delta\omega$, which means that $\omega_\mathrm{s} = \omega_\mathrm{p}/2 + \delta\omega$. In this case, the JPA acts as a phase-preserving amplifier, as the input signals are amplified independently of their phases (phase-preserving regime). The gain of the signal G_s and idler G_i modes are given by [64]

$$G_\mathrm{s}\left(\delta\omega\right) = \frac{\kappa_\mathrm{int}^2\delta\omega^2 + \left[\left(\kappa_\mathrm{int}^2 - \kappa_\mathrm{ext}^2\right)/4 - \epsilon^2\omega_0^2 - \delta\omega^2\right]^2}{\kappa_\mathrm{tot}^2\delta\omega^2 + \left[\kappa_\mathrm{tot}^2/4 - \epsilon^2\omega_0^2 - \delta\omega^2\right]^2} \quad , \tag{2.50}$$

$$G_\mathrm{i}\left(\delta\omega\right) = \frac{\kappa_\mathrm{ext}^2\epsilon^2\omega_0^2}{\kappa_\mathrm{tot}^2\delta\omega^2 + \left[\kappa_\mathrm{tot}^2/4 - \epsilon^2\omega_0^2 - \delta\omega^2\right]^2} \quad , \tag{2.51}$$

where κ_total is the total combined loss rate. We note, that these expressions are only valid for $\epsilon \leq \kappa_\mathrm{total}/\left(2\omega_0\right) = \epsilon_\mathrm{c}$. For $\epsilon > \epsilon_\mathrm{c}$, the JPA enters the regime of parametric oscillations. In our experiments, this can be observed when applying an excessively strong pump tone to the JPA. As for any phase-preserving amplifier, the Caves-House theorem [70, 71] imposes a lower bound on the noise photons A added to the amplified input signal

$$A \geq \frac{1}{2}\left|1 - \frac{1}{G_\mathrm{s}}\right| \quad . \tag{2.52}$$

We see that in the limit of high gain ($G \gg 1$), at least half a noise photon must be added to the signal. This is also known as the standard quantum limit (SQL) for phase-insensitive amplification. To go beyond the SQL, we can make use of the degenerate operating mode of the JPA. Here, we set $\omega_\mathrm{s} = \omega_\mathrm{p}/2, \delta\omega = 0$, and therefore, obtain $\omega_\mathrm{i} = \omega_\mathrm{s}$. In this operating mode the JPA acts as a phase-sensitive amplifier, as there is a fixed phase relation between the signal and the idler mode. This allows them to interfere constructively or destructively, depending on their relative phases. Therefore, the signal gain G_d depends on the phase θ between the pump and input signals and is given by [64]

$$G_\mathrm{d}(\theta) = \frac{\left[\frac{\kappa_\mathrm{ext}^2 - \kappa_\mathrm{int}^2}{4} + \epsilon^2\omega_0^2\right]^2 + \epsilon^2\kappa_\mathrm{ext}^2\omega_0^2 - 2\epsilon\kappa_\mathrm{ext}\omega_0\left[\frac{\kappa_\mathrm{ext}^2 - \kappa_\mathrm{int}^2}{4} + 4\epsilon^2\omega_0^2\right]\sin(2\theta)}{\left(\kappa_\mathrm{total}^2/4 - \epsilon^2\omega_0^2\right)^2} \quad . \tag{2.53}$$

As before, this relation only holds for $\epsilon \leq \epsilon_\mathrm{c}$. In this regime, in theory, the signal can be amplified without adding any noise, as stated by the Caves-Haus theorem [70, 71]. The noise photon numbers A_1 and A_2, added to the orthogonal quadratures of the signal with the respective gain of G_1 and G_2, are given by [70]

$$A_1 A_2 \geq \frac{1}{16}\left|1 - \frac{1}{\sqrt{G_1 G_2}}\right|^2 \quad . \tag{2.54}$$

If we now consider the case where one quadrature is deamplified, $G_1 < 1$, while the orthogonal one is amplified, $G_2 > 1$, the added noise can be zero if the condition $G_1 G_2 = 1$ is fulfilled. While losses, imperfections of the JPAs, or photon noise uncertainty in the pump tone inhibit noiseless amplification in real devices, it has been experimentally demonstrated that superconducting JPAs can overcome the standard quantum limit in the phase-sensitive regime [72].

Another important property of a JPA is its ability to generate squeezed states, which we have introduced in Sec. 2.1.2. For a squeezed state, the variances of the signal along different quadratures differ from each other. This makes the squeezing phenomenon closely related to the phase-sensitive amplification. When operating a flux-driven JPA in the phase-sensitive regime, we can generate a squeezed state by using a vacuum state as an input. One can show, that a direct connection of the JPA Hamiltonian in the interaction picture $\hat{H}_\mathrm{int}$ to the squeezing operator introduced in Eq. 2.18 can be made. For details on the derivation, we refer the reader to Ref. 32. In experiments, we can control the squeezing angle via the phase of the pump tone and the squeezing level via the pump power applied to the JPA.

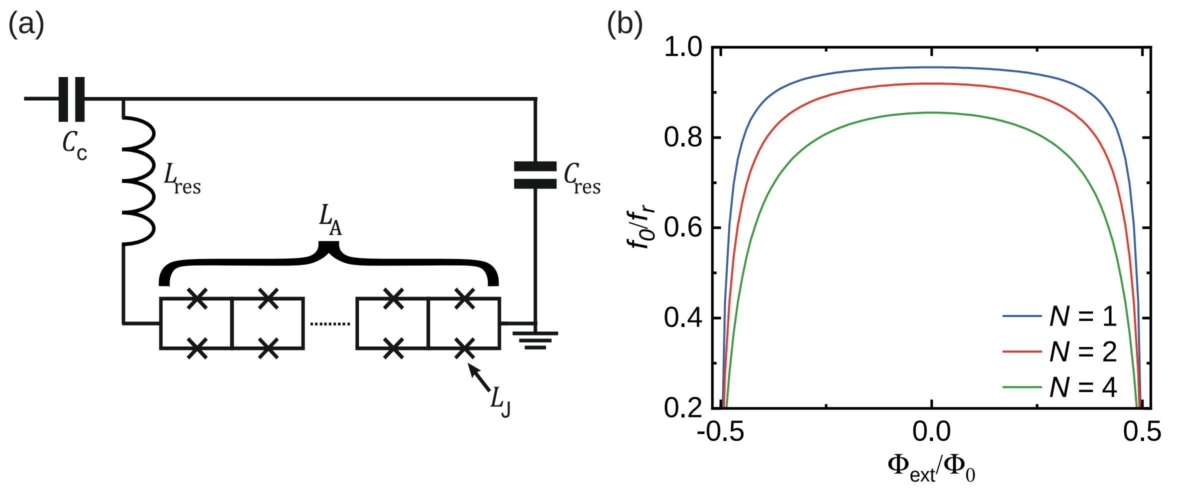

Figure 2.10: (a) Schematic drawing of the circuit used to model the multi-SQUID JPA. It features an array made from N dc-SQUIDs connected in series. Notably, we do not take the distributed nature of the CPW into account here. (b) Flux dependence of the resonance frequency for a SQUID array containing different numbers of dc-SQUIDs. The parameters used for this calculation are $I_c = 2\,\mu\text{A}$, $L_{\text{res}} = 2\,\text{nH}$ and $L_{\text{loop}} = 40\,\text{pH}$.

Effects of increased number of dc-SQUIDs

Lastly, we want to investigate the effects on the performance of a JPA when we switch out the single dc-SQUID for an array of N dc-SQUIDs connected in series. A schematic drawing of the JPA containing a dc-SQUID array is shown in Fig. 2.10(a). In order to theoretically describe this situation, we first start by introducing the array inductance [73]

$$L_{\text{A}} = NL_{\text{J}}\left(\frac{1}{2\cos(x) + \pi\beta_{\text{L}}\sin^2(x)} + \frac{\pi\beta_{\text{L}}}{4}\right) \quad . \tag{2.55}$$

Here, we define the ratio of the total flux penetrating the loop to the flux quantum $x = \pi\Phi_{\text{ext}}/\Phi_0$ as the frustration. From this, one can obtain the resonance frequency of the JPA as a function of a number of dc-SQUIDs [74]

$$f_0 = \frac{f_r}{1 + L_{\text{A}}/L_{\text{R}}} \approx f_r\left(1 - N\frac{L_{\text{S}}}{L_{\text{R}}}\right) \quad . \tag{2.56}$$

Here, we can see, that increasing the number of SQUIDs leads to a shift towards lower resonance frequencies and the resonance frequency as a function of applied flux has less of a rectangular shape, as can be seen from Fig. 2.10(b). Notably, the same behaviour is present when we keep the number of dc-SQUIDs constant, but decrease the critical current of the single Josephson junction by a factor of $1/N$. Therefore, in order to build a useful multi-SQUID JPA, it is necessary to increase the critical current, I_c, of the

Josephson junctions by a factor of N when adding dc-SQUIDs to the array. This allows us to maximize the range of working points of the JPA where the slope is neither too steep (makes the JPA too susceptible to flux noise), nor too flat (excessively strong pump signals are needed for modulation of the resonance frequency). The number of dc-SQUIDs also determines the dynamic range of the JPA. To quantify this, we are interested in the 1 dB-compression point P_{1dB} [61], which is the input signal power where the gain of the amplifier drops by 1 dB as compared to much weaker input signals. Here, one can find [73]

$$P_{\mathrm{1dB}} \propto \frac{\kappa_{\mathrm{ext}} + \kappa_{\mathrm{int}}}{|\alpha_{\mathrm{J}}|} \quad , \tag{2.57}$$

where α_{J} is the Josephson nonlinearitiy coefficient. We can therefore maximize the 1 dB-compression point by minimizing the Josephson nonlinearitiy coefficient. This nonlinearitiy inside a dc-SQUID is determined by the Josephson phase drop across its loop. By adding dc-SQUIDs to an array, the same phase drop is homogeneously distributed over many loops. Accordingly, this leads to an decrease of the effective nonlinearity of the dc-SQUID array compared to a single dc-SQUID. However, this picture only serves as an intuition, as a more detailed analysis shows that this argument is only valid, if the critical current is increased with the number of SQUIDs placed in the array. We can see this by defining the Josephson nonlinearitiy coefficient for the dc-SQUID array as [73]

$$\alpha_{\mathrm{J}} = -\frac{4\pi^2 f_0^2 p_{\mathrm{JPA}}^3}{2N^2} \quad . \tag{2.58}$$

Here, $p_{\mathrm{JPA}} = L_{\mathrm{A}}/(L_{\mathrm{A}} + L_{\mathrm{R}})$ is the participation ratio of the Josephson array inductance $L_{\mathrm{A}} \propto N$, and the total inductance, $L_{\mathrm{A}} + L_{\mathrm{R}}$, of the resonator. This shows that by increasing the number of dc-SQUIDs N, while simultaneously increasing the critical current I_c, one can achieve higher 1 dB-compression values, as compared to a single dc-SQUID design, by a factor of N^2 [74]. To make use of this fact, we utilize both single ($N = 1$) and double ($N = 2$) dc-SQUID JPAs throughout this thesis.

2.2.4 Broad-band amplification with a traveling wave parametric amplifier

The conventional JPAs are based on the CPW resonators. This approach allows one to increase an interaction time between the incident signal and the external pump, resulting in large amplification gains. However, this limits the amplification bandwidth as it depends on the cavity linewidth as well. Despite notable improvement regarding the 1 dB-compression values [75, 76] or the frequency range [57], the gain-bandwidth constraint imposed by the intrinsic resonator still represents a significant limitation for many applications, such as the frequency-multiplexed readout of qubits [77] or broadband entanglement generation [56]. To overcome this limitation, an alternative strategy can

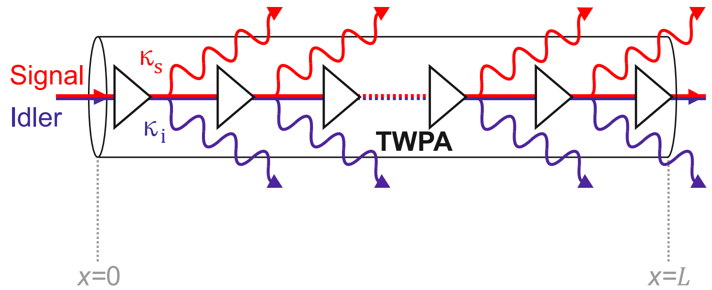

Figure 2.11: Schematic description of the distributed loss model of a generic TWPA: the signal and idler modes experience decay rates κ_s and κ_i, respectively, as they co-propagate through the TWPA with the length L. At the same time, they are amplified by a constant amount of gain per unit length.

be used. It exploits long chains of nonlinear elements (usually SQUIDs or SNAILs) to facilitate long interaction times between the incoming signal and the traveling parametric pump, thus, reaching high amplification gains. Such devices are known by the name Traveling Wave Parametric Amplifiers (TWPAs). They avoid the inherent gain-bandwidth trade-off associated with the cavity-based devices. In optics, fiber-optic TWPAs have demonstrated high gain, large dynamic range and broad bandwidth, while operating close to the SQL [78, 79]. Superconducting TWPAs in the microwave regime demonstrating sufficient gain and bandwidth have only been realized starting in the mid 2010s [80, 81]. A particular implementation of the TWPA is also a research subject of the current thesis.

Parametric amplification with the TWPA

The TWPA can be thought of as a nonlinear microwave transmission line, where the propagation velocity of the signal is controlled by inductance variation [82, 83]. Like the JPA described before, a strong pump tone is capable of achieving this goal which leads to a coupling between the pump and signal/idler tones via either three-wave ($f_p = f_s + f_i$) or four-wave ($2f_p = f_s + f_i$) mixing processes. The nonlinear medium of a TWPA in the microwave regime can be realized via the kinetic inductance of superconducting thin films (KTWPAs) [84] or via the Josephson junction-based metamaterials (JTWPAs). While KTWPAs can achieve saturation powers that are orders of magnitude larger than those of JTWPAs and bandwidths of greater than 8 GHz, the necessity of high pump powers (around 0.1 mW) poses many experimental challenges. Attenuation in the long transmission line (several meters) of the KTWPAs leads to heating, which increases temperatures in many applications and severely limits the noise performance of the respective amplifiers. Furthermore, the high pump powers often require pump cancellation methods to avoid saturation of next stages of amplification and demand strong isolation of the experiment from the pump tone [81]. These limitations have motivated the development of the

Josephson-based TWPAs with the goal to circumvent the aforementioned shortcomings.

Independent of the chosen design and approach, we can find a general expression for the gain of the TWPA by modelling it as a lossy, nonlinear waveguide with gain [85]. Here, we describe the TWPA as an array of independent loss ports, regularly spaced along the length of the TWPA, where each point introduces an independent loss channel for the signal and idler photons. These loss ports enable photons to leave the TWPA and also inject vacuum noise into the signal and idler modes. We describe their effects by the standard input-output theory [86] and label the injected bosonic noise modes from these ports as $\hat{\xi}_{\mathrm{s/i}}$. The coupling rates κ_{s} for the signal photons and κ_{i} for the idler photons are considered to be frequency and space independent. A scheme of this model can be found in Fig. 2.11. We only consider the limit where the spacing between the individual coupling ports x_j approaches zero, leading to a continuous loss and gain per unit length [87]. An imperfect phase matching between the signal, pump, and idler tones may lead to a non-zero mismatch $\Delta k = k_{\mathrm{p}} - k_{\mathrm{s}} - k_{\mathrm{i}}$ between the corresponding wavevectors. The Heisenberg-Langevin equation for the signal mode $\hat{a}_{\mathrm{s}}$ and idler mode $\hat{a}_{\mathrm{i}}$ describes the spatio-temporal evolution inside the TWPA [86]

$$\begin{aligned}\left(\partial_t + v\partial_x + \frac{i\Delta k}{2}\right)\hat{a}_{\mathrm{s}}(x) &= \chi\hat{a}_{\mathrm{i}}^{\dagger}(x) - \frac{\kappa_{\mathrm{s}}}{2}\hat{a}_{\mathrm{s}}(x) + \sqrt{\kappa_{\mathrm{s}}}\hat{\xi}_{\mathrm{s}}(x) \ , \\ \left(\partial_t + v\partial_x - \frac{i\Delta k}{2}\right)\hat{a}_{\mathrm{i}}^{\dagger}(x) &= \chi\hat{a}_{\mathrm{s}}(x) - \frac{\kappa_{\mathrm{i}}}{2}\hat{a}_{\mathrm{i}}^{\dagger}(x) + \sqrt{\kappa_{\mathrm{i}}}\hat{\xi}_{\mathrm{i}}^{\dagger}(x) \ . \end{aligned} \tag{2.59}$$

Here, v is the group velocity, which is assumed to be the same for signal and idler and χ is the parametric interaction strength. After moving to the frequency domain, one can find a scattering matrix $\mathbf{S}(x)$ that links the modes at the output of the TWPA, $x = L$, to those at the input, $x = 0$,

$$\begin{pmatrix}\hat{a}_{\mathrm{s}}\left[L,\omega\right] \\ \hat{a}_{\mathrm{i}}^{\dagger}\left[L,\omega\right]\end{pmatrix} = \mathbf{S}(L)\begin{pmatrix}\hat{a}_{\mathrm{s}}\left[0,\omega\right] \\ \hat{a}_{\mathrm{i}}^{\dagger}\left[0,\omega\right]\end{pmatrix}\frac{1}{v}\int_0^L \mathrm{d}x'\mathbf{S}(L-x')\begin{pmatrix}\sqrt{\kappa_{\mathrm{s}}}\hat{\xi}_{\mathrm{s}} \\ \sqrt{\kappa_{\mathrm{i}}}\hat{\xi}_{\mathrm{i}}^{\dagger}\end{pmatrix} \ . \tag{2.60}$$

For a detailed derivation of the elements of the scattering matrix, we refer the reader to Ref. 86. In the case of perfect phase matching ($\Delta k = 0$) and symmetric loss ($\kappa_{\mathrm{s}} = \kappa_{\mathrm{i}} = \kappa$), we find that the TWPA gain is frequency-independent and can be expressed by [86]

$$G = e^{-\kappa L/v}\cosh^2(L\chi/v) \approx \frac{e^{(2\chi-\kappa)L/v}}{4} \ . \tag{2.61}$$

We can see that, in theory, one could arbitrarily increase the gain of a perfectly phase-matched TWPA simply by increasing its length. However, for real devices, various nonlinear effects or pump depletion cause significant deviations from this exponential behaviour.

Phase matching

Independent of the design used for the TWPA, efficient traveling wave amplification requires fulfillment of two conditions: an impedance matching of the amplifier to the impedance of the external environment and a proper phase matching [88]. The phase mismatch in these TWPA devices arises mainly because of two reasons: dispersion phase mismatch due to the chromatic dispersion relation of the metamaterial [89] and the Kerr phase mismatch, caused by higher-order nonlinear processes. The latter include effects such as the self-phase modulation (SPM) and the cross-phase modulation (XPM) [82]. These effects increase the phase velocity of the pump tone compared to the signal and idler tones. Here, SPM and XPM are causing the signal to accumulate an additional phase-shift proportional to its own power (SPM) or proportional to the intensity of another co-propagating wave (XPM) [61, 88]. For a TWPA, where the pump, signal, and idler tones co-propagate along a common transmission line, the dominating phase shifts are introduced by SPM for the pump tone and by XPM for the signal and idler tones. When we theoretically consider the effects of the imperfect phase matching ($\Delta k \neq 0$) on the overall gain of the TWPA, we obtain [86]

$$G \approx e^{-\kappa L/v} e^{2L\mathrm{Re}(\tilde{\chi})/v} \left| 1 - \frac{i\Delta k}{2\tilde{\chi}} \right|^2 \quad , \tag{2.62}$$

where we introduced the complex parametric interaction amplitude

$$\tilde{\chi} = \sqrt{\chi^2 + \left(\frac{i\Delta k}{2}\right)^2} \quad . \tag{2.63}$$

From this equation we can see that the finite phase mismatch decreases the overall gain. For large Δk the effective interaction amplitude $\tilde{\chi}$ becomes purely complex, meaning that there is no amplification, as $|G| < 1$ [90, 91].

Several strategies can be adopted for addressing the issue of phase matching. The first approach is to minimize Δk via dispersion engineering. It is based on engineering a gap in the dispersion relation of the metamaterial. This allows to fulfill the phase matching condition for a specific pump frequency close to the gap frequency. This gap can be implemented via various periodic loading patterns [84, 92], or by introduction of resonant elements alongside the metamaterial itself [80, 81, 90, 93]. The second method to address the phase mismatch is based on tuning the Kerr-nonlinearity itself. Here, one can use the SNAILs to either periodically change the sign of the Kerr-nonlinearity by alternating the polarity of the SNAIL elements [94, 95], or to choose such a working point, where the Kerr-term is virtually zero [56]. The latter approach is the one chosen for the TWPA studied in this thesis: Specifically, we analyze a JTWPA implemented in a coplanar waveguide transmission line design, where the center conductor consists of an

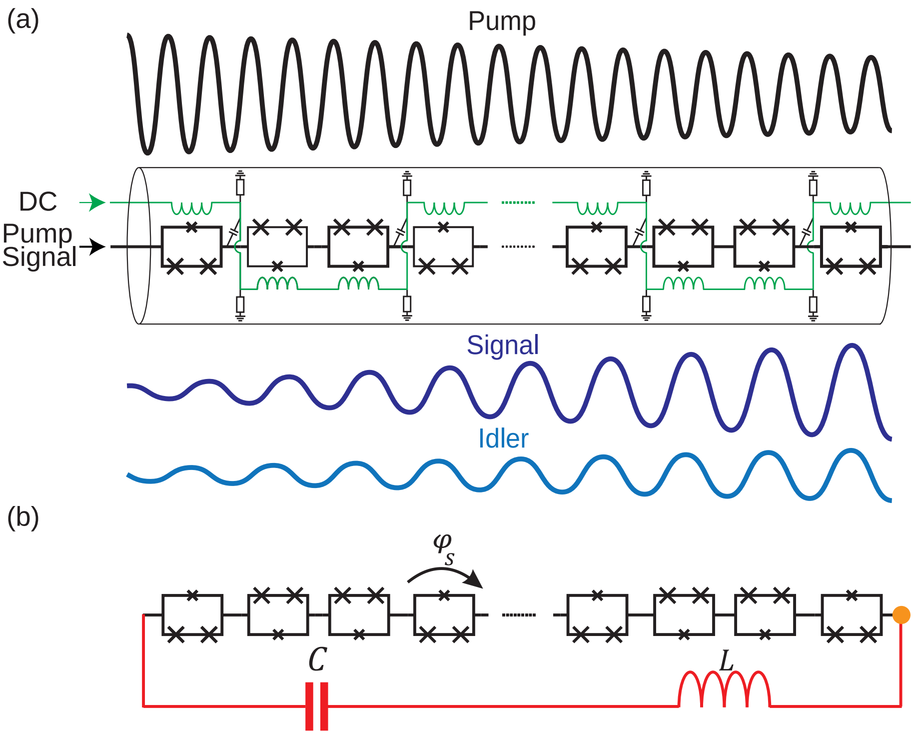

Figure 2.12: (a) Schematic of the JTWPA, where the center conductor is composed of a SNAIL array (black). The on-chip dc lines (green) are used to create a magnetic flux bias. The pump and signal tones enter at the combined input port. Wavelengths and different elements of the TWPA are not to scale. This scheme of the SNAIL array and the flux bias line has been introduced in Ref. 56. (b) Single-mode lumped-element circuit model for the JTWPA, where the array of SNAILs is placed in series with a linear inductance and capacitance (red). The orange dot indicates the node between the array of SNAILs and the linear inductance.

SNAIL array of 1632 SNAILs. For flux biasing of the SNAILs, an on-chip magnetic flux bias line is used. A scheme of the TWPA can be found in Fig. 2.12(a). The resistors shown provide low-pass filtering to the flux bias line and also function as effective air bridges, equalizing potentials across the JTWPA.

In order to obtain the three-wave mixing and Kerr-terms in this JTWPA, we can utilize the results obtained for the SNAIL in Sec. 2.2.2. However, we have to expand this theory, as we are not interested in the behaviour of a single SNAIL, but rather in the array of M identical SNAILs embedded into the CPW transmission line. Here, a careful consideration of the nonlinear current conservation is needed. To this end, we assume that the SNAIL array can be approximated as a simple lumped element circuit, in which the array of M SNAILs is placed in series with a linear inductance L and capacitance C and the Josephson phase splits equally among the individual SNAILs [57]. This circuit is illustrated in Fig. 2.12(b). Notably, this model is very similar compared to the one we used for the multi-SQUID JPA (see Fig. 2.10(a)). In order to obtain the Taylor expansion of the total potential energy of the SNAIL array, we follow the results presented in Ref. 57. We consider φ as the mode canonical phase coordinate and obtain the potential energy U_T of the whole circuit as

$$U_T(\varphi, \varphi_s) = MU_S(\varphi_s) + \frac{1}{2L}\varphi_0^2(\varphi - M\varphi_s)^2 \quad , \tag{2.64}$$

where $\varphi_0 = \Phi_0/2\pi$ is the reduced flux quantum. Here, the coordinate φ_s is not an independent variable anymore but a function of the phase coordinate φ. In order to obtain a relation between φ_s and φ, we make use of the nonlinear current conservation for the node between the SNAIL array and the linear inductance [57]

$$\alpha I_c \sin(\varphi_s) + I_c \sin\left(\frac{\varphi_s - \varphi_{\mathrm{ext}}}{2}\right) + I_c\frac{L_J}{L}(M\varphi_s - \varphi)^2 \quad . \tag{2.65}$$

The node between the SNAIL array and the linear inductance is indicated by the orange dot in Fig. 2.12(b). This equation allows us to write the potential energy in terms of the single degree of freedom φ

$$U_T(\varphi) = MU_S(\varphi_s[\varphi]) + \frac{1}{2L}\varphi_0^2(\varphi - M\varphi_s[\varphi])^2 \quad . \tag{2.66}$$

For the regime of small phase fluctuations, we can expand the potential $U_T(\varphi)$ around the minimum $\tilde{\varphi}_{\mathrm{min}}$ into the Taylor series and obtain the expansion coefficients $\tilde{c}_n$, which can be related to the coefficients c_n of a single SNAIL via [57]

$$\tilde{c_2} = \frac{p_{\mathrm{amp}}}{M}c_2, \quad \tilde{c_3} = \frac{p_{\mathrm{amp}}^3}{M^2}c_3, \quad \tilde{c_4} = \frac{p_{\mathrm{amp}}^4}{M^3}\left(c_4 - \frac{9c_3^2}{4c_2}(1 - p_{\mathrm{amp}})\right) \quad , \tag{2.67}$$

where $p_{\mathrm{amp}} = \frac{ML_J/L}{2c_2 + ML_J/L} = \frac{ML_s}{L+ML_s}$ is the linear participation ratio between the inductance of the array, $L_s^{\mathrm{array}} = ML_s$, and the linear inductance L. The 4WM (Kerr-term) is connected to $\tilde{c_4}$. We can see that optimizing the single SNAIL with regards to c_3 and c_4 leads to a strong suppression of the effective Kerr-term $\tilde{c_4}$ while still retaining a sufficiently large 3WM term via $\tilde{c_3}$, as required for parametric amplification. We want to note, that due to $\tilde{c_4}$ being dependent both on c_3 and c_4, a vanishing c_4 is not sufficient to obtain a Kerr-free situation for the SNAIL array. While these results of the simple lumped-element model introduced in Sec. 2.2.2 may not be directly applicable to the TWPA as such, it is expected that similar observations will hold for coupled-mode equations [89, 96], that describe the waves propagating along the TWPA [97]. From Eq. 2.67, combined with Fig. 2.6, we can see that at zero flux bias the SNAIL nonlinearity does not allow for 3WM. However, as indicated by Fig. 2.6, increasing the flux bias to $\Phi_{\mathrm{ext}} \approx 0.4\,\Phi_0$ allows for 3WM and is combined with strongly suppressed 4WM.

In order to further improve gain of the TWPA, the design utilized in this work has a nonlinear dispersion curve that is superlinear at the second harmonic generation (SHG) frequency of the pump tone [56]. The primary origin of this superlinear dispersion is a stopband near the SHG frequency, induced by the periodic loading of the TWPA with spiral resonators [96]. In particular, this nonlinear dispersion enables the control of the phase mismatch of the second harmonic generation. The nonlinear dispersion can be tuned in such a way that it allows for a weak and cascaded mixing process based on this second harmonic generation [98]. During this process, SHG is followed by a downconversion of the frequency-doubled microwaves back to the pump frequency [99]. This process introduces a phase shift to the pump tone, based on the imperfect phase matching of the SHG, $\Delta k_{\mathrm{SHG}} \neq 0$. At an optimal combination of SHG phase mismatch Δk_{SHG}, amplification phase mismatch Δk, and pump power, the pump tone accumulates a phase shift from inefficient SHG, that exactly compensates for the phase mismatch between the pump, signal, and idler tones Δk [99]. Effectively, this phase shift accumulated by the pump tone looks like 4WM and compensates for the remaining Kerr-effect within the device [56]. This effect is well known in the field of nonlinear optics [100] and allows for several adjustments for optimizing the TWPA performance during its operation. First, we can adjust the pump frequency in order to vary the amplification phase mismatch Δk. Second, we can adjust the pump power. Last, we can shift the magnetic flux bias Φ_{ext} to tune the 3WM and 4WM terms. With regards to the phase shift introduced by process described above, an offset of the optimal flux bias, which corresponds to a zero Kerr-term, may improve the overall phase matching. [99]. Therefore, we need to scan the three-dimensional parameter space spanned by pump frequency, pump power and flux bias in order to find an optimal working point for the TWPA.

Noise performance and squeezing

The noise added to the amplified signal is another important property of all parametric amplifiers. If we consider the noise spectral density S_{added} added to the signal amplified by the TWPA, we obtain [86]

$$S_{\mathrm{added}} \approx \frac{1}{2} + \frac{1}{2\chi - \kappa}\left(\kappa + \frac{\Delta k^2}{4\chi(2\chi - \kappa)}\right) \quad , \tag{2.68}$$

where χ is the parametric interaction strength and κ is the coupling rate to the loss ports along the TWPA for both the signal and idler photons. Here, we see that losses and phase mismatches increase the added noise above the SQL value of 1/2. We can consider the same imperfections for the task of vacuum squeezing by analyzing the squeezed quadrature variance, σ_{s}^2. For perfect phase matching, we can obtain [86]

$$\sigma_{\mathrm{s}}^2 = \frac{1}{4(\kappa + 2\chi)}\left(\kappa + 2\chi e^{-2L\chi/v} e^{-\kappa L/v}\right) \quad . \tag{2.69}$$

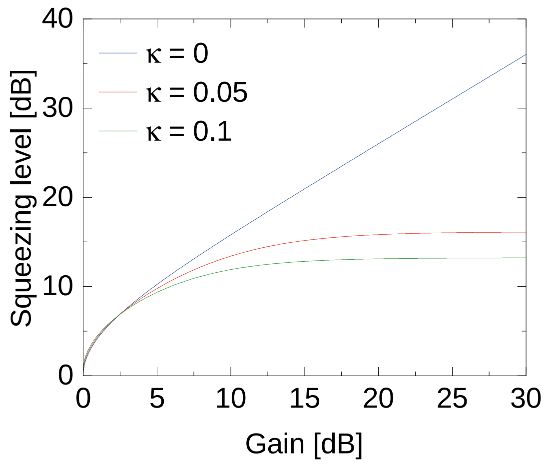

Figure 2.13: Squeezing level obtained with the distributed loss model. The squeezing level is plotted as a function of TWPA gain, which is controlled by varying the length L according to Eq. 2.61. We set $\chi/v = 1$ and change the coupling rate to the loss ports along the TWPA, κ, between the different graphs. Here, we assume equal coupling rates for the signal and idler photons, $\kappa = \kappa_\mathrm{i} = \kappa_\mathrm{s}$. As we increase gain, squeezing saturates for the case of non-zero κ. The blue curve ($\kappa = 0$) represents the squeezed variance of an ideal, lossless TWPA.

This corresponds to a squeezing level of

$$S = -10\log_{10}\left(\frac{1}{(\kappa+2\chi)}\left(\kappa + 2\chi e^{-2L\chi/v}e^{-\kappa L/v}\right)\right) \quad . \tag{2.70}$$

From this, we can see that, theoretically, taking the large-length limit is always beneficial, as the squeezing level increases monotonically with L, saturating at $-10\log_{10}(\kappa/(2\chi+\kappa))$. This saturation can be seen from Fig. 2.13 where we plot the theoretical squeezing level S. However, in experiments, increasing the length of the TWPA also increases the total losses, which limits the final squeezing. Up to this point, we only considered a decay rate κ that is constant along the length of the TWPA. However, we can also consider a spatially varying decay rate $\kappa = \kappa(x)$. For such a decay rate, the squeezed quadrature variance takes the form [86]

$$\begin{aligned}\sigma_\mathrm{s}^2 &= e^{-\frac{1}{v}\int_0^L \mathrm{d}x\kappa(x)}e^{-2L\chi/v} \\ &+ \frac{1}{v}\int_0^L \kappa(x)e^{-\frac{1}{v}\int_x^L \mathrm{d}x'\kappa(x')}e^{-2\chi(L-x)/v} \quad ,\end{aligned} \tag{2.71}$$

where the second term corresponds to the contribution from vacuum fluctuations injected from the loss ports. When taking the large length limit and assuming $\chi \gg \kappa(x)\ \forall x$, the contribution from the added noise integral is exponentially insensitive to noise coupled into the system close to the input port, as the vacuum fluctuations coupling to the loss ports of the TWPA are themselves squeezed by the TWPA interaction [86].

It is also important to note that the TWPAs, as well as JPAs, always produces TMS states in the degenerate regime due to their finite bandwidths. Here, correlations exist between quadratures of different frequency modes, which are symmetrically spaced around half the pump frequency [101, 102]. During the parametric amplification process, the 3WM process converts a single pump photon (ω_p) into an entangled pair of photons in the signal (ω_s) and idler (ω_i) mode. When $\omega_\mathrm{s} \neq \omega_\mathrm{p}/2$, energy conservation places the idler photon at a different frequency than the signal photon, which leads to the formation of frequency-nondegerate two-mode squeezing and quantum entanglement. Due to the inherently broadband nature of TWPAs, this continuous variable (CV) entanglement can be achieved between microwaves with a frequency-spacing of up to several GHz [56, 93].

Chapter 3

Experimental techniques

In this chapter, we present the experimental methods and techniques used to generate and measure quantum microwave states. To realize these experiments, we rely on cryogenic and room-temperature microwave setups in combination with an accurate signal reconstruction. In Sec. 3.1, we introduce our basic cryogenic experimental setup. In Sec. 3.2, we focus on our microwave tomography setup, including the data acquisition using a field-programmable gate array (FPGA) and the reconstruction of the quantum states.

3.1 Cryogenic setup

In our experiments, we investigate properties of propagating quantum microwave states at the frequencies of 3 GHz to 12 GHz. To avoid noise in these states and preserve quantum coherence, the relation $k_{\mathrm{B}}T \ll hf$ needs to be fulfilled, which demands for temperatures of less than 50 mK. In order to achieve these millikelvin temperatures, we employ cryostats utilizing dilution cooling. This method is based on the phase separation of a $^{3}\mathrm{He}/^{4}\mathrm{He}$ mixture at low temperatures. Experiments presented in this thesis have been performed in two different dilution refrigerators. For the TWPA (Sec. 4.2) and two-dimensional PNCF measurements (Sec. 4.3), we use a commercially built cryostat located in the Bob lab. For the JPA measurements (Sec. 4.1), we use a home-built dry dilution cryostat located in the Alice lab. In the following, we will call these cryostats Alice and Bob, respectively. In Chapter 5 we introduce a cryogenic link connecting these Alice and Bob cryostats which serve as a basis for quantum state transfer and entanglement distribution.

Bob cryostat

The dilution cryostat located in the Bob lab is a commercial Oxford Instruments (OINT) Triton system. It consists of five different temperature stages, namely, the two pulse tube stages (PT1 and PT2), the distillation (still) stage, the cold plate, and the mixing chamber stage. When the cryostat is closed, each stage is covered by cylindrical shields blocking thermal radiation emitted from the adjacent stages. For the PT1 and PT2 stages, these shields are made out of aluminum while the innermost shields, covering still and mixing chamber stage, are made from copper. Additionally, the PT1 shields are covered by a superinsulation foil consisting of 10 layers of aluminized polyester foil separated by a polyester spacer material. The different stages of the cryostat are placed inside an outer vacuum chamber (OVC). This allows us to operate the cryostat inside a high vacuum ($\approx 1 \times 10^{-6}$ mbar) preventing the thermal coupling between adjacent temperature stages. A photograph of the opened Bob cryostat indicating the different stages can be found in Fig. 3.1(a). The first two stages are cooled by a Cryomech PT415-RM pulse tube refrigerator (PTR) to the temperatures of 50 K and 4 K, respectively. These stages, in conjunction with a Joule-Thomson (JT) impedance, are used for precooling of the ^{3}He/^{4}He mixture. The Joule-Thomson impedance, where cooling of the compressed gas is based on isenthalpic expansion, is connected to the still, which has a temperature of roughly 1 K. A continuous counter flow heat exchanger connects the still stage to the cold plate and cools the incoming mixture down to less than 100 mK. Lastly, the mixture reaches the coldest part of the cryostat, the mixing chamber, which can reach temperatures as low as 15 mK. Here, the cooling power is generated by dilution cooling which occurs due to the enthalpy difference between the ^{3}He-rich (incoming) and the ^{3}He-diluted (outgoing) mixture. The diluted ^{3}He flows from the mixing chamber to the still, where mainly ^{3}He is pumped out utilizing a turbo-molecular pump backed by a scrolls pump. To filter out any contaminants like water vapour, nitrogen, hydrogen, and other gases, an external liquid nitrogen (LN2) cold trap, as well as two cold traps inside the cryostat (on PT1 and PT2) are used.

The Bob cryostat is equipped with four stainless steel (SS) coaxial microwave input lines[1]. The choice of stainless steel cables results in a good thermal isolation between the neighbouring temperature stages of the cryostat due to its low thermal conductivity, but comes at the cost of high losses of 5.9 dB/m at the frequencies around 5 GHz and temperatures of 4 K. However, typically, our rf-sources can provide enough output power to compensate for these losses. At each temperature stage of the cryostat, microwave attenuators are thermalized to the respective plate. For the two dedicated input signal lines, we choose a total attenuation of 56 dB to reduce the blackbody radiation entering the cables at room temperature to a thermal photon occupation number of few 10^{-3} at the sample stage. This blackbody radiation is also known as Johnson-Nyquist noise. In order to reduce the thermal load on the lower temperature stages, we distribute the attenuation across the different temperature stages. This is done in such a way, that the remaining noise from higher stages matches the thermal noise coupled from the respective stage itself. The pump input lines have a total attenuation of only 44 dB. This limited attenuation stems from a limited dynamical range of our microwave generators and the strong pump tones required at the sample. The two output lines in the Bob cryostat are made from superconducting coaxial cables[2] (SC) up to the high-electron-mobility

[1]We use SC-219/50-SS-SS, Coax Co., Ltd stainless steel cables.
[2]We use SC-219/50-NbTi-NbTi, Coax Co., Ltd superconducting cables.

transistor (HEMT) amplifiers[3] placed on the PT2 stage. Afterwards, we use silver-plated SS cables (SSS)[4]. According to Friis formula [103] a slight increase in losses after strong amplification, $G \gg 1$, has only a minimal impact on the overall signal-to-noise ratio, which allows us to exploit the low thermal-conductance of the SSS cables. Two microwave isolators[5] are placed in each of the output lines and are mounted to the mixing chamber plate. They are used to provide an isolation of around 40 dB, protecting from noise and microwave reflections from the higher temperature stages and HEMTs.

For the cryostat thermometry and distribution of dc-currents we use two dc-looms containing 12 twisted wire pairs each. At the temperatures higher than 3 K, we use BeCu-looms soldered to a 24 pin LEMO connector at the vacuum feed-through. After the PT2 stage, we use a superconducting loom made from NbTi. These two looms are connected via microminiature D-connectors. At the mixing chamber stage, each loom is soldered to a 24-pin Buerklin microconnector anchored to the mixing chamber plate via a gold-plated oxygen-free high thermal conductivity (OFHC) copper housing. The four-wire temperature measurement and the dc-currents can be routed through different looms to avoid crosstalk. A third loom, connecting the room temperature plate and the PT2 stage, is used for the HEMT power supply. All of the looms are thermalized at different temperature stages by pressing them between two gold-plated OFHC copper plates together with Kapton foil. Lastly, the cryostat has a fourth loom for the in-built thermometry. Both of the resistance bridges used are equipped with external preamplifiers which are placed as close as possible to the cryostat to reduce noise influencing the measurement process. In our case, this is achieved by placing them on top of self-made filterboxes, which are directly plugged into the vacuum feedtrough of the cryostat. These filterboxes contain RCL low-pass filters with the cutoff frequency of 10 kHz [104–106].

Alice cryostat

The Alice cryostat, housing the experimental setup for quantum teleportation of propagating microwaves, is a home-built dry dilution refrigerator. It has been designed and constructed at Walther-Meißner-Institut [107, 108]. Compared to the Bob cryostat, there is no JT impedance in the Alice fridge, but there is an additional temperature stage, where cooling is realized by a ^{4}He 1K-loop. This cryostat is equipped with eight stainless steel microwave input lines and four output lines utilizing the same kind of HEMT amplifiers as in the Bob cryostat. Three of the input lines have 70 dB of microwave attenuation combined with low-pass cryogenic filters[6]. Five lines have 26 dB of added attenuation. For additional details about the wiring and thermometry in the Alice cryostat we refer the reader to Ref. 5.

[3]We use LNF-LNC4 8C, Low Noise Factory, HEMT amplifiers.
[4]We use SC-219/50-SSS-SS, Coax Co., Ltd silver-plated stainless steel cables.
[5]We use CTH11 84-KS18, Quinstar Technology, Inc, Isolators.
[6]We use a K&L 6L250-12000/T26000 low pass filter with a cut-off frequency of 12 GHz.

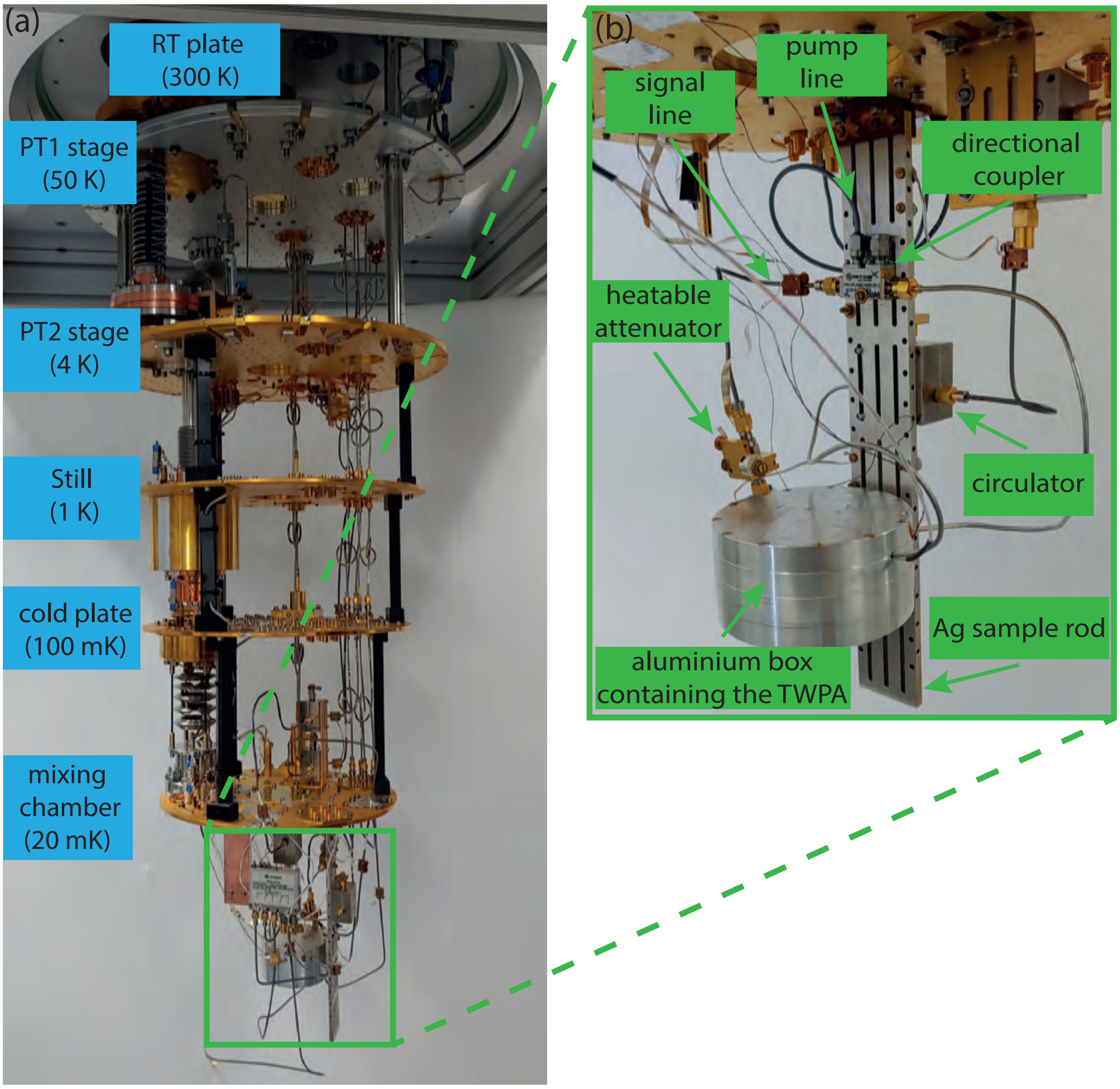

Figure 3.1: (a) Photograph of the Oxford Instruments Triton ^{3}He/^{4}He dilution refrigerator with respective temperature stages. Carbon fiber struts are used to hold the stages with a minimal thermal coupling between adjacent stages. (b) Photograph of the sample stage holding the TWPA setup. The silver (Ag) sample rod is directly mounted to the mixing chamber plate using OFHC copper brackets.

3.2 Data acquisition

In this section, we describe the methods we use to detect and reconstruct propagating quantum signals in the microwave regime. First, we present the room temperature setup. To this end, we introduce a microwave receiver setup which is used to down-convert incoming microwave signals to the intermediate frequencies around 11 MHz before they get digitized by the FPGA. Next, we discuss the photon number conversion factor (PNCF) measurements. We conclude this section by presenting the reference state reconstruction method which is used to reconstruct quantum states from the measured data.

3.2.1 Room temperature setup

Here, we introduce a general measurement setup used in our experiments. We use Rohde & Schwarz SGS 100A microwave sources for generation of coherent signals. These can be used either as input signals or pump tones in the JPA and TWPA experiments. Here, both in the Bob and in the Alice lab, we use one of such generators to serve as a local oscillator (LO) for the dual path microwave receiver. The rf-sources used for generation of strong coherent pump tones are additionally equipped with two highpass filters[7] in order to remove spurious subharmonics. All of the sources can be operated in the pulsed regime modulated by external devices. To this end, we use an arbitrary waveform generator (HDAWG, Zurich Instruments) in the Bob lab or a data timing generator (DTG 5334, Tektronix) in the Alice lab. Figure 3.2(b) shows the detailed pulsing scheme used in the Bob lab. The signals leaving the cryostat are further amplified by room temperature amplifiers[8]. Those are kept at a constant temperature by a Peltier cooler stabilized around the temperature of 19.5 °C. The signals are detected either directly with a Rohde & Schwarz ZNA26 vector network analyzer (VNA) or by the microwave receiver discussed in the next section. All microwave devices are referenced to a Stanford Research FS725 10 MHz rubidium frequency standard, as illustrated in Fig. 3.2(b). In the Alice lab, Agilent N1810TL and N1812TL microwave switches are used to switch between different inputs and output lines and to chose the desired detection method.

3.2.2 FPGA data acquisition

Direct VNA measurements can be used for pre-characterization measurements of JPAs and TWPAs but are unsuitable for performing quantum state tomography and the measuremnt of subtle quantum properties, such as vacuum squeezing. For the latter purposes, we employ a custom heterodyne microwave receiver. A picture of such a receiver, used in the Bob lab, can be found in Fig. 3.2(a). The receiver we use in the Alice lab is similar in the design. Therefore, we will not differentiate between them in our discussion. A

[7]We use VHF-8400+, Mini-Circuits, highpass filters with a cut-off frequency of 8.4 GHz.
[8]We use AMT-A0033, Agile MwT, RF-Amplifiers.

schematic drawing containing the microwave setup we use to perform measurements in the Bob lab is illustrated in Fig. 3.2(b). First, we amplify the signal leaving the sample stage of the cryostat with the HEMT and the Peltier-cooled room temperature rf-amplifier. Next, we use a Mini-Circuits VBFZ-5500-S+ bandpass filter with a passband from 4.9 GHz to 6.2 GHz to filter the signal around the desired detection frequency f_{RF}. In the next step, we utilize a strong, independent local oscillator (LO) signal at a frequency of $f_{\mathrm{LO}} = f_{\mathrm{RF}} + f_{\mathrm{IF}}$ to down-convert the signal to an intermediate frequency (IF) of $f_{\mathrm{IF}} = 11\,\mathrm{MHz}$ in the Alice lab and $f_{\mathrm{IF}} = 12.5\,\mathrm{MHz}$ in the Bob lab. For the downconversion process, we make use of an image rejection mixer (IRM4080B, Polyphase), which filters out the blue sideband at $f_{\mathrm{RF}} + 2f_{\mathrm{IF}}$. This step is crucial for correct reconstruction of squeezed states [5]. The IF-frequencies in both labs are detuned from the 10 MHz reference to avoid interference. We choose the IF-frequency in the Bob lab in such a way that the FPGA sampling frequency $f_{\mathrm{S}} = 125\,\mathrm{MHz}$ is an integer multiple to the IF-frequency. The receiver is equipped with two identical paths, where a mechanical phase-shifter allows us to adjust the relative phase between them and step attenuators (ESA2-1-10/8-SFSF, EPX microwave Inc) can be adjusted to balance the signal between the two paths of the receiver and to avoid compression effects during the following amplification. Before and after further amplification of the IF-signal (AU-1447-R, Miteq), we use Mini-Circuits SLP-21.4+ to low-pass filter the signals with a bandwidth of 0-22 MHz. Lastly, the signals are digitized by a NI-5782 transceiver module in conjunction with a PXIe-7975R FPGA for data processing. The FPGA allows us access to the statistical moments of the down-converted signals. For further information about the FPGA image used we refer the reader to Ref. 109.

3.2.3 Output line calibration

An outstanding challenge in all quantum microwave experiments is how to relate measured classical quantities (voltages, currents, etc.) to their quantum counterparts (photon numbers, wavefunction probability amplitudes, etc.) somewhere deep in the cryogenic setup or on-chip. One of the common solutions for this problem is to embed a reference source (for instance, of photons) in the experimental setup to be used later for an in-situ calibration. This calibration method gives us access to the so-called photon number conversion factor (PNCF) for each output line. The PNCF calibration provides the total gain and noise numbers for each output. To obtain the PNCF, we need a photon source emitting a signal with an accurately known photon number. We discuss various photon sources with this property in more detail in Sec. 4.3.1. For our measurements, we use a 30 dB heatable attenuator placed in the input line, which acts as a source of black-body radiation. The electromagnetic power emitted by the attenuator is determined by its temperature, which can be varied and stabilized using an external PID control loop. This

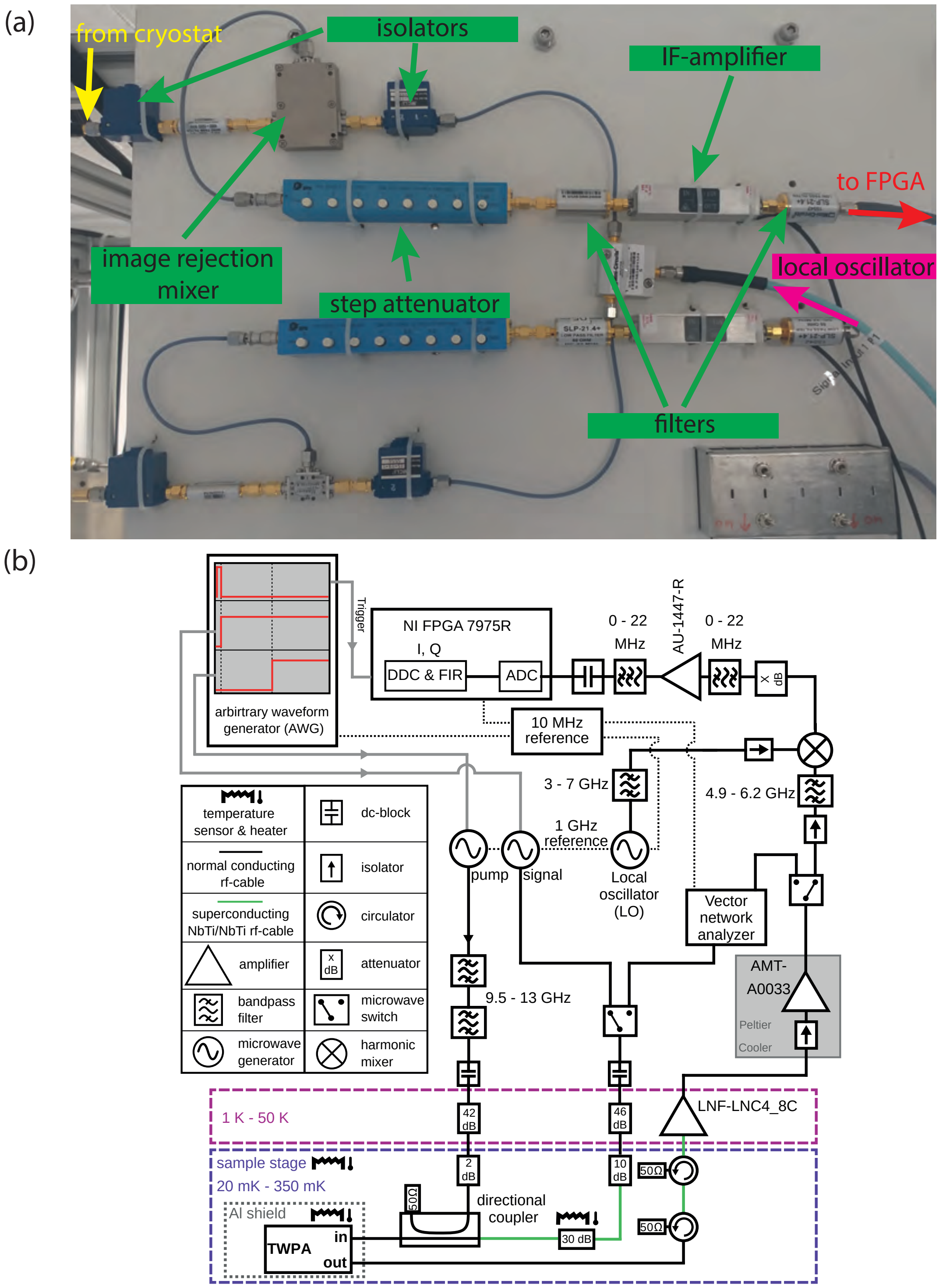

Figure 3.2: (a) Photograph of the dual path receivers used in the Bob lab. Here, only one of the two paths is used. (b) Microwave setup used for the TWPA measurements in the Bob fridge. One of the rf-sources (the LO) is directly connected to the 10 MHz reference. The remaining rf-sources are referenced to a 1 GHz signal emitted by the LO.

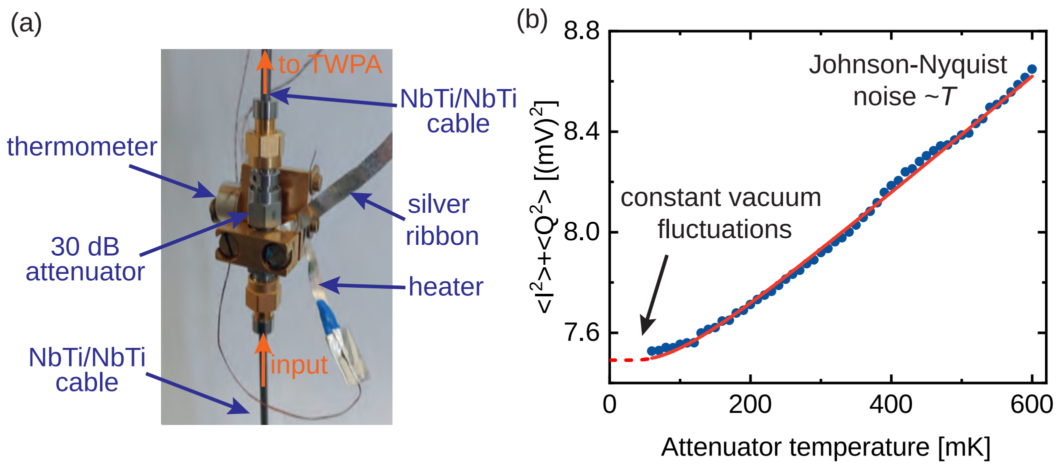

Figure 3.3: (a) Photograph of the heatable attenuator used in the Bob fridge. All of the components are mounted to a gold-plated OFHC copper holder that is clamped to the 30 dB attenuator. (b) Results of a PNCF measurement performed during the TWPA characterization. Symbols depict the experimental data and the solid red line is the corresponding fit according to Eq. 3.2, which yields $n = 9.41 \pm 0.21$ and $\kappa = 1.31 \pm 0.03\,(\mathrm{mV})^2$. The carrier frequency is $f_0 = 5\,\mathrm{GHz}$ and the detection bandwidth is $\Omega = 400\,\mathrm{kHz}$. The dashed line is an extension of the fit beyond the measured data indicating the constant vacuum noise at low temperatures, $k_\mathrm{B}T \ll \hbar\omega$.

PID loop makes use of a thermometer and a $100\,\Omega$ heater attached to the opposite sides of a OFHC copper frame holding the attenuator. For the temperature control, we use an AC Lakeshore resistance bridge, model 370, in the Alice lab and a Picowatt AVS 48SI resistance bridge in the Bob lab. A thin silver ribbon, clamped around the attenuator and connected to the mixing chamber plate, is used for thermalization. Since the attenuator temperature must be varied in a wide range of temperatures (50 mK to 1 K), the thickness of the ribbon is chosen in such a way that it provides a good compromise for coupling to the mixing chamber, which must stay at 50 mK at all times. A photograph of the heatable attenuator used in the Bob cryostat can be found in Fig. 3.3(a). The power spectral density $S(T)$ emitted by this attenuator at a temperature T_att and a frequency f_0 is given by [19]

$$S(T_\mathrm{att}) = \frac{hf_0}{2}\coth\left(\frac{hf_0}{2k_\mathrm{B}T_\mathrm{att}}\right) \quad . \tag{3.1}$$

Therefore, the total power measured at room temperature with the FPGA can be written as

$$P(T_\mathrm{att}) = \frac{\kappa}{R}\left[\frac{1}{2}\coth\left(\frac{hf_0}{2k_\mathrm{B}T_\mathrm{att}}\right) + n\right] \quad . \tag{3.2}$$

Here, κ is the PNCF, defined as $\kappa = G\,R\,B\,hf_0$, where B is the detection bandwidth, $R = 50\,\Omega$, G is the combined gain of the amplification chain, and n is the total noise, containing contributions from the HEMT noise and from the system itself. Figure 3.3(b) shows the exemplary result of such a Planck spectroscopy measurement. Here, two distinct regions are visible: for large temperatures, $k_B T \gg h f_0$, S reduces to the classical, linear Johnson-Nyquist noise spectral density, proportional to T. For temperatures lower than roughly 70 mK, the noise spectral density becomes constant due to dominance of temperature-independent vacuum fluctuations. Furthermore, we need to take the effect of finite microwave losses between the photon source, i.e. the heatable attenuator, and a desired reconstruction point of our quantum signal into account. To this end, we model these losses with a beam splitter model, where the incoming signal gets attenuated and a thermal state, with the mean photon number corresponding to the bath temperature, gets coupled to the microwave line. In most of our experiments, we estimate these losses from datasheet values of the passive devices or cables. However, actual losses may deviate from these estimated values due to many reasons. The central cause for these deviations is that the datasheet values are typically available for room temperatures (sometimes, for $T = 4\,\mathrm{K}$), while our experimental setups are operated around 50 mK. In order to mitigate this problem of estimating losses, we introduce the two-dimensional Planck spectroscopy in Sec. 4.3 which allows us to obtain a more accurate estimation of these losses, and as a result, allows for a more accurate quantum state tomography. If we take the losses provided by datasheets into account, we can fit the data displayed in Fig. 3.3(b) according to Eq. 3.2. Here, we obtain $n = 9.41 \pm 0.21$ and $\kappa = 1.31 \pm 0.03\,(\mathrm{mV})^2$. From this, we can calculate the gain of the amplification chain, $G = 101.2\,\mathrm{dB}$. Lastly, we want to note, that heating the attenuator results in a temperature gradient along the NbTi microwave cable connecting the heatable attenuator with other components in the experimental setup. For our measurements, this is either a directional coupler in the case of the TWPA measurements, or a measurement circulator for the JPA measurements. In previous experiments [5, 110], a linear temperature gradient with a linear distribution of losses along the cable has been assumed and modelled by a distributed beam splitter model with 100 elements. However, in experiments, these losses are not distributed equally along the cable, but are mainly present at the SMA connectors, as the cable itself is superconducting. Therefore, it is more accurate to assign the attenuator temperature to the loss introduced by the first SMA connector and the temperature of the TWPA (or the JPA) to the remaining losses. The correction introduced by this effect is, however, negligible compared to the error bars obtained when fitting the experimental data.

For all of our measurements, it is important to minimize the noise added by the amplification chain. Here, the first amplifier in the chain, the HEMT in our case, has the strongest impact on the overall signal-to-noise ratio [103]. Therefore, we need to ensure that the HEMT amplifiers are adding only a minimal amount of noise photons, regardless of their age and the number of cooldowns they have experienced. To this end, we consider the noise performance of the HEMT amplifiers over an extended period of time and evaluate the PNCF measurements performed in the Alice lab over the last

7 years. Figure A.1 shows the extracted noise photons n for four of the HEMT amplifiers installed in the cryostat. Here, we do not observe a consistent increase in noise photons for any of the amplifiers. However, the added noise photons change drastically whenever the experimental setup is changed. This suggests that the noise added by the system may have a strong influence on the number of noise photons extracted with the PNCF method.

3.2.4 Reference state reconstruction

Due to low energy of single photons at microwave frequencies, the reconstruction of microwave quantum signals is a challenging task, as they are strongly affected by thermal excitations at room temperatures. One possibility for detecting these quantum microwave states is to utilize linear amplifiers to amplify these weak quantum signals and then detect them at room temperatures. However, even the best semiconductor-based HEMT amplifiers add around 10 noise photons to an input quantum signal. Therefore, we have to make use of advanced reconstruction techniques in order to reconstruct microwave quantum signals with low photon numbers. To this end, we utilize the reference state reconstruction method where we use a well-known signal as a reference state. This allows us to eliminate noise contributions in the amplification chain [111]. In our experiments, this reference state is provided by a weak thermal state. This results in photon numbers $\ll 1$ which allows us to treat this weak thermal state as vacuum state in most of our experiments. In general, we can define the complex envelope function

$$\hat{S}_{1,2} = \sqrt{G_{1,2}}(\hat{a}_{1,2} + \hat{V}_{1,2}) \tag{3.3}$$

for the detected signal at room temperature. Here, $G_{1,2}$ represents the gain of each of the amplification chains (assuming we have two of these) and $\hat{V}_{1,2}$ is the added noise of the respective path. This complex envelope function can be calculated from the measured quadratures $\hat{I}_{1,2}$ and $\hat{Q}_{1,2}$ by using the photon number conversion factor via

$$\hat{S}_{1,2} = \frac{\hat{I}_{1,2} + i\hat{Q}_{1,2}}{\sqrt{\kappa}} \quad . \tag{3.4}$$

The complex envelope function for the weak thermal reference state $\hat{v}$ is given as

$$\hat{S}_{\mathrm{ref};1,2} = \sqrt{G_{1,2}}(\hat{v}_{1,2} + \hat{V}_{1,2}) \quad . \tag{3.5}$$

Utilizing the fact, that the moments of the reference state are known, Eq. 3.5 allows us to calculate the noise moments $\langle(\hat{V}_1^\dagger)^n(\hat{V}_2^\dagger)^m\hat{V}_1^k\hat{V}_2^l\rangle$, with $n+m+k+l \leq 4$ for $n,m,k,l \in \mathcal{N}$. We can use this knowledge over the noise moments to determine the quadrature moments $\langle I_1^k Q_1^l I_2^m Q_2^n\rangle$ from the detected moments of the complex envelope function. A more detailed description of the reference state reconstruction method can be found in Ref. 110. It is important to note, that the reference state cannot be approximated by the vacuum state in all of our experiments. In Sec. 5.2.2, we show measurements, where the temperature of the input attenuator, creating the reference state, increases up to 120 mK. In this case, the thermal statistics in the reference state can no longer be neglected and the moments of the thermal state need to be considered. [6, 7, 112–139]

Chapter 4

Characterization of Josephson parametric devices

In this chapter, we apply the theoretical and experimental knowledge introduced in the previous chapters for the characterization of two different classes of parametric amplifiers, namely, narrow-band JPAs and broadband TWPAs. With the two-dimensional (2D) Planck spectroscopy we introduce a method to determine losses *in-situ* in a closed cryogenic system. Characterization of the JPA starts with investigations of flux dependency of its respective resonance frequency, followed by the nondegenerate gain measurements. Furthermore, we characterize the 1 dB-compression point. Afterwards, we determine the degenerate gain and the squeezing properties. An identical sequence of measurements is performed for the TWPA characterization.

4.1 Characterization of a flux-driven JPA

The JPAs used throughout this thesis belong to the experimental setup employed in the experiment for quantum teleportation of propagating microwaves between two cryostats. Overall, there are five JPAs. JPAs 1-3 employ are single dc-SQUID design, while JPAs 4 and 5 use a double dc-SQUID design. We compare these two respective designs to each other in terms of their frequency ranges, gains, and 1 dB-compression points. Finally, we study the single dc-SQUID JPAs for squeezing generation, and respectively, entanglement distribution in our local microwave quantum network.

Sample preparation

The JPA samples used throughout this thesis have been designed at Walther-Meißner-Institut and fabricated in VTT Technical Research Centre of Finland. They consist of a $\lambda/4$ microwave resonator which is shorted to the ground plane via a dc-SQUID. A microscope image of an exemplary VTT JPA chip is shown in Fig. 4.1. Here, the CPW resonator structure and pump line are visible. They are patterned from a 50 nm thick Nb film sputtered onto a 525 μm thick silicon substrate. The silicon substrate of the

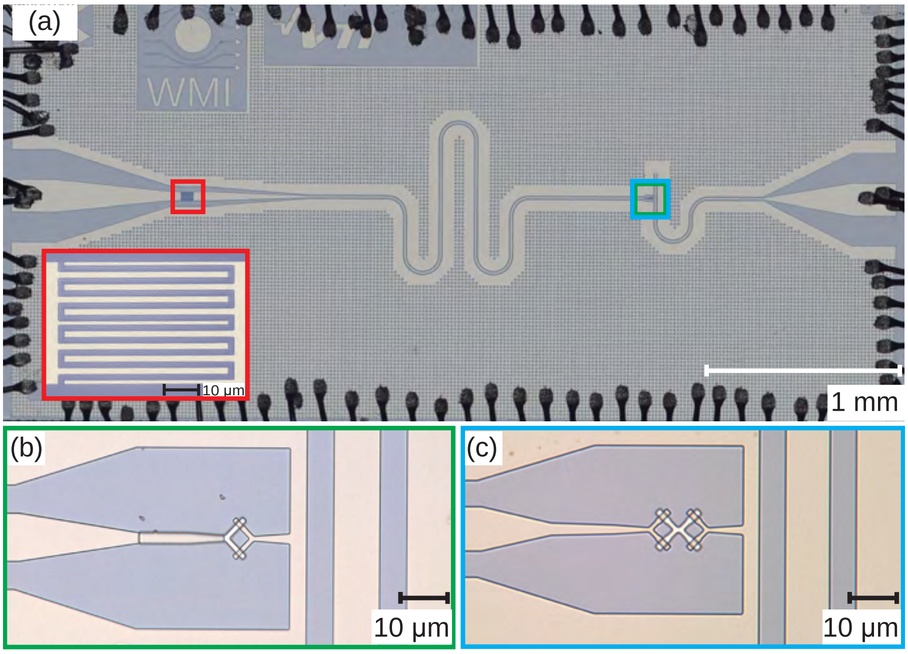

Figure 4.1: (a) Photograph of the JPA sample chip. Black bonding wires are visible along the chip edges. The periodic flux trap structure can be observed over the chip ground plane. The inset (red) shows a zoom-in of the coupling capacitance. The blue square marks the location of the dc-SQUID. Bottom panels (b) and (c) show a zoom-in to the area of the dc-SQUIDs, featuring the single- and double-SQUID designs.

silicon chip is thermally oxidized. The dc-SQUID loop has the area of $4.2 \times 2.4\,\mu\text{m}^2$ and is fabricated from niobium. For our experiments we use single- and double dc-SQUID designs, illustrated in Fig. 4.1(b) and (c), respectively. All of the JPA samples are designed to have an external quality factor $Q_{\text{ext}} \simeq 200$ which is defined by the coupling capacitance value. This coupling capacitor can be seen in the inset of Fig. 4.1(a). The JPA internal quality factors are expected to be much higher than the external ones, thus, putting the JPAs resonators into the overcoupled regime. The JPA samples are glued with GE Varnish glue to the inside of a gold-plated sample box fabricated out of OFHC copper. For microwave connections, we use K-connectors that are soldered into the sample holder. We use a printed circuit board (PCB), made out of gold-plated alumina containing a $50\,\Omega$ CPW transmission line, to connect from the K-connectors to the JPA chip. The signal and pump ports of the JPA chip are bonded to the PCB using the ultrasonic bonding technique with thin aluminium wires (diameter around 100 µm). At the external edges of the PCB, the inner waveguide-conductor is soldered to a glass bead pin linked to the K-connector. To ensure an equal potential across the JPA, the chip, the PCB, and the sample holder are interconnected with a dense mesh of bonds. We test every JPA sample holder and all related microwave cables using time domain reflectometry (TDR)[1]. A picture

[1]We use Tektronix DSA8200 equipped with a 80E08 sampling module.

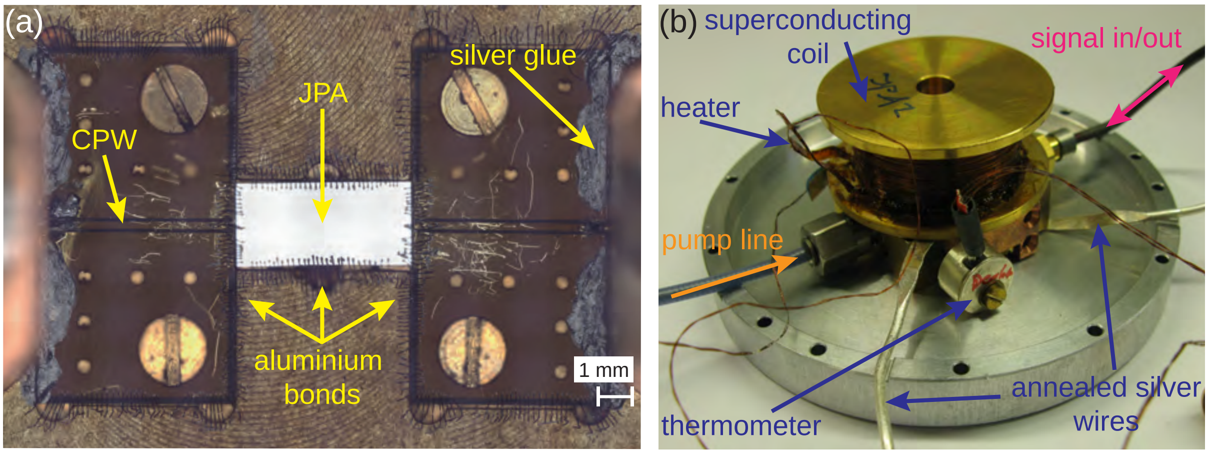

Figure 4.2: (a) Photograph of the JPA chip inside of the sample box. (b) Measurement-ready JPA sample holder mounted to the lid of the superconducting aluminum shield. The annealed silver wires are fixed to the sample rod of the cryostat and ensure good thermalization of all inner components.

of such a sample box containing a JPA chip is shown in Fig. 4.2(a). In order to control the magnetic flux through the dc-SQUID, we employ a large external superconducting coil attached to one side of the JPA sample holder. Furthermore, a $100\,\Omega$ heater and a RuO_2 thermometer are mounted at the opposite sides of the sample holder to enable temperature stabilization of the JPA. A flexible normal-conducting minibend cable and a superconducting NbTi cable are used to connect to the pump and signal port of the JPA, respectively. For magnetic shielding, we place the sample box inside a cylindrical aluminum housing, providing a robust magnetic shielding below the critical temperature of aluminum, $T_c = 1.1\,\mathrm{K}$. A picture of an almost finished sample box is shown in Fig. 4.2(b). In the Alice cryostat, in addition to the superconducting aluminum shield, we use a cylindrical cryperm shield covering large portions of the sample stage to additionally protect the samples during the cooldown (above T_c of aluminum).

Flux dependence of the resonance frequency

As discussed in Sec. 2.2.3, changing magnetic flux Φ_{ext} threading through the dc-SQUID leads to a change of the resonance frequency f_0 of a JPA. In our case, this magnetic flux is created by applying a constant current through the superconducting coil that is mounted on the JPA sample holder, as shown in Fig. 4.2(b). To experimentally verify the flux dependence of the resonance frequency, we employ the setup shown in Fig. 4.3. We measure the JPA resonance in reflection by using an external microwave circulator which separates incident and reflected signals. This approach reduces reflection measurements to the evaluation of a transmitted signal between ports A and B of a vector network analyzer (VNA). The VNA sends a weak coherent microwave signal from port A to the

JPA with a power of $-115\,\mathrm{dBm}$ referred to the JPA input. By comparing the input signal with a measured output signal, a complex S-parameter is obtained. This provides access to estimation of the JPA resonance properties. The resulting plots are shown in Fig. 4.4(a) and (b). Since the VNA measures an unwrapped phase resulting in a linear increase of phase with frequency, we subtract a linear slope from this data. For the magnitude, we subtract a constant background. Since our JPAs are operated in the overcoupled regime, there is only a very weak Lorentz dip in magnitude of the reflection spectrum. Therefore, the JPA resonance frequencies are identified by the characteristic 360° phase shift when crossing the JPA resonance frequency. An experimental flux dependence of JPA 1 resonance frequency is shown in Fig. 4.4(c). The green cross marks a working point at $f_0 = 5.55\,\mathrm{GHz}$ corresponding to the coil current $I_{\mathrm{dc}} = -129.20\,\mu\mathrm{A}$. If not stated differently, this is the working frequency for all JPAs analyzed later in this thesis.

Nondegenerate gain

With the coil current fixed to a constant value corresponding to the desired resonance frequency f_0, we can investigate the JPA amplification properties by applying a pump tone to port P. First, we employ the JPA in the nondegenerate operating mode, as discussed in Sec. 2.2.3. To this end, the pump frequency is set to $2f_0$ while the coherent probe tone generated by the VNA enters the JPA through port S. The probe frequency, $f_{\mathrm{s}} = f_0 + \delta f$, has a non-zero offset from half the pump frequency, $\delta f \neq 0$. The corresponding measurement scheme is shown in Fig. 4.3. Results of the nondegenerate gain measurements for JPA 4 are shown in Fig. 4.5. For small detuning, $\delta f / f_0 \ll 0$, we observe the parametric gain up to 32 dB. The gain as a function of detuning follows a Lorentzian shape. For the measurements shown here, the nondegenerate gain is limited by the dynamic range of the corresponding microwave pump generator. We also consider the gain-bandwidth

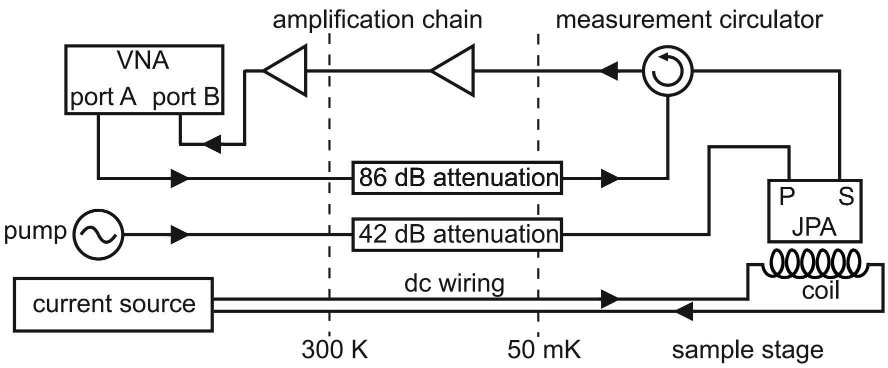

Figure 4.3: Schematic for the characterization of JPAs using a vector network analyzer. The superconducting coil is used to control magnetic flux through the dc-SQUID loop. Labels P and S denote the pump and signal ports of the JPA, respectively.

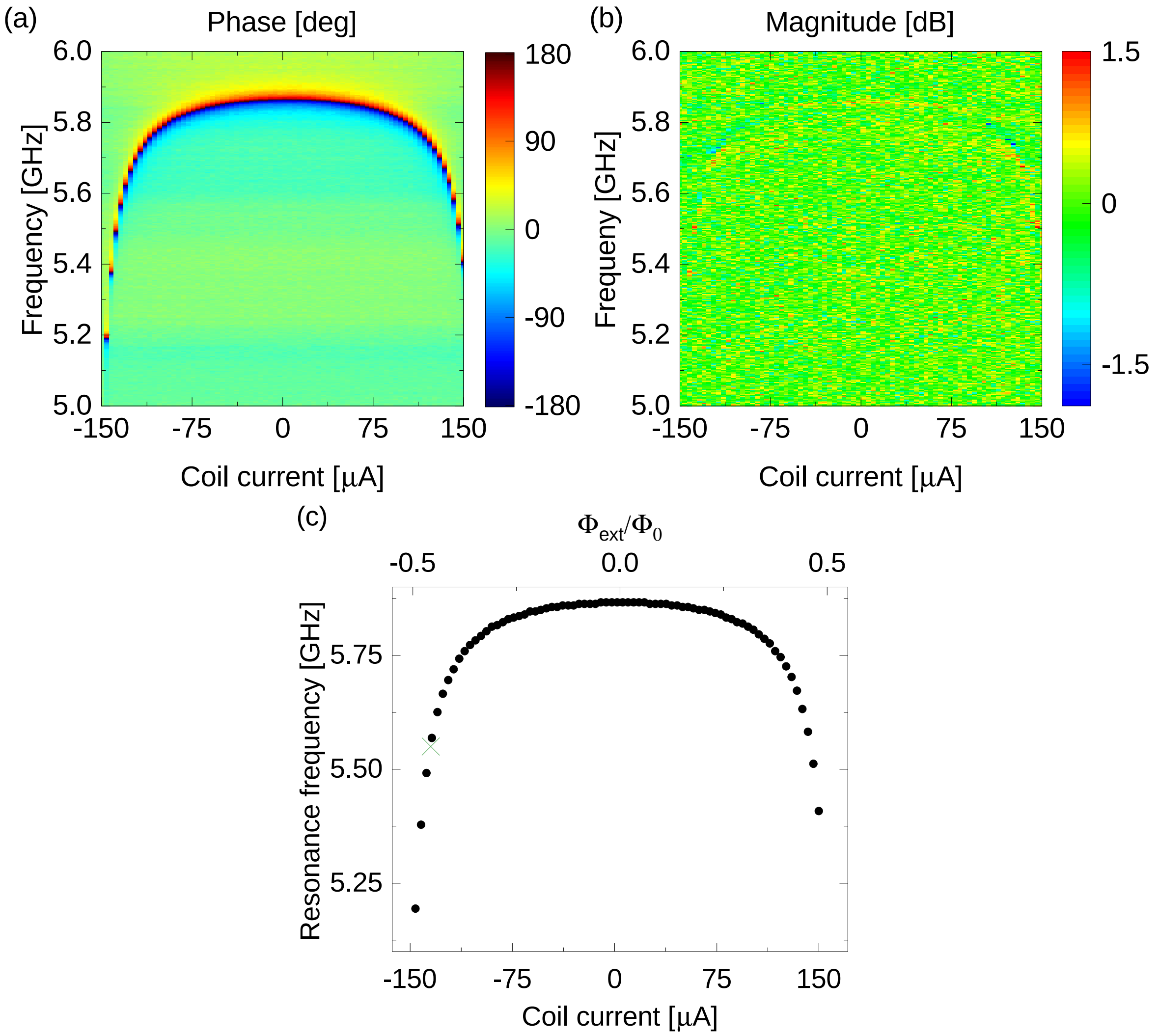

Figure 4.4: Magnetic flux dependence of the JPA microwave reflection. (a) Phase response of the reflected tone. (b) Magnitude response of the reflected tone. (c) Resonant frequency of the single-SQUID JPA as a function of applied magnetic flux. Dots represent the resonant frequencies extracted from the frequency dependence of the reflected signal's phase. The green cross marks the working point at 5.55 GHz used for later measurements.

product (GBP) of our devices which is assumed to be constant for resonator-based JPAs. It is defined as GBP $= \sqrt{G_{\mathbf{lin}}} \cdot B$, where $\sqrt{G_{\mathbf{lin}}}$ is the voltage gain in linear units and B is the full width at half maximum spectral gain bandwidth. The GBP extracted from the data shown in Fig. 4.8 is around 30 MHz. For a JPA featuring a single dc-SQUID, we extract a GBP of around 55 MHz.

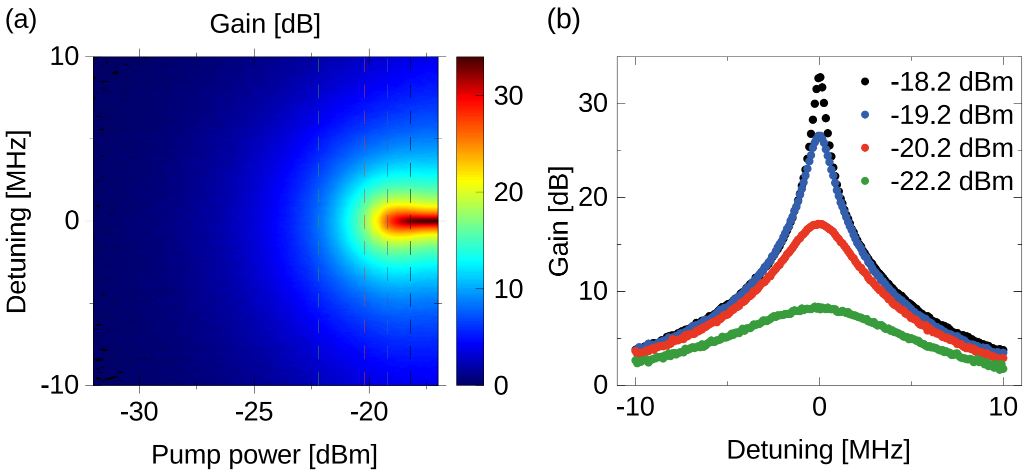

Figure 4.5: (a) Spectrum of the nondegenerate gain as a function of pump power and signal detuning δf from $f_{\mathrm{pump}}/2$ =5.55 GHz for JPA 4. (b) Gain as a function of detuning δf at several pump powers indicated by the colored dashed lines in panel (a). For both panels, the displayed pump powers are referred to the input of the JPA sample box.

1 dB-compression point

The 1 dB-compression point is an important figure of merit for a linear amplifier. It separates the region where the gain of the amplifier is independent of an input signal power and the region where the gain decreases with an increased input power. It is defined as the signal power at which the gain is reduced by 1 dB below its value at low input powers [61]. There are two main mechanisms causing compression effects in JPAs: higher-order nonlinear effects, when interaction of pump and signal tones can shift the JPA resonance frequency, and a pump depletion effect, when the stiff pump approximation becomes invalid [25, 130]. Figure 4.6(a) and (b) shows the signal gain as a function of the input signal power for various pump powers applied to the single- and double-SQUID JPAs. Orange crosses mark the 1 dB-compression points. The pump frequency is set to $2f_0 = 11.1\,\mathrm{GHz}$. A possible explanation for the 'bump' in gain, seen for the two lowest pump powers in Fig. 4.6(a), is the presence of a power-dependent shift of JPA resonance frequency [112]. Here, the JPA working point is optimized for achieving high gain at low input power and large pump powers, where the latter introduces a shift in resonance frequency, as mentioned before. Therefore, the condition $f_{\mathrm{p}} = 2f_0 \approx 2f_{\mathrm{s}}$ is only fulfilled for either large pump or signal powers. For the case, when the pump and signal tone are weak at the same time, the power-dependent shift of JPA resonance frequency is weak. Thus, the resonance frequency is detuned from twice the pump frequency, $f_{\mathrm{p}} \neq 2f_0$, and JPA gain is reduced. An increase in signal power reintroduces the power-dependent shift and realigns the JPA resonance frequency to $f_{\mathrm{p}} = 2f_0$ which leads to an increase in gain. At the signal power close to the 1 dB-compression point, compression effects

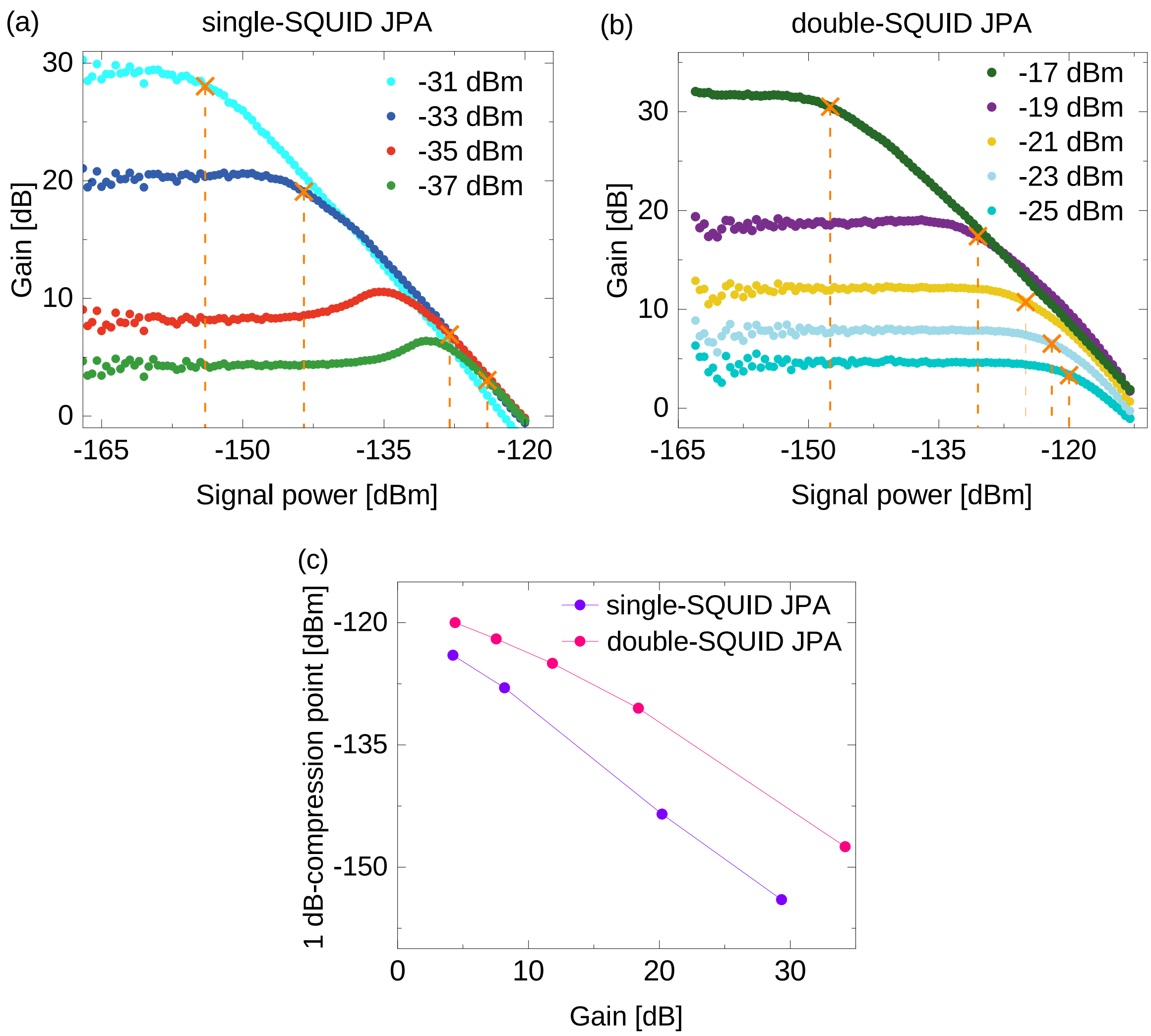

Figure 4.6: JPA nondegenerate gain as a function of input signal power for a (a) single- and (b) double-SQUID JPAs at different pump powers. The input signal and pump powers are referred to the inputs of the corresponding JPA ports. Orange crosses indicate the 1 dB-compression point. (c) 1 dB-compression point as a function of gain for single- and double-SQUID JPAs.

start to take over and reduce the gain. Further information about this mechanism is given in Ref. 74. Figure 4.6(c) shows the 1 dB-compression point as a function of gain for both the single- and double-SQUID JPAs. Here, we can observe that for similar gains, the 1 dB-compression point of the double-SQUID JPA is up to 8 dB larger than for the single-SQUID JPA. This behaviour is expected from theory, as shown in Sec. 2.2.3, where we predict the 1dB-compression point of the double-SQUID JPAs to be larger by 6 dB, as compared to the single-SQUID devices.

Degenerate gain

After determining the JPA properties in the nondegenerate operating mode, we consider the degenerate operating regime. Here, the JPA works as a phase-sensitive amplifier, where one quadrature of the incoming signal is deamplified and the orthogonal one is amplified. In theory, such operation allows for noiseless amplification, as discussed in Sec. 2.2.3. Similar to the nondegenerate operating mode, in the degenerate gain experiments, the pump signal is exactly twice the resonance frequency, $f_\mathrm{p} = 2f_0$. However, the signal frequency is chosen to be exactly half the pump frequency, $f_\mathrm{s} = f_\mathrm{p}/2$. Therefore, the idler mode is centered around the same frequency as the signal mode which leads to interference effects between the idler and signal modes. Therefore, depending on their relative phase, constructive or destructive interference is possible. A scheme of the corresponding measurement setup is shown in Fig. 4.7. We apply a weak coherent signal with the frequency of $f_\mathrm{s} = 5.55\,\mathrm{GHz}$ and power of $P_s = -135\,\mathrm{dBm}$ incident at the signal port of the JPA, while the pump frequency is set to $f_\mathrm{p} = 2f_\mathrm{s}= 11.1\,\mathrm{GHz}$. Before being digitized, the signal from the JPA is further amplified and down-converted to the intermediate frequency of 11 MHz, as discussed in Sec. 3.2.2. We use an FPGA to detect the down-converted signal and demodulate it into the quadrature components, I and Q. Then, the total power, $P_\mathrm{amp} = \langle I\rangle^2 + \langle Q\rangle^2$, of the amplified signal can be calculated. As a reference measurement, we record the power P_ref with no pump tone applied to the JPA. From this, we can measure the phase-dependent degenerate gain, $G_\mathrm{d}(\theta) = P_\mathrm{amp}(\theta)/P_\mathrm{ref}$, by varying the phase θ of the incident signal, as it is illustrated in Fig. 4.8(a). Figure 4.8(b) shows the extracted maximum degenerate gain as a function of pump power. Here, we can obtain a large maximum degenerate gain of up to 40 dB.

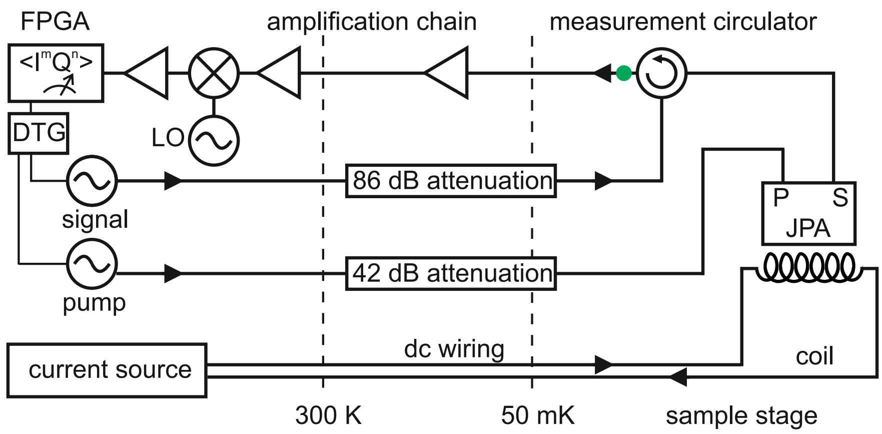

Figure 4.7: Scheme for the degenerate gain and squeezing measurements of JPAs. For the squeezing measurements, the microwave signal source stays inactive. The green dot indicates the reconstruction point of the squeezed state.

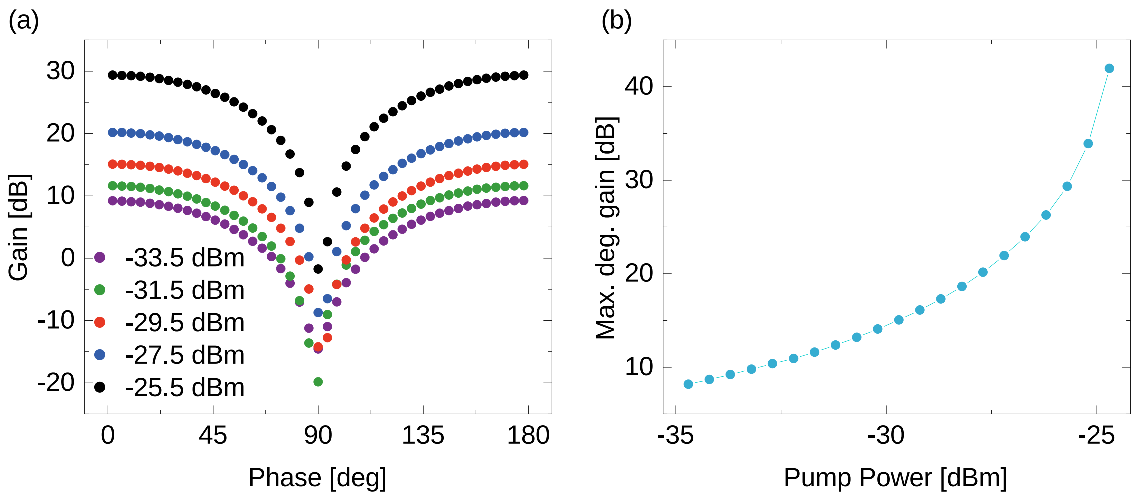

Figure 4.8: (a) Phase-dependent degenerate gain and (b) maximum degenerate gain of JPA 4 at the frequency of 5.55 GHz within the bandwidth of 430 kHz for various pump powers referred to the pump port of the JPA. The curves in panel (a) are artificially shifted across the phase axis, so that the minima coincide.

Vacuum squeezing

Josephson parametric amplifiers are robust and indispensable sources of squeezed microwave states. These states play a fundamental role in many quantum communication protocols, such as the quantum teleportation of microwaves states [6]. For squeezing measurements, we use exactly the same experimental setup and working parameters as in the degenerate gain measurements. However, no coherent input signals are sent to the JPA. Instead, the input signal of the JPA is a weak thermal state, whose photon number population is determined by the temperature of the heatable attenuator installed in the signal microwave line. For typical temperatures of less than 60 mK, such input states can be well approximated by the vacuum state.

Compared to the previous measurements of JPAs gain, we now want to probe the quantum properties of the propagating microwave states created by the JPA. To this end, we need to perform a tomography of the quantum state and gain access the undisturbed signal moments, even in the presence of significant amplifier noise. Thus, to reconstruct the quantum microwave state from the voltages measured by the FPGA, we use the reference state reconstruction method introduced in Sec. 3.2.2. To this end, a two-pulsed scheme is utilized, where the pump is turned off during the first half of the measurement time. This part of the measurement trace serves as the reference signal for state reconstruction. During the second half, a pump tone is applied to the JPA and it squeezes the input signal. The pulsing is achieved by using the pump microwave generator in the external modulation regime, with an external time pulse provided by the DTG. The states are reconstructed at the output of measurement circulator, as indicated by the green dot in Fig. 4.7. The

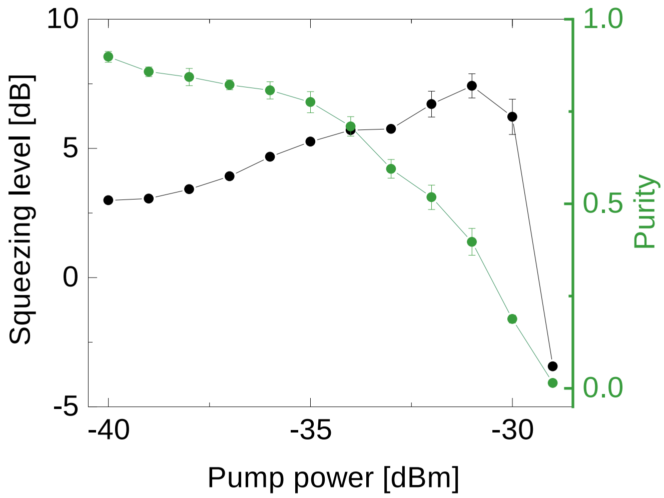

Figure 4.9: Squeezing level and purity as a function of the pump power for JPA 1 at the resonance frequency of 5.55 GHz within the bandwidth of $\Omega = 430\,\mathrm{kHz}$. If not shown, the error bars are smaller than the symbol size. The pump power is referred to the pump port of the JPA sample holder.

squeezing angle is set to $\gamma = 45°$ and stabilized during the measurement procedure. To this end, multiple measurements are taken for each pump power and after each measurement the squeezing angle is reconstructed. Based on this result, the phase of the pump signal adjusted accordingly. We observe that the squeezing level S increases with increasing pump powers, up to $S = 7.4\,\mathrm{dB}$ at $P_\mathrm{p} \simeq -31\,\mathrm{dBm}$, and decreases rapidly after this threshold. Figure 4.9 illustrates this experimental finding, as well as the purity of the squeezed microwave states. For increasing pump powers, the purity decreases monotonically. This decrease of the squeezing level and purity is a result of higher-order nonlinear effects. The latter start to play a role at higher pump powers and lead to a deviation from ideal three-wave mixing process [112, 113]. Previous measurements with this JPA have shown maximum squeezing levels of up to 10 dB with corresponding purities of larger than 0.8. However, these measurements were taken at the working point of $f_0 = 5.742\,\mathrm{GHZ}$. It can be seen from Fig. 4.4 that the working point of 5.55 GHz corresponds to a much steeper slope of the $f_0(\Phi_\mathrm{ext})$ dependence. This makes this working point more sensitive to flux noise and results in excessive noise during the squeezing operation. Nevertheless, this working point is optimal in the scope of measuring entanglement distribution and quantum teleportation between two cryostats. Here, we need to find a common working point, where both frequencies of the single- and double-SQUID JPAs would be identical and, at the same time, the double-SQUID JPAs would have sufficient gains, as required to fulfill a projection criterion in the quantum teleportation protocol. This results in operating both JPA designs at their, individually, non-ideal working points.

4.2 Characterization of the TWPA

In the following section, we discuss TWPA sample preparation, as well as characterization of its parametric gain properties. To this end, we will perform the same sets of measurements as for the JPA and compare their results.

Sample preparation

The TWPA sample used in this thesis is designed and fabricated in VTT as a part of collaboration within the Quantum Microwave Communication & Sensing (QMiCS) project, funded within the European Quantum Flagship Initiative. The sample is fabricated using the side-wall passivated spacer (SWAPS) niobium junction technology which relies on the UV photolithography [114, 131]. The Josephson junctions making up the SNAILs are formed by a Nb/Al-AlO_x/Nb trilayer. A schematic drawing of the TWPA layout is depicted in Fig. 4.10. Capacitors, made from open-ended transmission-line spiral resonators, are galvanically coupled to the Nb CPW center conductor and to the CPW ground plane. A secondary niobium wiring layer is used for the on-chip magnetic flux bias line. This flux line has a meander shape and periodically crosses from one side of the CPW to another, which ensures an equal potential of the ground planes on both sides of the transmission line. This is important to prevent a leakage of static currents and a formation of parasitic loops of quantized magnetic flux. A detailed description of the fabrication process can be found in Ref. 56.

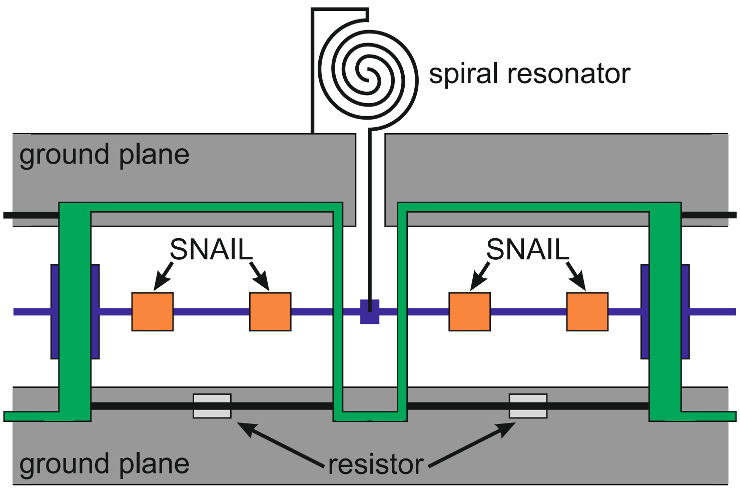

Figure 4.10: Schematic drawing of the TWPA layout on the chip, as described in Ref. 56. The blue line indicates the center conductor of the CPW and the flux line is depicted in green. At their crossings, a parallel-plate capacitor is formed with the center conductor acting as the bottom-electrode and the flux line acting as the top-electrode, separated by an aluminum oxide layer. Resistors connect the flux line to the ground plane.

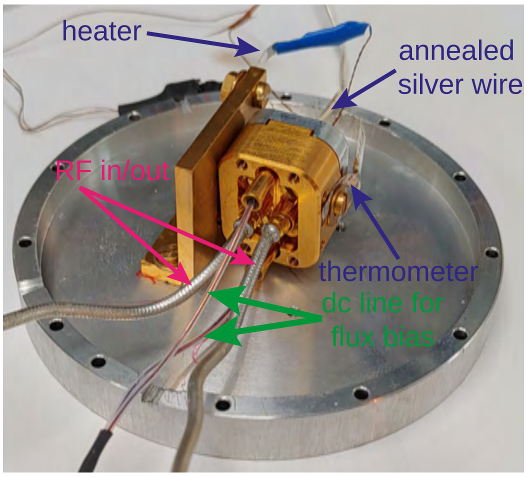

Figure 4.11: Photograph of the TWPA sample holder mounted to the open superconducting aluminum shield. The sample holder itself consists of a copper base for good thermalization and an aluminium lid for increased magnetic shielding.

The TWPA sample is housed in a non-magnetic copper sample holder within an aluminum magnetic shielding box. The sample holder has two SMP connectors with flexible co-centric tin-plated copper cables connected to them. These cables are used to route the combined pump and signal tones to the TWPA and an amplified output tone away from the TWPA. For the on-chip flux biasing the sample holder is equipped with two MMCX female ports. Superconducting NbTi wires are reinforced with temperature resistant Teflon based jackets and carry the bias current to the sample holder. Similar to the JPA sample holders, we install a $100\,\Omega$ heater and a thermometer on the opposite sides of the TWPA sample holder to enable temperature stabilization of the latter. For thermalization, we clamp an annealed silver wire between the sample box and OFHC copper bracket which is used to attach the TWPA sample holder to the aluminum shielding box. The other end of the silver wire is connected to the mixing chamber stage of the cryostat. A photograph of the prepared TWPA sample holder can be found in Fig. 4.11.

Flux response of the TWPA

We start characterizing the TWPA by probing the flux response of the undriven TWPA with a VNA. A scheme of the measurement setup can be found in Fig. 4.12. Overall, this setup is quite similar to the one used for the VNA measurements conducted with the JPAs, but there are also a few differences. First, we directly measure the transmission through the TWPA, without additional input circulators. Second, the TWPA has no dedicated pump port and, therefore, the pump and signal tones enter via the same port. This makes it necessary to combine the two signals beforehand. We accomplish this by using a cryogenic directional coupler[2] just before the TWPA. The pump signal is fed

[2]We use a CPL4000-8000-20-C, Miteq, directional coupler.

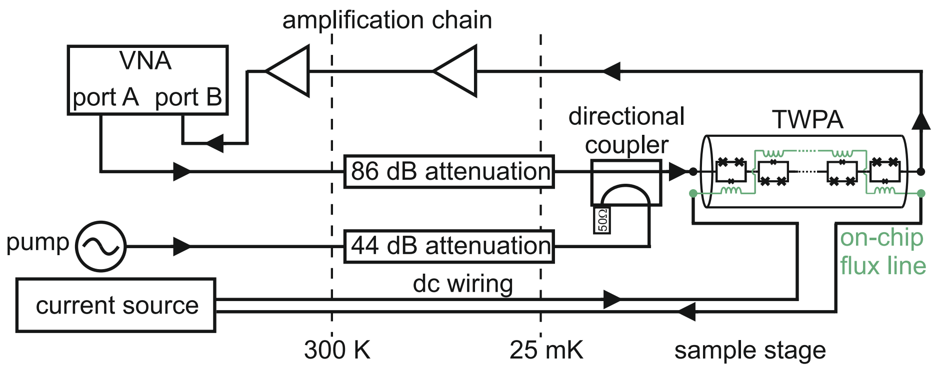

Figure 4.12: Schematic for the characterization of the TWPA using a vector network analyzer. An on-chip bias line is used to control magnetic flux through the SNAIL metamaterial.

to the "coupled" port of the directional coupler which is weakly ($\simeq -30\,\mathrm{dB}$) coupled to the output. For flux biasing of all of the 1632 SNAILs in the current TWPA, an on-chip magnetic flux bias line is utilized. It ensures homogeneous biasing and negligible off-chip fringing magnetic fields. We first perform a reference VNA measurement at zero bias current in order to obtain the reference scattering parameter $S_{\mathrm{BA}}^{\mathrm{ref}}(f_{\mathrm{s}}, I_{\mathrm{dc}} = 0)$. We later subtract this frequency-dependent background from the measured scattering parameter $S_{\mathrm{BA}}(f_{\mathrm{s}}, I_{\mathrm{dc}})$, in order to obtain the flux response of the undriven TWPA, $S_{\mathrm{BA}}^{\mathrm{TWPA}}(f_{\mathrm{s}}, I_{\mathrm{dc}}) = S_{\mathrm{BA}}(f_{\mathrm{s}}, I_{\mathrm{dc}}) - S_{\mathrm{BA}}^{\mathrm{ref}}(f_{\mathrm{s}}, I_{\mathrm{dc}} = 0)$. Figure 4.13 shows the magnitude and phase of the transmitted signal as a function of applied current (generating the magnetic flux through the SNAILs) with the background subtracted. Here, the magnitude of the signal, $\left|S_{\mathrm{BA}}^{\mathrm{TWPA}}(f_{\mathrm{s}}, I_{\mathrm{dc}})\right|$, changes only very weakly as a function of I_{dc}. Ripples in the transmitted signal magnitude, as a function of signal frequency, appear due to a non-ideal impedance matching of the Josephson metamaterial to the external $50\,\Omega$ impedance. As the TWPA is designed to avoid any resonant elements in the range of 4-8 GHz, no characteristic 360° jump is visible in the phase of the transmitted signal, $\arg\left(S_{\mathrm{AB}}(f_{\mathrm{s}}, I_{\mathrm{dc}})\right)$, and the phase changes smoothly as a function of magnetic flux. Figure 4.13(c) shows the group delay $\tau = \partial\theta/\partial(2\pi f)$ introduced by the TWPA, where θ is the phase of the signal and f is its frequency. The Φ_0-periodic flux response of the SNAIL array allows us to relate the dc-bias current I_{dc} to the magnetic flux through the SNAILs, $\Phi_{\mathrm{ext}}/\Phi_0 = 0.578\,\mathrm{I_{dc}/mA} - 0.016$. This corresponds to the mutual inductance between the SNAIL array and the flux line of $0.578\,\Phi_0/\mathrm{mA}$ and matches the value provided by the manufacturer VTT. The phase response of the TWPA, and therefore also the group delay, is shifted by roughly 850 uA, or half of the flux quantum, as compared to the behaviour predicted by theory. Here, we expect a local minimum of the group delay to coincide with zero flux bias.

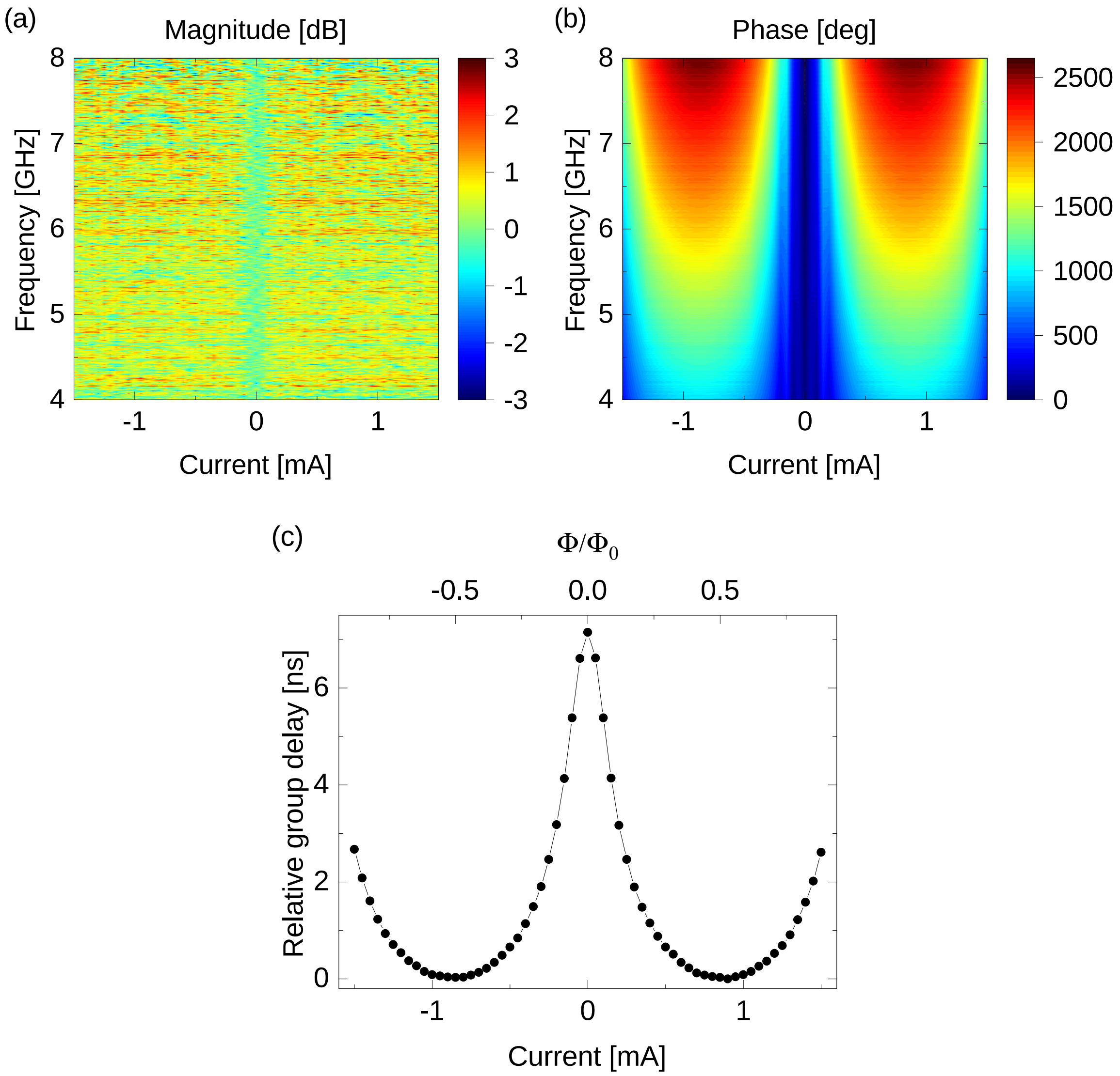

Figure 4.13: Transmission spectrum of the undriven TWPA as a function of the bias current. Panels (a) and (b) show the magnitude and phase response of the transmitted signal. (c) Group delay of the transmitted signal. The group delay is shifted across the vertical axis in such a way that the minima coincides with 0 ns delay.

Nondegenerate gain

Due to the broadband and non-resonant nature of the TWPA, finding a proper working point is more cumbersome, as compared to the resonator-based JPAs. Namely, we can vary pump power, pump frequency and the current for flux biasing over a wide parameter space. In order to achieve an optimal working point, we start by sweeping the flux bias and the pump microwave power while keeping the pump frequency fixed to 12 GHz. The result of such a measurement is shown in Fig. 4.14(a). Here, each data point corresponds

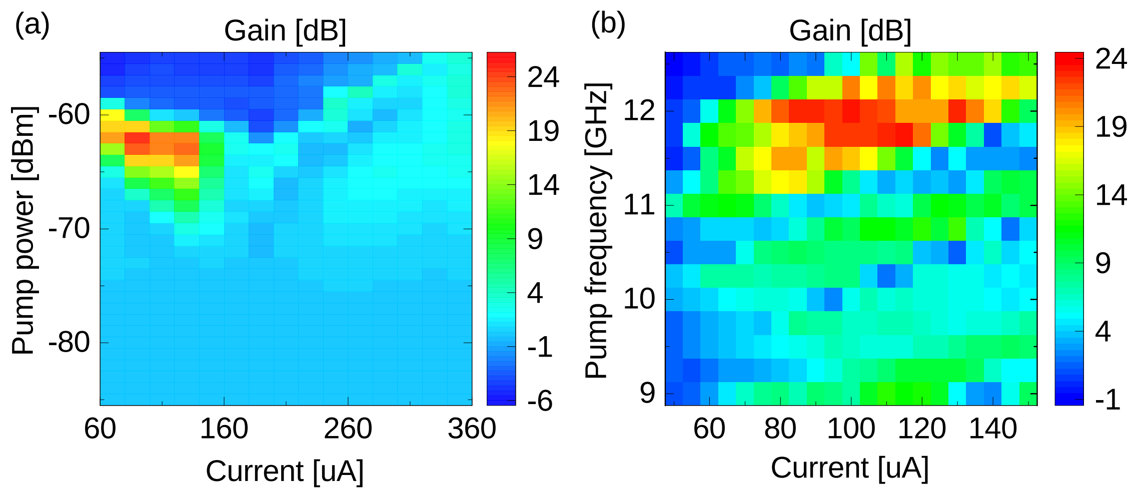

Figure 4.14: Mean signal gain of the TWPA. Each data point reflects the average gain over the frequency range of $f_s = 4\,\mathrm{GHz}$ to $f_s = 8\,\mathrm{GHz}$. For panel (a), the pump frequency is fixed at 12 GHz while we vary the dc bias current and the pump power. For panel (b), the pump power is fixed to $-63\,\mathrm{dBm}$ while we vary the dc bias current and the pump frequency. The values given for the pump power are referred to the input of the TWPA sample box.

to an average TWPA gain over the signal frequency range of 4 GHz to 8 GHz. We find a significant signal gain only around $\Phi_{\mathrm{ext}} \approx 0.1\,\Phi_0$, with the highest gain corresponding to the bias current of $I_{\mathrm{dc}} = 100\,\mathrm{uA}$ and the pump power of $-63\,\mathrm{dBm}$ referred to the TWPA input. Here, we observe the same behaviour as for the measurement of the group delay: the flux bias corresponding to the highest signal gain does not agree with the working point predicted by theory, $\Phi_{\mathrm{ext}} \approx 0.4\,\Phi_0$, where the condition for phase matching condition with a non-vanishing 3WM term is satisfied. In order to further refine the working point, we fix the pump power to the optimal value obtained from the previous measurement ($-63\,\mathrm{dBm}$) and sweep the pump frequency, f_{p}, and the bias current. The results of this subsequent measurement can be seen in Fig. 4.14(b). Here, we obtain the highest average gain of 24 dB at the bias current of $I_{\mathrm{dc}} = 95\,\mathrm{uA}$ and the pump frequency of 12 GHz. To make sure that this working point is not biased by the chosen starting point, we repeat the procedure starting from a pump frequency of 10 GHz, which, however, leads to the same working point as before. Figure 4.15 shows the gain at the determined working point as a function of the signal frequency and pump power. We see a maximum gain of 25 dB over the range from 4 GHz to 8 GHz and gain ripples on the order of 4 dB. Further increase in the pump power leads to a decrease of ripples amplitude, although the gain is also reduced. We note that data outside of the frequency span of 4 GHz to 8 GHz has not been considered here, since it exceeds the specified operating range of the HEMT amplifier, used after the TWPA. We repeat this measurement at the dc bias current with opposite sign, $I_{\mathrm{dc}} = -95\,\mathrm{uA}$. Here, we observe nearly identical signal gain as

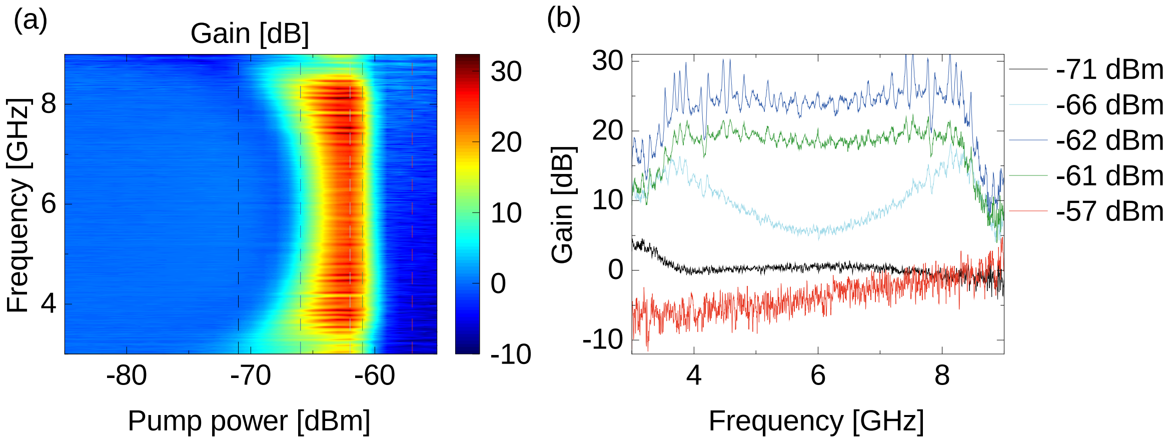

Figure 4.15: (a) Gain of the TWPA as a function of the pump power and signal frequency. Here, the bias current and pump frequency are set to $I_{\mathrm{dc}} = 95\,\mathrm{uA}$ and 12 GHz, respectively. (b) Selected cross sections at various pump powers, also indicated by the colored dashed lines in panel (a).

compared to the measurement at $I_{\mathrm{dc}} = 95\,\mathrm{uA}$. We expect this symmetric behaviour of the TWPA gain based on our theoretical analysis of the SNAIL potential coefficients, where we found $|c_3(-\Phi_{\mathrm{ext}})| = |c_3(\Phi_{\mathrm{ext}})|$ and $c_4(-\Phi_{\mathrm{ext}}) = c_4(\Phi_{\mathrm{ext}})$. We also want to discuss the gain-bandwidth product of the TWPA. While a generic TWPA does not have the fixed GBP intrinsic to resonant JPAs, it is still instructive to calculate it. Assuming the TWPA gain $G = 25\,\mathrm{dB}$, we obtain GBP $= \sqrt{G_{\mathrm{lin}}} \cdot 4.13\,\mathrm{GHz} = 73.44\,\mathrm{GHz}$. This values exceeds the JPA GBP values by more than 3 orders of magnitude. Lastly, we want to emphasize the importance of filtering the dc-current used for flux-biasing of the SNAILs. When we bypass the low-pass filter mentioned in Sec. 3.1, we obtain the same flux response for the undriven TWPA as presented in Fig. 4.13. However, there is no working point leading to significant nondegenerate TWPA gain in this configuration.

1 dB-compression point

As for JPAs, determination of 1 dB-compression point is an important part of the TWPA characterization. Figure 4.16(a) shows related measurements for various pump powers and the fixed signal frequency of 6 GHz. Here, we see a 1 dB-compression point that is rather independent of the signal gain, especially when we compare this to the behaviour of the JPAs (Fig. 4.6(c)). At the TWPA gain of 25 dB, we obtain the frequency-averaged (over the signal frequency of 4-8 GHz) 1 dB-compression point of $-99.4\,\mathrm{dBm}$. While this value is roughly 35 dB larger than the one of the double-SQUID JPA and shows improvement over the best performing high dynamic range JPAs [115, 116], it is still considerably inferior in comparison to commercially available semiconductor-based HEMT amplifiers. A particular source for this limitation is the pump depletion effect, similar as for the JPA. Another limiting factor is power leakage of the pump tone to higher harmonics, especially

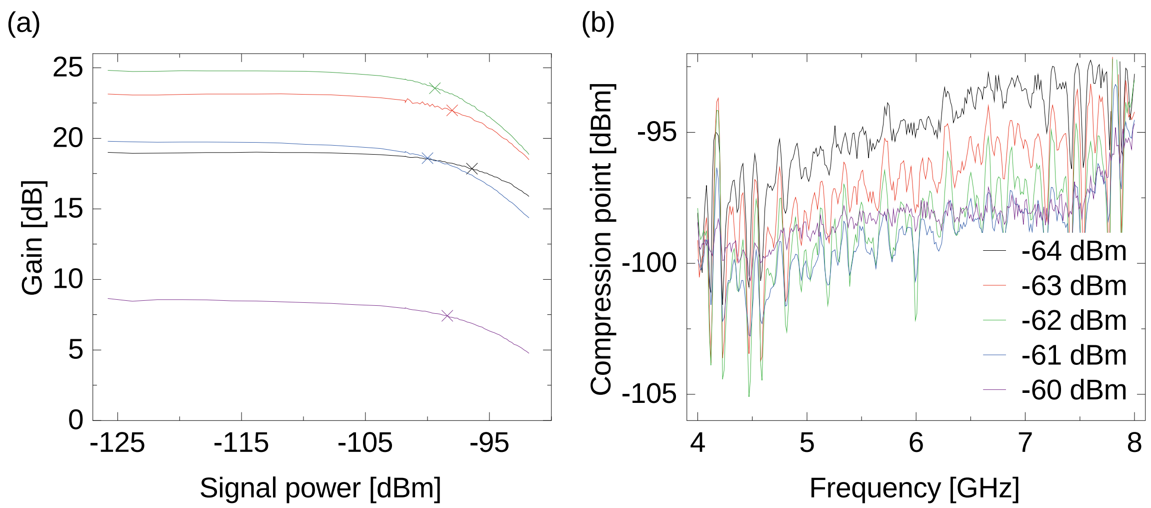

Figure 4.16: (a) Signal gain as a function of the input signal power at different pump powers. All powers are referred to the input of the TWPA sample holder. Crosses indicate the 1 dB-compression point. Here, the signal frequency is set at 5 GHz, while the pump frequency is at 12 GHz. (b) 1 dB-compression point as a function of the signal frequency and the pump frequency set at 12 GHz. Panels (a) and (b) use the same color code for the different pump powers.

to the second harmonic at $2f_\mathrm{p}$ [89]. Lastly, the Kerr phase modulation and higher-order processes can also limit the 1 dB-compression powers [98, 118]. The 1 dB-compression point as a function of the signal frequency can be found in Fig. 4.16(b), where we see an increase of the 1 dB-compression point when we move to higher signal frequencies. Respective compression ripples are, most likely, a result of the gain ripples.

Degenerate gain

Similar to JPAs, TWPAs can also be operated in the degenerate amplification regime. In order to do so, we have to set the frequency of the pump tone to exactly twice the signal frequency, $f_\mathrm{p} = 2f_\mathrm{s}$. In our experiment, we probe the TWPA at the signal frequency of $f_\mathrm{s} = 6\,\mathrm{GHz}$ and with the signal power of $P_\mathrm{s} = -126\,\mathrm{dBm}$. Accordingly, the pump frequency is set at the frequency of 12 GHz and the power is varied from $-80\,\mathrm{dBm}$ to $-64\,\mathrm{dBm}$, referred to the input of the TWPA sample box. Similar to the degenerate gain measurements of the JPAs, we use the FPGA to obtain the quadratures, I and Q, of the signal amplified by the TWPA. A corresponding measurement scheme is shown in Fig. 4.17. Compared to the Alice lab, we use an AWG for pulse modulation of the microwave pump source and the signal leaving the cryostat is down-converted to a different intermediate frequency of 12.5 MHz. We sweep the signal tone phase from 0° to 360° in order to obtain the phase-dependent gain of the TWPA. The gain of the TWPA is calibrated against the measurement when the pump is turned off, as discussed for the

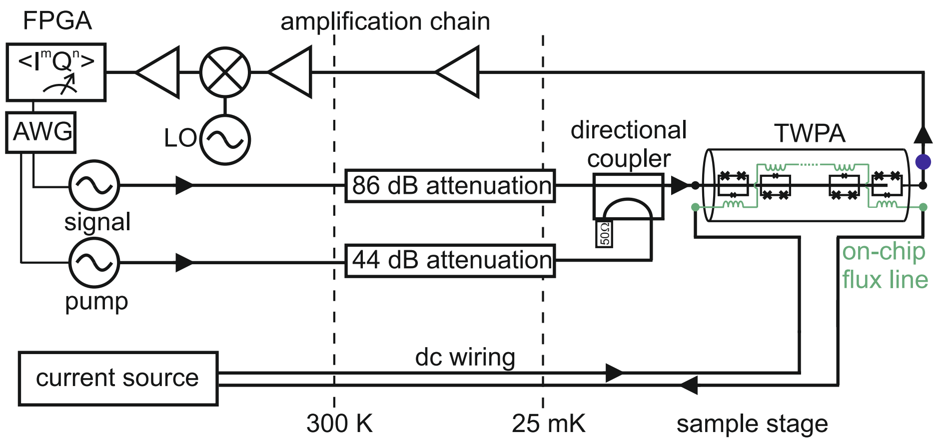

Figure 4.17: Schematic of the degenerate gain and squeezing measurements of the TWPA. For the squeezing measurements, the microwave signal source is inactive. The blue dot after the TWPA indicates the reconstruction point of the squeezed state.

measurements of the JPA degenerate gain. Figure 4.18(a) shows the degenerate gain as a function of the signal phase for various pump powers and Fig. 4.18(b) shows the extracted maximum gain. This measurement shows two distinct pump power regions: for the pump powers smaller than −68 dBm, the phase dependence is sine-like and deamplification of the signal is visible; for the pump power above −68 dBm, we see a rapid increase in the maximum gain and the phase dependence becomes unbalanced, i.e., $G_{\mathrm{amp}} \neq G_{\mathrm{deamp}}$. For pump powers larger than −66 dBm, we observe no deamplification of the signal. This non-existent deamplification may be explained by excessive noise added by the TWPA

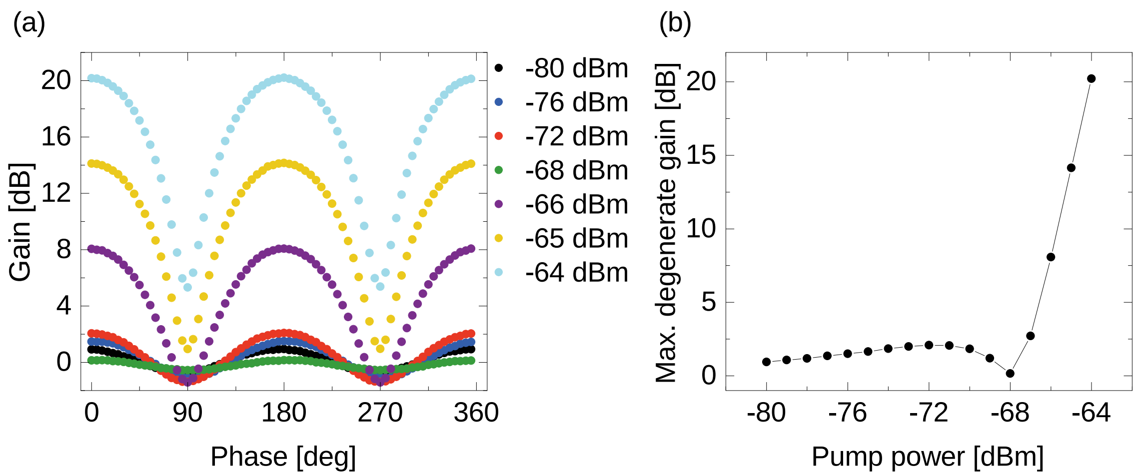

Figure 4.18: (a) Phase-dependent degenerate gain and (b) maximum phase-dependent gain of the TWPA at the central frequency of 6 GHz within the bandwidth of 400 kHz for various pump powers referred to the TWPA input. The curves in panel (a) are shifted along the horizontal axis in order for their minima to coincide.

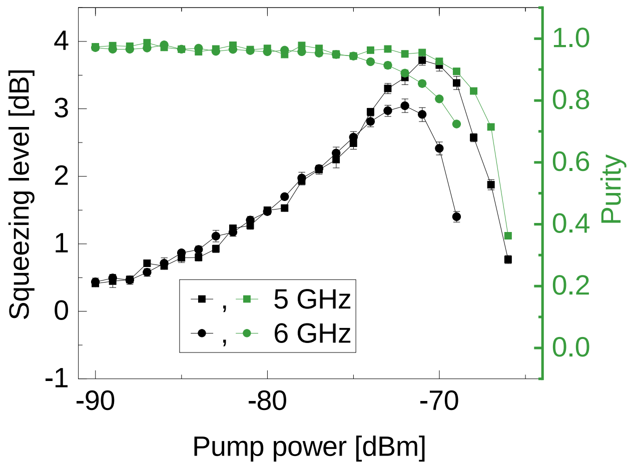

Figure 4.19: Squeezing level and purity as a function of the pump power for carrier frequencies of 5 GHz (squares) and 6 GHz (circles), with the detection bandwidth of 400 kHz. The pump frequency is set to twice the carrier frequency $f_\mathrm{p} = 2f_\mathrm{s}$. If not shown, the error bars are smaller than the symbol size. The pump power is referred to the TWPA input.

during the parametric amplification. Overall, the behaviour of the maximum gain has also been observed in previous experiments, however, its physical origin is not entirely clear and further investigation is needed. Last, we want to consider the phase-sensitive extinction ratio (PSER), defined as the difference between the maximum phase-sensitive amplification and deamplification at a fixed pump power, PSER $= G_\mathrm{amp} - G_\mathrm{deamp}$. For pump powers larger than -66 dBm, it is 14 dB. As compared to the JPA measurements shown in Fig. 4.8(a), where PSER $= 35$ dB, and TWPAs featuring phase-matching resonators, where PSER $= 56$ dB [93], this value is rather low for the current TWPA.

Vacuum squeezing

Lastly, we characterize vacuum squeezing with the SNAIL based TWPA. To achieve this, we employ a setup similar to the one shown in Fig. 4.17. We assume that in the absence of any coherent input, the TWPA incident state is well-approximated by the vacuum state at the corresponding signal frequency generated by the 30 dB attenuator placed in the input signal line. Reconstruction of the quantum microwave state produced by the TWPA is done in the same way as for the JPA, i.e. by utilizing the reference state reconstruction method. The reconstruction point of the quantum state is after the TWPA, as indicated in Fig. 4.17. The results of the TWPA squeezing measurements can be seen in Fig. 4.19, where the squeezing level and purity are obtained for two different carrier frequencies with the corresponding bandwidths of 400 kHz. The squeezing angle is stabilized at $\gamma = 45°$. We observe the maximum vacuum squeezing level of 3.7 dB at 5 GHz and 3.1 dB at 6 GHz with purities above 0.9 in both cases. With further increase in the pump power, vacuum squeezing disappears and purity rapidly decreases. Overall, the squeezing levels achieved by the SNAIL-based TWPA are lower than those obtained with the resonator-based JPAs in this thesis (7.4 dB maximum), or in other TWPA experiments, featuring different TWPA designs, (11.35 dB maximum) [93]. Equation 2.69 illustrates, that the squeezing level at the TWPA output is very sensitive to losses along its transmission line. This suggests that a possible effect limiting squeezing in the current TWPA design is dielectric losses in the Josephson metamaterial, which act as noise channels [97]. Other possible effects degrading squeezing can be attributed to the Kerr-type nonlinearities, generation of higher-order harmonics [112], and an imperfect impedance matching.

4.3 Two-dimensional Planck spectroscopy

Precise knowledge about microwave losses is the requirement for an accurate quantum state tomography and, in particular, for squeezing measurements. However, this is a challenging task in most cryogenic systems because of impossibility to access various parts of the experimental setup during the system operation at millikelvin temperatures. Therefore, one requires to exploit various self-calibrated methods to access these losses *in-situ*. In the following, we discuss some of the methods which are commonly used to achieve this task and study a novel concept of a two-dimensional Planck spectroscopy. Lastly, we present experimental results obtained with this method.

4.3.1 Calibration techniques for cryogenic microwave systems

Many of the *in-situ* calibration methods rely on black-body radiators emitting thermal states with well-known properties defined by the Planck formula. Here, the power spectral density S emitted by an black-body radiator with temperature T follows the Planck equation, as introduced in Sec. 3.2.3. This gives us a precise knowledge over the microwave power emitted into the cable. However, methods relying on the Plank spectroscopy are intrinsically slow, as one needs to wait several minutes for the system to stabilize and thermalize at new temperature points. Therefore, other methods and self-calibrated sources of radiation, such as voltage-bias tunnel junction, have been developed in this context. In the following, we discuss and compare some these calibration techniques.

Heating the mixing chamber

The first calibration technique we want to discuss is based on heating large parts of the experimental setup inside of the cryostat [56]. In experiments, this is usually achieved with a heater and a thermometer placed at the mixing chamber plate, allowing for temperature control of the mixing chamber stage and all of the microwave components thermalized to this stage. Under the assumption that all of these components are at the same temperature

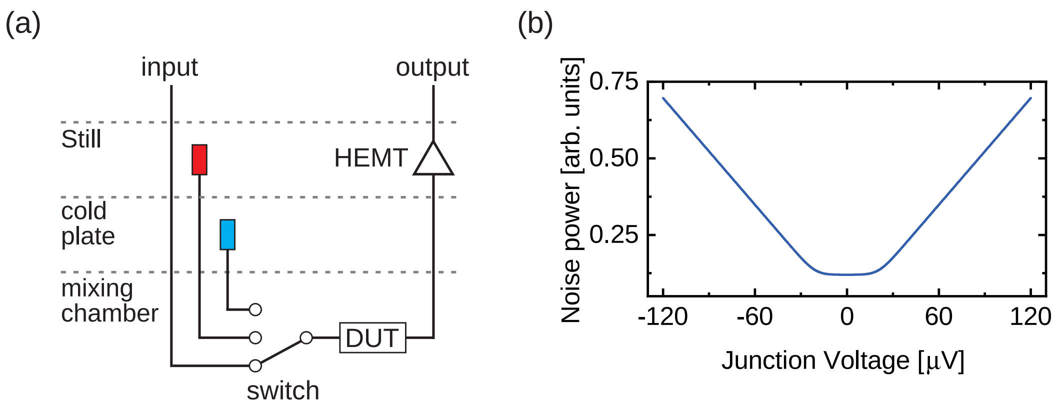

Figure 4.20: (a) Scheme of a calibration setup utilizing ”hot” (red) and ”cold” (blue) $50\,\Omega$ attenuators at different temperature stages of the cryostat. (b) Emitted noise power from a SNTJ as a function of voltage across the junction for the temperature of 50 mK and the frequency of 5 GHz within the bandwidth of $B = 430\,\mathrm{kHz}$ according to Eq. 4.1.

as the mixing chamber stage, we can model them as a single black-body radiator placed at the input of the amplification chain. However, there are several drawbacks to this method. First, the large thermal mass of the mixing chamber stage results in long waiting times until the system reaches the steady state at a new temperature point and makes an accurate stabilization of the stage's temperature demanding. This makes this calibration method quite slow, even compared to other techniques based on black-body radiators. Second, the method prohibits us from placing the first amplifier of the amplification chain on the mixing chamber, as the properties of the amplifier, such as gain and noise performance, can be very depended on its temperature [93]. Overall, while this method is quite easy to implement, its accuracy and use-cases are limited.

Hot and cold sources

One can implement a more elaborate solution by using ”hot” and ”cold” attenuators at two, drastically different, temperature stages and switch between them utilizing a cryogenic microwave switch [75, 132, 133]. A scheme of such calibration setup is shown in Fig. 4.20(a). The accuracy of this method is limited, as we only have two reference temperature points at which we can measure and impedance differences between the hot and cold source signal pathways when operated through a coaxial switch can lead to systematic errors. An advantage of this method is that the mixing chamber temperature stays rather constant regardless of which noise source is chosen. Furthermore, one can utilize the natural temperature stages of the cryostat to eliminate the need for extra heaters and sensors. This results in faster calibration measurements as the system does not need to stabilize and thermalize at new temperature points.

Heatable attenuator

Another step forward is to use a heatable attenuator located in the input line of a to-be-calibrated device or an amplification chain. This approach brings us to the idea of the PNCF calibration [17, 19, 131, 134, 135], as discussed in Sec. 3.2.3 of this thesis. With dilution cryostats reaching temperatures well below 50 mK, this method can resolve the flat part of the temperature-dependent Planck spectrum corresponding to the regime dominated by quantum fluctuations, as it can be seen in Fig. 3.3. In the case when the thermal coupling of the heatable attenuator to the rest of the experimental setup is small enough, a wide range of the attenuator temperatures can be used for calibration without significantly increasing the temperature of other components. This makes this method very accurate.

Shot noise tunnel junction

An alternative method, not based on the black-body radiation, utilizes a voltage-biased tunnel junction generating shot noise [93, 130, 136]. The shot noise tunnel junction (SNTJ) is typically a metal-insulator-metal junction with 50 Ω nominal resistance and is embedded in a 50 Ω coplanar wave-guide transmission line. The metal, usually aluminum, is operated in the normal conducting state by applying a strong magnetic field, generated by an in-situ neodymium magnet. This realizes a normal tunnel junction at dilution temperatures. The noise power P_{N} at frequency f generated by the voltage-biased SNTJ is given by [136]

$$P_{\mathrm{N}} = \frac{k_B B}{2}\left[\left(\frac{eV+hf}{2k_B}\right)\coth\left(\frac{eV+hf}{2k_BT}\right) + \left(\frac{eV-hf}{2k_B}\right)\coth\left(\frac{eV-hf}{2k_BT}\right)\right], \tag{4.1}$$

where V is the voltage bias across the shot noise tunnel junction, B is the measurement bandwidth, and T is the temperature. The noise power P_{N} is plotted as a function of the voltage bias in Fig. 4.20(b). Here, two different regimes emerge: for $eV \ll hf$, the output power is dominated by a constant quantum noise; for $eV \gg hf$, the voltage dependence becomes linear since the noise is dominated by the Poissonian shot noise of electron tunneling events through the tunnel junction. The SNTJ can be switched between different voltage states in under a millisecond [137], allowing for quick noise temperature measurements, limited primarily by the speed of related microwave measurements. Furthermore, the applied voltage can be controlled very precisely and self-heating effects are also small [93, 137]. The disadvantage of this method is that it introduces many extra complexities to experiments. Also, placing a rather strong magnet ($\simeq 0.5$ T [136]) near superconducting and flux-sensitive devices, like JPAs, raises the need for very strong magnetic shielding.

Qubit coupled to a waveguide

The last method we discuss utilizes waveguide quantum electrodynamics and is based on the ac-Stark shift [80, 93]. Here, we use a power dependent transmission of a superconducting qubit coupled in a waveguide when a coherent microwave signal is applied. This method enables the calibration of the absolute power of the incoming coherent signal at the qubit. The transmission amplitude of the waveguide depends on parameters which can be measured independently, such as a spontaneous emission rate of the qubit into the transmission line, Γ_1, a transverse decoherence of the qubit, Γ_2, and the detuning Δ of the coherent probe tone from the qubit frequency. Lastly, the transmission amplitude depends on the power of the coherent probe tone, P_p, as seen by the qubit [138, 139]. This method, arguably, provides a more accurate input loss calibration than the SNTJ, as no additional circuit components are employed, and therefore, no additional, not very well-known, loss sources. The drawback of the ac-Stark method is that it is limited to a relatively narrow frequency range of the used qubit. It also requires somewhat cumbersome, lengthy characterization measurements.

A comparison between the SNTJ and the ac-Stark approaches within the same setup is presented in Ref. 93. Qualitatively, this comparison shows consistent results. However, the shot noise method overestimates the noise temperature for a following amplifier by roughly 2 K as compared to the ac-Stark approach. This difference in noise temperature most likely arises from the losses imposed by the additional components required to operate the SNTJ. When the losses of roughly 1.9 dB introduced by the microwave components located in between the SNTJ and the following amplifier are taken into account, both methods result in the same noise temperature of the aforementioned amplifier.

4.3.2 Path losses and HEMT performance

It is apparent that one of the biggest sources of uncertainty for any of the aforementioned calibration methods comes from the loss estimation between the calibrated photon source and a (HEMT) amplifier. To mitigate this problem, we introduce a method that provides access to yet unknown cryogenic losses in our measurement channel. Here, we combine the heatable attenuator approach with the method relying on heating of the whole sample stage. As for the regular PNCF measurement, introduced in Sec. 3.2.3, we use a 30 dB heatable attenuator emitting black-body radiation as a self-calibrated signal source. For typical experimental setups, we route the microwave signal created by the heatable attenuator through various passive microwave components, like connectors or circulators, before it reaches the amplification chain. These components introduce losses, $L_n > 0$, and attenuate the microwave signal. However, for a complete description, we need to consider them as 4-port devices and describe them using the beam splitter model. Therefore, losses do not only attenuate the incoming microwave signal, but also add a noise contribution. The latter depends on the amount of attenuation introduced and the temperature of the microwave component. In our experiments, all of these microwave components are typically well-thermalized to the mixing chamber plate. Therefore, we can assume that they are all at the mixing chamber temperature T_{mc}. This allows us to consider these losses as one combined attenuator at T_{mc} with a combined loss, $L = \sum_{n=1} L_n$. The power spectral density S_{out} after this combined attenuator is

$$S_{\mathrm{out}}\left(T_{\mathrm{att}}, T_{\mathrm{mc}}, L\right) = S\left(T_{\mathrm{att}}\right) 10^{\frac{-L}{10}} + \left(1 - 10^{\frac{-L}{10}}\right) S\left(T_{\mathrm{mc}}\right) \quad . \tag{4.2}$$

The first part of this equation corresponds to the attenuated black-body radiation from the heatable attenuator at a the temperature T_{att}, while the second part is the added thermal radiation but with a different characteristic temperature, T_{mc}. With the noise n_{HEMT} added by the HEMT during the amplification of the signal and the photon number conversion factor κ, introduced in Sec. 3.2.3, the output power P detected by the FPGA is given by

$$P\left(T_{\mathrm{att}}, T_{\mathrm{mc}}, L, n_{\mathrm{HEMT}}\right) = \frac{\langle I^2 \rangle + \langle Q^2 \rangle}{R} = \frac{\kappa}{R}\left(S_{\mathrm{out}}\left(T_{\mathrm{att}}, T_{\mathrm{mc}}, L\right) + n_{\mathrm{HEMT}}\right) \quad , \tag{4.3}$$

where $R = 50\,\Omega$. A generic scheme for a respective measurement setup is illustrated in Fig. 4.21(a). Now, we can analyze the difference between detected noise powers corresponding to two different temperatures of the mixing chamber, T_1 and T_2

$$\begin{aligned} P_2\left(T_{\mathrm{att}}, T_2, L\right) - P_1\left(T_{\mathrm{att}}, T_1, L\right) &= \frac{\kappa}{R}\left[\left(1 - 10^{\frac{-L}{10}}\right) S\left(T_2\right) - \left(1 - 10^{\frac{-L}{10}}\right) S\left(T_1\right)\right] \\ &\approx \frac{\kappa}{R}\left(1 - 10^{\frac{-L}{10}}\right) \frac{k_{\mathrm{B}} \Delta T}{h f_0} \propto \left(1 - 10^{\frac{-L}{10}}\right) \Delta T \quad . \end{aligned} \tag{4.4}$$

Here, $\Delta T = T_2 - T_1$ is the temperature difference. We also have used the fact that the power spectral density S reduces to the classical Johnson-Nyquist noise spectral density $k_{\mathrm{B}}T$ for $k_{\mathrm{B}}T \gg \hbar\omega$, i.e., for large enough temperatures. In our experiments, this is the case for temperatures that are larger than roughly 150-200 mK. From this we see, that increasing the mixing chamber temperature leads to an increase in the measured output power. Therefore, by performing multiple PNCF measurements at different mixing chamber temperatures, we can obtain access to the unknown component losses via the spacing of the different PNCF curves. Since we have to vary two variables to achieve this result, we call this method a two-dimensional (2D) Planck spectroscopy.

In the experiment, the two temperatures are stabilized using separate external PID control loops. For controlling the mixing chamber temperature, a thermometer and heater, mounted to the mixing chamber plate, are controlled by a Lakeshore Model 372 AC Resistance Bridge. The setup for stabilizing the attenuator temperature is the same, as the one we use for the standard PNCF (Sec. 3.2.3), utilizing a Picowatt AVS-48SI

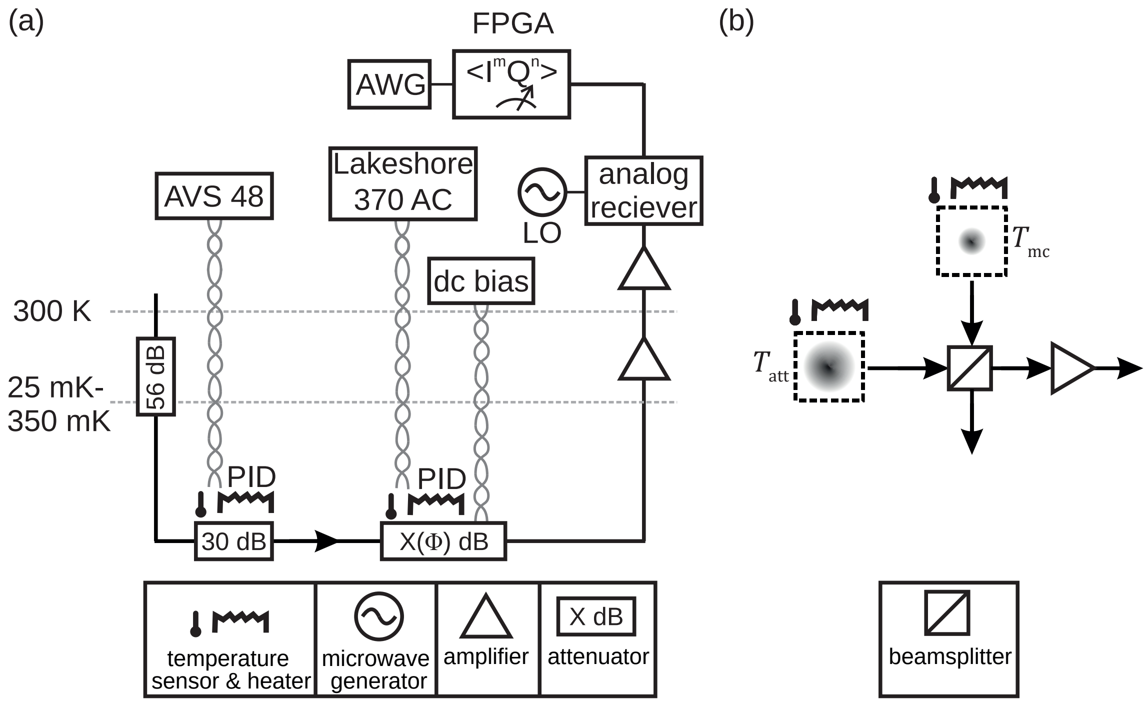

Figure 4.21: (a) Experimental setup used for the 2D PNCF measurements. (b) Schematic drawing of the model used for the 2D PNCF. Noise at the respective mixing chamber temperature T_{mc} enters the channel via an unknown loss port between the heatable attenuator and the HEMT. This loss port is modelled with an asymmetric beam splitter.

Picobridge. The thermometer mounted to the TWPA sample box allows us to verify that not only the mixing chamber plate but also the sample rod are at the desired temperature. Before performing the two-dimensional Planck spectroscopy, we heat only the 30 dB attenuator and observe the temperatures of the mixing chamber in the steady-state. We conclude that the attenuator can only be heated to 600 mK, as long as we want to stabilize the mixing chamber at 100 mK. A further increase in attenuator temperature increases the mixing chamber temperature above 100 mK. For the two-dimensional Planck spectroscopy itself we perform six consecutive PNCF measurements, while we increase the mixing chamber temperature in steps of 50 mK starting at T_{mc} =100 mK. The minimal heatable attenuator temperature is set 20-30 mK higher than the present mixing chamber temperature to ensure good temperature stabilization and its maximum temperature is limited to 600 mK. In Fig. 4.22 we show such a two-dimensional Planck spectroscopy with a corresponding fit of Eq. 4.3. The detection frequency is set to 5.5 GHz and no dc-current is applied to the TWPA. For the detection of the signal leaving the cryostat, the same room temperature setup, as for the regular PNCF measurement, is used. The measured data clearly shows the equidistant spacing between the different mixing chamber temperatures, as expected from Eq. 4.4. For the fit shown, we leave κ, n_{HEMT} and L as

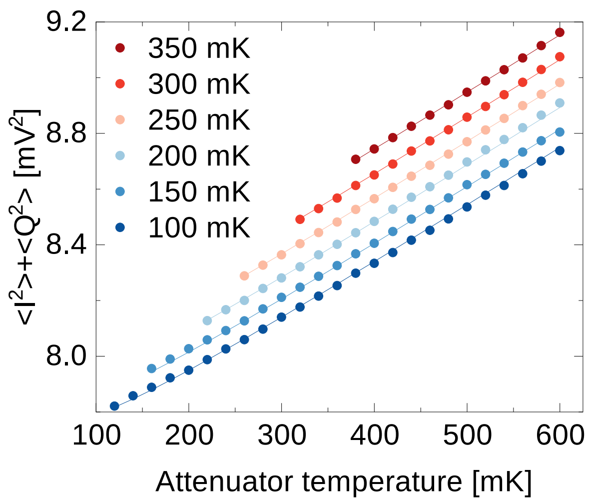

Figure 4.22: Two-dimensional Planck spectroscopy consisting of various attenuator temperature sweeps recorded at different mixing chamber temperatures (indicated by different colors). The TWPA is not driven by a pump tone and the coil current is kept at 0 uA. Symbols depict experimental data and solid lines are corresponding fits. The carrier frequency is $f_0 = 5.5\,\mathrm{GHz}$ with a detection bandwidth of 400 kHz.

free parameters and obtain a very good agreement between the measured and fitted data for $\kappa = 1.15\,(\mathrm{mV})^2$, $n_{\mathrm{HEMT}} = 6.83$ and $L = 2.79\,\mathrm{dB}$. Furthermore, when evaluating the measured data, we take into account the thermal noise, which travels down the pump line and couples to the signal line via the directional coupler. This added signal leads to an increase of the noise temperature of the initial thermal state emitted by the 30 dB heatable attenuator by 8 mK for $T_{\mathrm{mc}} = 100\,\mathrm{mK}$ and up to 12 mK for $T_{\mathrm{mc}} = 350\,\mathrm{mK}$.

As a comparison, we evaluate the data measured at a mixing chamber temperature of 100 mK by using the standard 1D PNCF fitting routine. Here, we assume the losses from the data sheet of the individual components. At a signal frequency of 5.5 GHz, these are: 0.16 dB for the directional coupler, 0.6 dB for the TWPA [56], 0.9 dB for the two non-superconducting microwave cables connecting the TWPA, 0.05 dB for each of the six custom SMA rf-connectors, and 0.09 dB for each of the output circulators. This amounts

Method	Losses L	noise photons n_{HEMT}	PNCF κ
1D PNCF	2.14 dB (data sheet values)	9.59	$1.34\,(\mathrm{mV})^2$
2D PNCF	2.79 dB	6.83	$1.15\,(\mathrm{mV})^2$
Mixing chamber PNCF	-	6.70	$1.10\,(\mathrm{mV})^2$

Table 4.1: Results obtained with the 1D and 2D PNCF measurement and the PNCF measurement only using the mixing chamber heater.

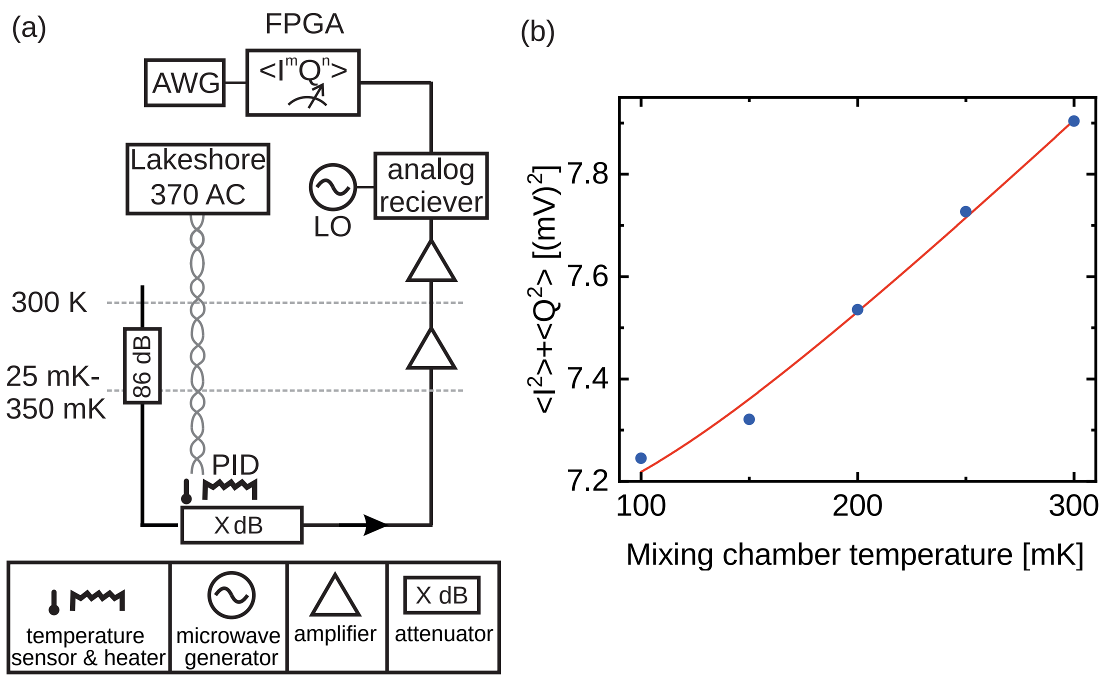

Figure 4.23: PNCF measurement only using the mixing chamber heater. (a) Schematic drawing of the measurement setup. All attenuation placed on the mixing chamber is assumed to be well-thermailzed to the mixing chamber temperature, T_{mc}. (b) Experimental results of the PNCF measurement using the mixing chamber heater. The dots correspond to the experimental data, while the solid line represents the fit according to Eq. 3.2. The carrier frequency is 5.5 GHz and the detection bandwidth is 400 kHz.

to a total theoretical loss of 2.14 dB. The results obtained for the 1D and 2D PNCF measurements can be found in Tab. 4.1. Here we observe, that the path-losses obtained with the two-dimensional Planck spectroscopy are nearly 0.7 dB larger than the value extracted from data sheets.

This underestimation of losses leads to an overestimation of the noise photons added by the HEMT and κ in the case of the 1D PNCF measurement. The number of HEMT noise photons we obtain with the two-dimensional Planck spectroscopy is in good agreement with the data sheet value of $n_{\mathrm{HEMT}} = 6.2$ provided by the HEMT's manufacturer (LNF). In order to verify this number, we perform a separate measurement, where we increase the temperature of the mixing chamber stage. Here, all of the microwave components can be treated as a single heatable attenuator at the mixing chamber temperature, as illustrated in Fig. 4.23(a). This places the self-calibrated signal source directly in front of the HEMT, without any losses in between, and ensures good accuracy of this method. Furthermore, heating the mixing chamber to 300 mK has only a negligible effect on the temperature of the 4K stage, where HEMT is mounted. Therefore, the performance of the latter is constant throughout this measurement. The measurement result is shown in Fig. 4.23(b). Fitting the measurement data according to Eq. 3.2 yields $n_{\mathrm{HEMT}} = 6.70$ noise photons added to the signal by the HEMT.

4.3.3 TWPA as tunable attenuator

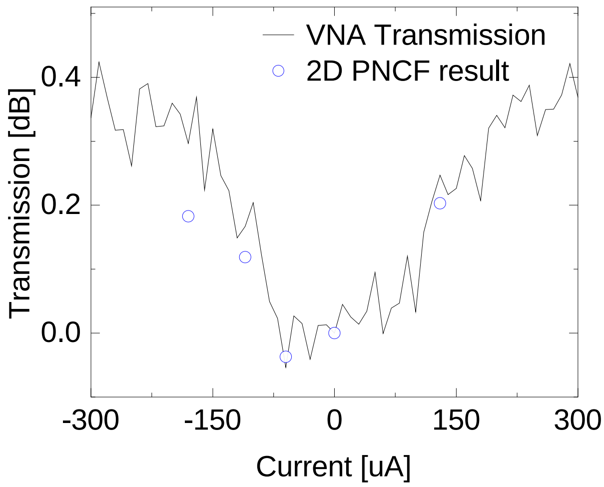

Figure 4.24: Transmission of the unpumped TWPA as a function of applied current measured with a VNA (solid line) and obtained from a set of two-dimensional Planck spectroscopies (blue circles). Both data sets are shifted vertically to obtain a transmission of 0 dB at a current of 0 uA.

To further explore the potential of the two-dimensional Planck spectroscopy, we utilize the tunability of the TWPA and use it as a ”flux-tunable attenuator”. To this end, we vary the TWPA flux bias by changing the bias current I_{dc}. First, we measure the total transmission, $S_{\mathrm{BA}}\left[(\Phi_{\mathrm{ext}}(I_{\mathrm{dc}}))\right]$, through the system as a function of the flux bias by performing a transmission measurement with a VNA, just as for the first characterization measurement of the TWPA in Sec. 4.2. Second, we perform multiple 2D PNCF measurements at different flux biases and use the fitting routine according to Eq. 4.3 to extract loss values $L\left[(\Phi_{\mathrm{ext}}(I_{\mathrm{dc}}))\right]$. The results of these measurements can be found in Fig 4.24. In order to compare the transmission obtained with the VNA measurement to the amount of losses obtained with the 2D PNCF approach, we only consider their respective change as a function of bias current, $\Delta S_{\mathrm{BA}}\left[(\Phi_{\mathrm{ext}}(I_{\mathrm{dc}}))\right]$ and $\Delta L\left[(\Phi_{\mathrm{ext}}(I_{\mathrm{dc}}))\right]$. To this end, we first perform reference measurements at a bias current of 0 uA and a frequency of 5.5 GHZ with both methods. We then subtract these values from each measurement point in order to obtain the change in transmission, $\Delta S_{\mathrm{BA}}\left[(\Phi_{\mathrm{ext}}(I_{\mathrm{dc}}))\right] = S_{\mathrm{BA}}\left[(\Phi_{\mathrm{ext}}(I_{\mathrm{dc}}))\right] - S_{\mathrm{BA}}\left[(\Phi_{\mathrm{ext}}(I_{\mathrm{dc}} = 0))\right]$ and $\Delta L\left[(\Phi_{\mathrm{ext}}(I_{\mathrm{dc}}))\right] = L\left[(\Phi_{\mathrm{ext}}(I_{\mathrm{dc}}))\right] - L\left[(\Phi_{\mathrm{ext}}(I_{\mathrm{dc}} = 0))\right]$, respectively. We see that, qualitatively, there is a good agreement between the two methods and the two-dimensional Planck spectroscopy is able to resolve loss changes smaller than 0.1 dB. However, for the TWPA bias currents smaller than -140 uA, the change in attenuation is smaller than the one expected from the VNA measurements. One possible explanation for this deviation is that, fundamentally, these two methods measure different quantities. With the VNA we measure the attenuation introduced to a rf-probe signal applied to the experimental setup. With the two-dimensional Planck spectroscopy, however, we measure a combination of the attenuation introduced to a broadband signal and the amount of noise that gets added to that signal. Here, the beam splitter relation establishes a connection between the losses and the amount of noise coupled from the bath to the incoming signal. However, this demands precise knowledge of the signals incident at both inputs of the beam splitter and, therefore, the bath temperature at which these signals are created. For the model we use to analyse the data, we assume that this bath temperature is the same as the temperature measured by the thermometers. This can be the case for a "simple" system like an attenuator. However, for more complex systems like the Josephson metamaterial, the electronic temperature of the noise coupling to the material can be different than the phononic temperature measured by the thermometer. Further analysis is needed to investigate whether the two-dimensional Planck spectroscopy could be employed as a method to determine the noise temperature coupling to a device. Here, one would determine the losses introduced by the microwave device under test beforehand and use a fit of Eq. 4.3 to determine the bath temperature for known losses L.

4.3.4 Noise performance of the TWPA

Finally, we want to use the 2D Planck spectroscopy to determine the noise properties of the TWPA in the nondegenerate regime. To this end, we perform the 2D PNCF with the TWPA bias current set to 95 uA. We pump the TWPA using the two-pulse scheme, similar to the squeezing measurements. By analyzing the first and second part of the measured traces individually, we obtain PNCF calibrations for the case of the undriven and driven TWPA. The frequency of the pump tone is set to 12 GHz and the carrier frequency is at 5.5 GHz with the related detection bandwidth of 400 kHz. A scheme of the setup can be found in Fig. 4.25. When the TWPA is pumped, the expression for the detected power is modified in comparison to Eq. 4.3, as the noise photons added by the amplification chain are not given only by the HEMT noise, n_{HEMT}, but by the noise contribution n_{total} of the TWPA and HEMT in a chained configuration. For known TWPA gain, G_{TWPA}, and HEMT noise photons, the noise photons added by the TWPA can be calculated using the Friis formula [103]

$$n_{\mathrm{TWPA}} = n_{\mathrm{total}} - \frac{n_{\mathrm{HEMT}}}{G_{\mathrm{TWPA}}} \quad . \tag{4.5}$$

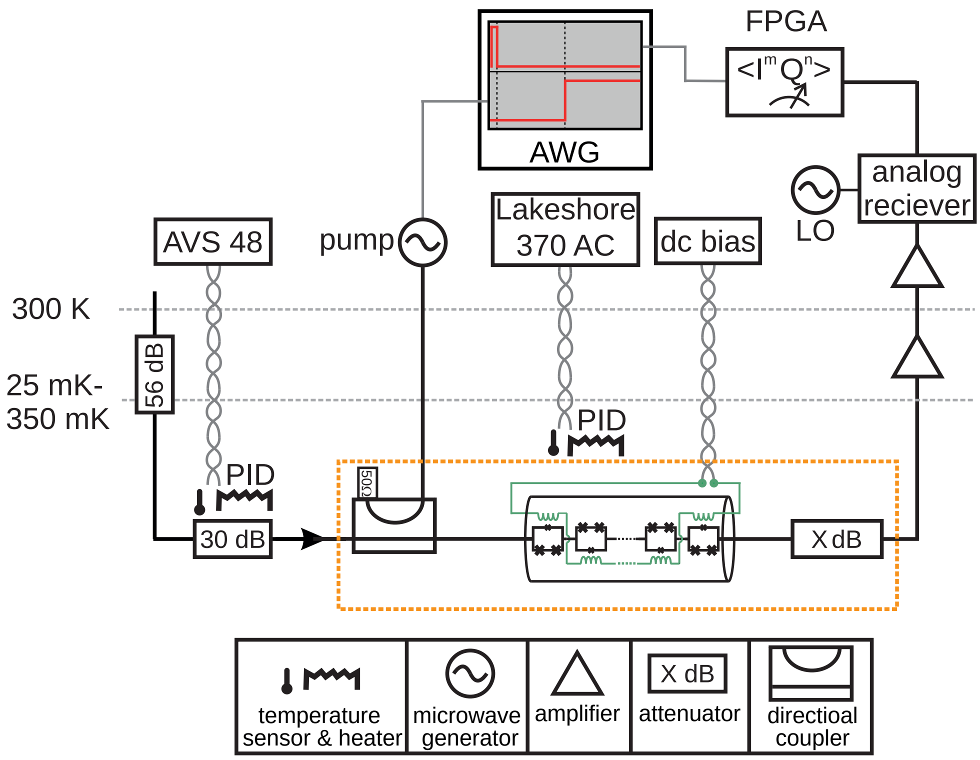

Figure 4.25: Schematic model of the two-dimensional Planck spectroscopy with the active TWPA. The orange rectangle indicates the region heated by the mixing chamber heater and, therefore, the location of the microwave losses L obtained with the 2D PNCF measurement.

We can calculate the gain of the TWPA by dividing the PNCF obtained with an active TWPA, κ_{on}, by the PNCF for the unpumped TWPA, κ_{off}

$$G_{\mathrm{TWPA}} = \frac{\kappa_{\mathrm{on}}}{\kappa_{\mathrm{off}}} = \frac{G_{\mathrm{off}} G_{\mathrm{TWPA}}\, R\,\Omega\, h f_0}{G_{\mathrm{off}}\, R\,\Omega\, h f_0} \quad . \tag{4.6}$$

Here, we have expressed the gain of the amplification chain with the active TWPA, G_{on} as a product of the TWPA gain and the gain of the amplification chain with the inactive TWPA, G_{off}. With access to the noise photons added by the TWPA, we can also use the quantum efficiency, η, to characterize its noise performance. The quantum efficiency is defined as the ratio between vacuum fluctuations in the input signal and total fluctuations in the output signal [112]. Therefore, η can be expressed as

$$\eta = \frac{1}{1 + 2 n_{\mathrm{TWPA}}} \quad . \tag{4.7}$$

The experimental results of the two-dimensional Planck spectroscopy with the two-pulse scheme can be found in Fig. 4.26. For the unpumped TWPA, one can notice that the

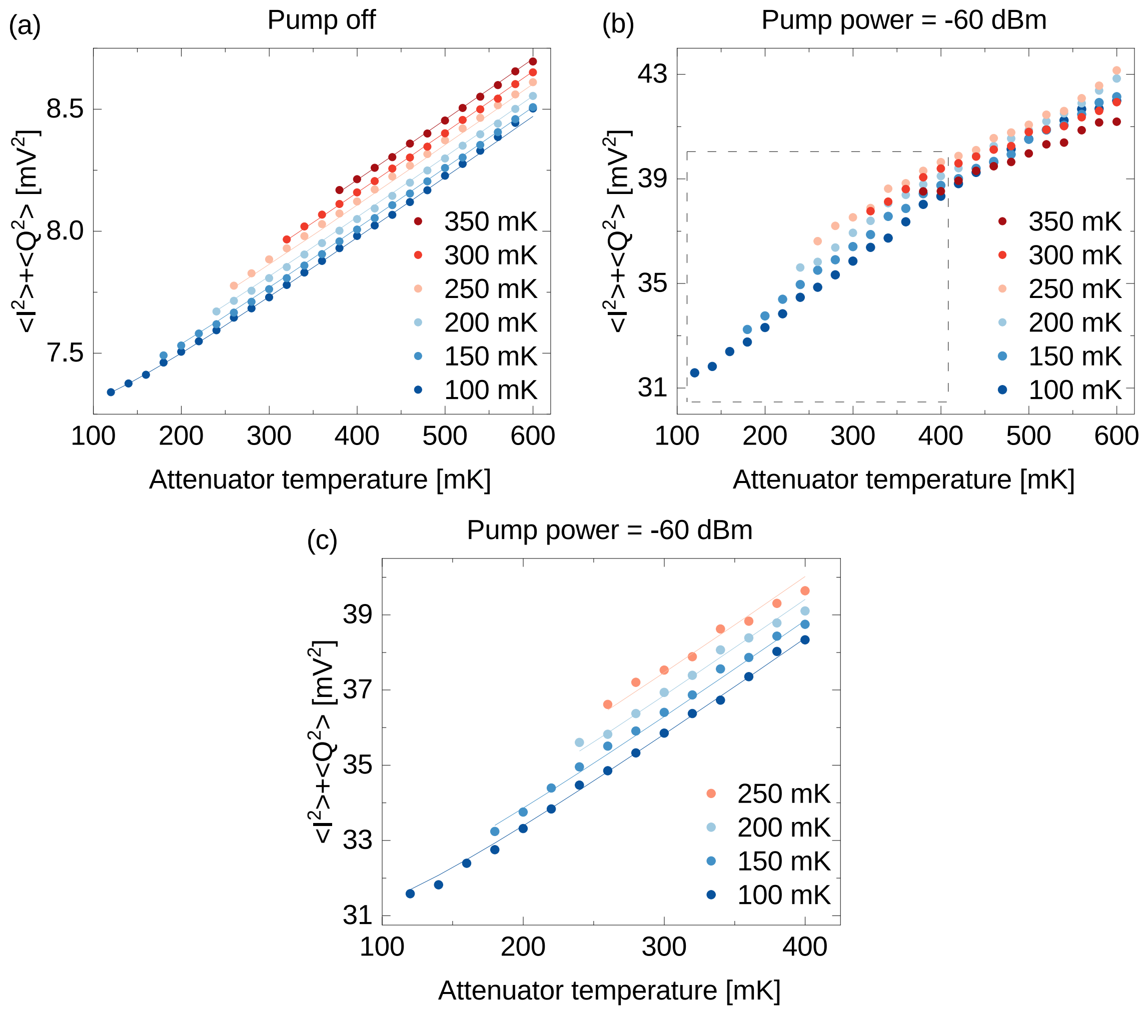

Figure 4.26: Two-dimensional Planck spectroscopy at the bias current of 95 uA for the unpumped (a) and pumped (b) TWPA. The frequency of the pump tone is 12 GHz and the carrier frequency is 5.5 GHz with the detection bandwidth of 400 kHz. The TWPA gain is 10.35 dB. (c) Zoom-in in the marked region in panel (b), where the compression effects of the TWPA are negligible. Symbols depict experimental data and solid lines are the corresponding fits according to Eq. 4.3.

spacing between different PNCF traces (corresponding to different T_{mc}) is smaller than for the measurement shown in Fig. 4.25(a). This indicates less losses present in the channel, according to Eq. 4.4. We extract the losses to be around 1.78 dB, compared to the value of 2.79 dB before, while the added noise photons stay at a similar value of $n_{\mathrm{HEMT}} = 6.68$. Most likely, this change in losses is due to the fact that the output circulator was exchanged from a Quinstar QCY-G0401201AS, with an insertation loss of 0.09 dB at the frequency of 5.5 GHz, to a PAMtech CTH1184-KS18, with an insertation loss of 0.19 dB at the frequency of 5.5 GHz, between these two measurements. As these data sheet values differ

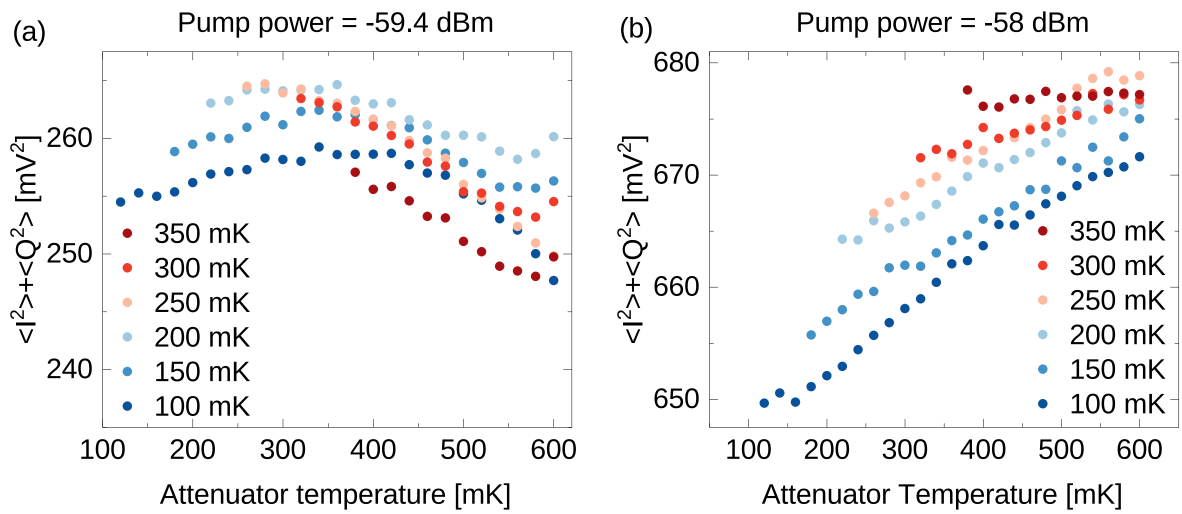

Figure 4.27: Compression effects for the strongly-pumped TWPA, $P_\mathrm{p} = -59.4\,\mathrm{dBm}$ (panel (a)) and $P_\mathrm{p} - 58\,\mathrm{dBm}$ (panel (b)), respectively. The given pump powers are referred to the input of the TWPA. The carrier frequency is 5.5 GHz with a detection bandwidth of 400 kHz.

only by 0.1 dB, there could be another source for these changes. This may be an improper impedance matching at one of the microwave connectors or a loose connection. This highlights the importance of the two-dimensional Planck spectroscopy - while the two experimental setups may look nearly identical on paper, in reality, their losses can be quite different from each other.

Panel (b) of Fig. 4.26 shows the results for the pumped part of the trace. The pump power of $-60\,\mathrm{dBm}$ corresponds to the gain of 10.35 dB. Here, we can observe the equidistant spacing between the different mixing chamber temperatures only up to 250 mK. The linear increase of detected power as a function of the attenuator temperature is only present up to 400 mK. For higher temperatures, we start to see deviations caused by compression effects. The latter are already visible at much lower gains and attenuator temperatures, as compared to similar measurements with the JPA [59], which has a much lower 1 dB-compression point. This behaviour can be explained by the broadband nature of thermal radiation from the heatable attenuator and the TWPA, that amplifies the signal over a broad bandwidth. At a temperature of $T_\mathrm{att} = 400\,\mathrm{mK}$, the heatable attenuator emits the total signal power P_s inside the bandwidth of the TWPA

$$P_\mathrm{s} = \int_{f_1=4\,\mathrm{GHz}}^{f_2=8\,\mathrm{GHz}} S\left(T_\mathrm{att}, f\right) \mathrm{d}f \approx -100\,\mathrm{dBm}. \tag{4.8}$$

This signal power is close to the 1 dB-compression point of the TWPA at the pump power of $P_\mathrm{p} = -60\,\mathrm{dBm}$, $P_\mathrm{1dB}\left(P_\mathrm{p} = -60\,\mathrm{dBm}\right) \approx -101\,\mathrm{dBm}$, which we measured with the VNA (see Fig. 4.16). For our analysis of the TWPA noise properties, we neglect the

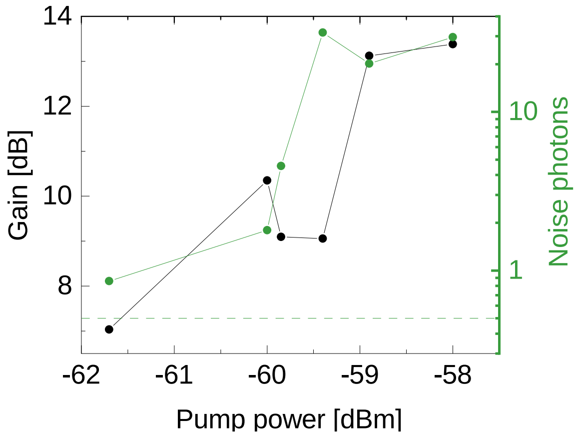

Figure 4.28: Gain and added noise photons of the TWPA as a function of the pump power referred to the input of the TWPA sample box. The dashed line represents the SQL of half a noise photon added to the amplified signal.

region where compression becomes apparent. The corresponding cut-off is marked by the dashed line in Fig. 4.25(b) and is independently shown in Fig. 4.25(c). We fit the data show in this panel (c) and obtain $n_{\mathrm{TWPA}} = 1.79$, $\eta = 0.21$. Next, we can try to increase the gain of the TWPA by increasing the pump power. Then, we observe that first, the number of noise photons starts to increase and gain starts to decrease, as compression effects start to get stronger. A corresponding measurement in this regime can be seen in Fig. 4.27(a). If we continue to increase pump power even further, the gain starts to increase again and the noise added by the TWPA stays at a rather high level of more than 10 noise photons, or, quantum efficiency of less than 5%. Here, while still visible, compression effects are less pronounced, as can be seen from Fig. 4.27(b). The number of noise photons added by the TWPA, as well as its gain, as a function of the pump power are shown in Fig. 4.28. If we calculate the noise performance for the case where we use the data sheet losses of the microwave components, instead of the losses obtained by the 2D PNCF, the added noise photons will be underestimated.

Using multiple amplifiers at cryogenic temperatures in a pulsed manner theoretically allows us to independently determine the losses between the amplifiers. In our case, using only the HEMT gives us access to all of the losses coupled to the mixing chamber temperature. If we turn on the HEMT and the TWPA, the total losses obtained with the fitting routine decrease, as the impact of losses after the first amplifier reduces, according to the Friis formula [103]. In the high gain limit of the first amplifier, we would only obtain a contribution of the losses in front of this amplifier, thus allowing us to divide the system in individual subsections. For the case of the TWPA measurements, the first subsystem, between the 30 dB heatable attenuator and the TWPA, contains exactly the losses we need to take into account for shifting the reconstruction point of the quantum state during the reference state reconstruction. Access to this subsystem would allow us to completely discard assuming data sheet losses during data processing, even for shifting of the reconstruction point. However, in our experiments, the low gain of the TWPA when amplifying a broadband signal does not allow us to make use of this result.

Chapter 5

Microwave quantum local area network

In this chapter, we present a cryogenic link connecting two dilution cryostats spatially separated by a distance of 6.5 m. Utilizing a superconducting microwave cable, we create an elementary microwave quantum local area network (QLAN). In Section 5.1, we discuss our design of the cryolink, including main cryogenic components and the superconducting transmission line. We present the cryolink performance and analyze its limitations. Section 5.2 concludes this chapter by presenting an experiment on microwave entanglement distribution between distant nodes.

5.1 Cryolink assembly

The cryogenic link has been designed in close collaboration between OINT and the Walther-Meißner-Institute in the framework of the Quantum Microwave Communication & Sensing project, funded by the European Quantum Flagship program. In this section, we discuss the design of this system and its performance. Our cryogenic local network consists of five main elements. First, there are the Alice (designed and built at WMI) and Bob (Triton, OINT) dilution refrigerators, both of which have been introduced in Sec. 3.1. Then, there is a cold network node (CNN) located in the Eve lab. This lab is located between the Alice and Bob labs. To be consistent with the naming scheme throughout this thesis, we call this cryostat Eve. The last components forming the cryogenic local network are two link arms, with the length of 2.2 m each, which are connecting Alice to Eve and Eve to Bob. A scheme and a photograph of the cryogenic link is shown in Fig. 5.1. Eve is a commercial 4 K cryostat from OINT which contains only PT1 (50 K) and PT2 (4 K) stages. In the current configuration, there are no microwave input and output lines in the Eve cryostat and it contains only dc-looms for temperature readout. As in the Bob croystat, we use a 24 pin LEMO connector at the vacuum feedtrough and a BeCu-loom for temperatures higher than 3 K. Below the PT2 stage, we use a superconducting loom made from NbTi. We thermalize the superconducting looms by wrapping them around OFHC copper cylinders that are fixed at various temperature stages of the cryostat. To ensure a good thermal contact, we glue the looms to the cylinders with GE varnish. All the lines used for thermometry are filtered with the low-pass filters described in Sec. 3.1.

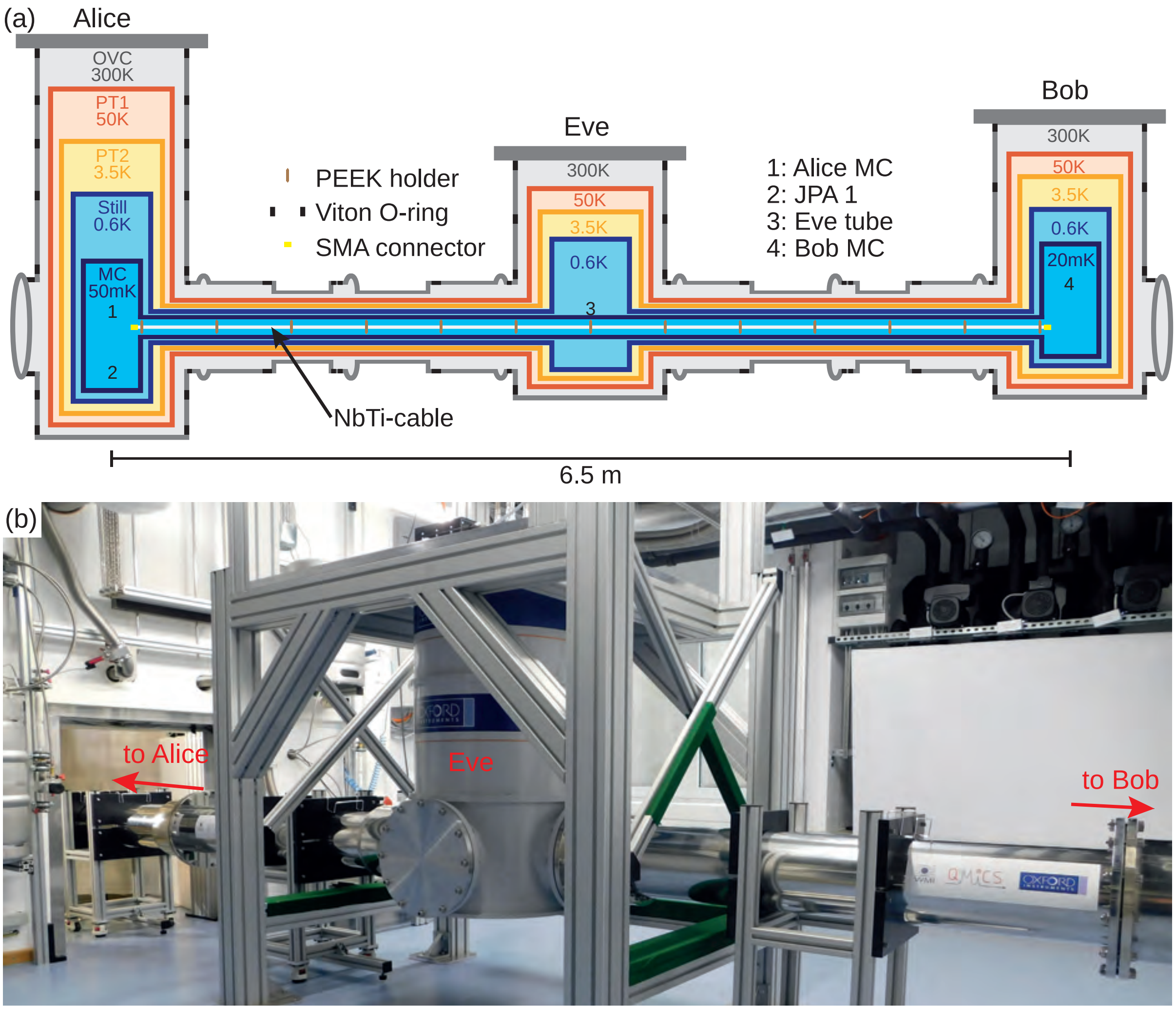

Figure 5.1: (a) Schematic drawing of the complete cryolink system. The numbers 1 to 4 indicate the positions of important thermometers throughout the system. (b) Photograph of the cryolink. The Eve lab also houses parts of the cryogenic infrastructure needed to run the cryostats, such as pumps and compressors.

The cryogenic Alice-Eve and Eve-Bob link arms have the same inner shielding layout as the respective dilution fridges. A schematic cross-section of this layout can be found in Fig. 5.1(a). A photograph illustrating this inner structure is shown in Fig. 5.2. Each temperature stage of the link arm, except those for the mixing chamber and the outer vacuum shield, is equipped with stainless steel bellows which allow for limited flexibility under thermal contraction forces. Due to the low heat conductivity of stainless steel, additional copper braids span across the bellows in order to provide a good thermal contact across them. A detailed image of these elements can be seen in Fig. B.1(a). We determine the gaseous volume of the OVC, in order to relate the pressure inside the OVC to a volume of gas during later analysis of the system. To this end, we fill the evacuated

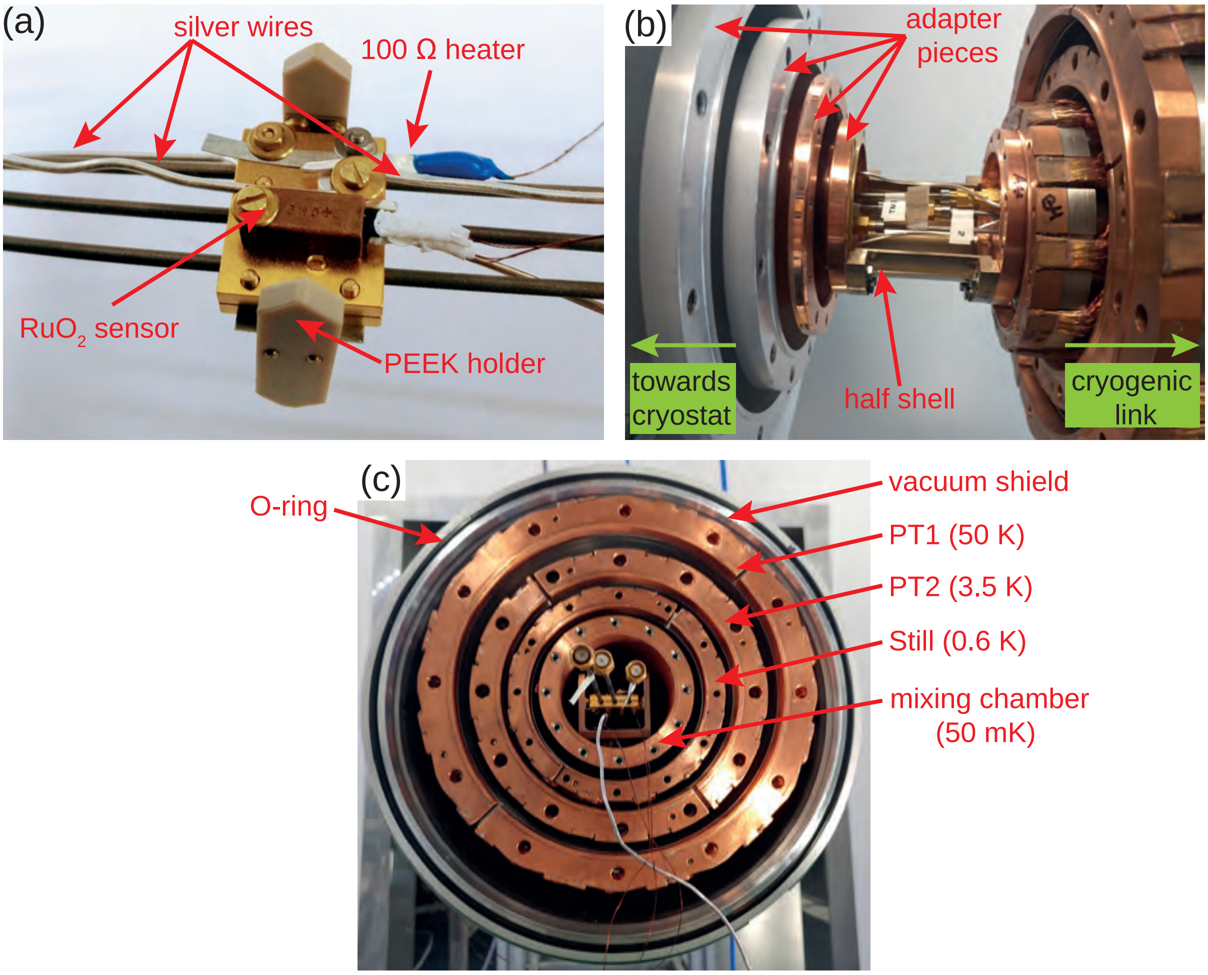

Figure 5.2: (a) Photograph of the superconducting cable assembly used as a microwave quantum channel inside the cryogenic link. The entire cable is supported by 13 of such holders. This particular element shown here is equipped with a heater and thermometer to allow for temperature stabilization. Silver wires are used for thermalization of the cables. (b) Photograph of the connection interface between the Bob fridge and the link arm. (c) Photograph of the different temperature shields of the link arm and the respective superconducting microwave cable. The stages are equipped with copper faces where the copper braids are attached to.

vacuum can with a known amount of gas and measure the pressure increase inside the OVC. Here, we obtain a volume of $933 \pm 229\,\mathrm{l}$. The large error stems from different values read from three pressure gauges.

Assembling the cryolink

In order to connect the cryostats to the link arm, the lowest shields on Eve and Bob and the second lowest shields on Alice are equipped with holes with the diameter of the corresponding temperature stage of the link arm. Flat faces surrounding these holes allow us to attach the cylindrical adapter pieces using 12 stainless steel screws of varying sizes each. On the mixing chamber stage we use these screws in combination with molybdenum washers. These washers can compensate for the difference in thermal expansion between the copper shields and the stainless steel screws, which ensures a proper mechanical and thermal contact at millikelvin temperatures. A picture of these adapter pieces can be seen on the left side of Fig. 5.2(b). The adapter pieces mirror the shields of the cryostat and their materials, i.e. aluminum for the PT1 and PT2 stages, and OFHC copper for the still and mixing chamber shields. The PT1 stage shields are covered in 10 layers of superinsulation.

We form a connection between the adapter pieces and the link arms by using cylindrical, c-shaped, half shells. One of the two half shells used on the mixing chamber stage can be seen in the middle of Fig. 5.2(b). To insert the half shells we make use of the stainless steel bellows by compressing them. This opens the gap between the adapter pieces and the link arm far enough to insert the half shells. From Fig. 5.2(b), we can also see that the adapter pieces and copper interfaces on the link arm are equipped with small ridges on the surfaces facing each other. These ridges help to align and connect the shield counterparts. We wrap the PT1 half shells with two 10 layer superinsulation foils and cover all open slits with aluminum tape to protect against thermal radiation. For proper lateral orientation between the adapter pieces and the link arm itself, all of the cryostat shields are equipped with elongated holes for fixing them to the shield above. This allows us to rotate these shields by a few degrees in the horizontal plane. The proper alignment between cryostat and the link arms is of utmost importance, as it guaranties a good mechanical and thermal contact between the adapter pieces, the half shells and the link arm. Furthermore, the correct alignment reduces the mechanical forces which are exerted on the system. These forces must not be underestimated, as we observe the frame carrying the Bob cryostat shifting on the floor by a few mm after every cooldown. Once all inner shields of the cryolink are closed, we close the outer vacuum shields. To this end, a part of the link arm vacuum shield can be slid over the half shells towards the vacuum shield of the cryostat. Viton O-rings are used to form a vacuum-tight connection between the link arm and the fridge side-flange. Their positions are indicated in Fig. 5.3(a). Here, the correct alignment of the vacuum shield is important, as the vacuum can is not equipped with any flexible elements and the O-ring needs to be compressed evenly around its circumference to provide a reliable vacuum isolation. To this end, all three cryostats are equipped with systems to move them into proper positions. For the Bob and Eve cryostats, the cryostat top-plate is resting on the frame top-plate, as it is illustrated in Fig. 5.3(b). This frame top-plate has a circular cut-out that is significantly larger than the diameter of the cryostat. The two aluminium plates are separated by plastic gliders. These gliders allow us to push the cryostat top-plate in the horizontal plane using stainless steel screws. After we finish the horizontal alignment, vertical movement is achieved by lowering the vertical screws, lifting

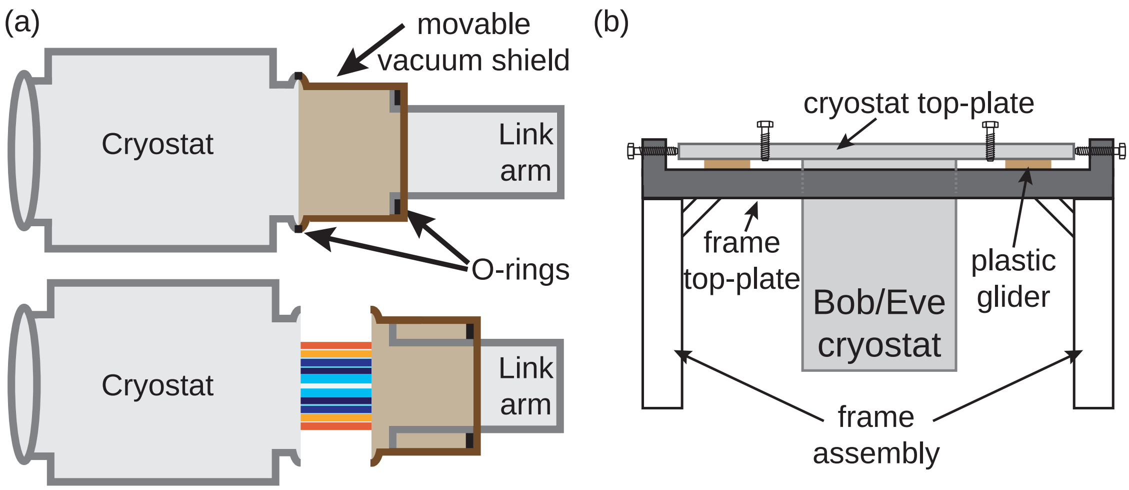

Figure 5.3: (a) Schematic cross-section of the cryostat and the link arm. The upper picture shows the vacuum shield of the link arm in the closed position. Two O-rings (each one indicated by pair black rectangles) seal the system. The lower picture shows the vacuum shield of the link arm in the open position, slid black. (b) Schematic drawing of the mechanism used to align the Bob and Eve cryostats. All screws are placed in threaded holes.

the cryostat top-plate from the frame top-plate. The Alice cryostat is different in this respect from Bob and Eve. It rests on three pneumatic vibration isolators which allow us to change the height and the angle of the cryostat by changing the pressure inside the isolators. The forces acting on the system shift the cryostats during a cooldown which brings the need for a complete realignment of the system each time before closing. In order to speed up the process of the cryolink closing, the rigid outer vacuum shells could be exchanged for flexible, vacuum-tight, bellows. However, calculations carried out by OINT estimate that the contraction forces, due to atmospheric pressure, of these bellows would be around 3 kN. In order to withstand such forces, a different, more stable design of the cryostats and support carts would be required.

5.1.1 Superconducting microwave transmission line

We use superconducting coaxial cables inside the cryolink in order to realize the QLAN. We employ custom-made, 6 m long, coaxial NbTi cables produced by Keycom for this purpose. These cables are inserted in the innermost tube of cryolink and thermally anchored to the mixing chambers of the Alice and Bob fridges. In total, three of these cables are placed inside the cryogenic link. They are fixed by 13 holders illustrated by Fig. 5.1(a). Each of these holders is made out of a polyether ether ketone (PEEK) frame and contains a clamp made from gold-plated OFHC copper. The central one, placed directly underneath the Eve fridge is visible in Fig. 5.2(a). It is equipped with a 100 Ω

heater and a RuO_2 thermometer allowing for temperature stabilization using an external PID control loop. Both the top and the bottom of the PEEK holder are tip-shaped to minimize the contact area to the mixing chamber tube. This ensures a good thermal decoupling of the cables from the mixing chamber tube, provided by the low thermal conductivity of the PEEK material [140]. Another benefit of minimizing the contact area between the holders and mixing chamber tube is a reduced mechanical friction. This allows the holders to move freely along the tube and reduces mechanical strain on the cable during cooldowns. Furthermore, this helps with connecting the link, as the cables can be easily slid in or out of the link arm by a few cm. For thermalization of the holders, and respectively the superconducting cables, we use two-high purity silver wires clamped to the mixing chambers of the Alice and Bob fridges. Finally, we use 4 m long, superconducting dc-wires to connect to the cable temperature sensor and heater under the Eve fridge directly through the cryolink from the side of the Bob fridge.

5.1.2 Cryolink performance

In this subsection, we describe the experimental characterization of the cryolink performance. In order to achieve the to-be-demonstrated results, several major modifications of the entire cryolink system have been implemented. Those are presented in details in Appendix B in order to streamline presentation of the main results.

Cooldown procedure

The first step in the cooldown procedure consists in evacuation of the outer vacuum chamber of the entire cryolink. To this end, we connect one external turbo molecular pump (TMP) to the Alice cryostat and another TMP to the Eve cryostat and pump the system down to the pressures of around 1×10^{-2} mbar, which takes roughly two full days. After reaching the desired pressure in the OVC, we start pre-cooling the system by switching on the PTRs in all fridges. We keep both of the TMPs connected to the OVC during the cooldown procedure. Figure 5.4 illustrates the temperatures during the cooldown process. Here, one can see that the optimized cryolink (see App. B for details) achieves similar steady-state pre-cooling temperatures, as compared to the independently operated Alice fridge. After the pre-cooling is finished, we start condensing the ^{3}He/^{4}He mixture. After another 10 hours, we reach millikelvin temperatures at the mixing chamber stages, as illustrated in Fig. 5.4(c). Once the mixture is completely condensed and circulating, we observe the best performance when applying a heating power of around 400 μW to the still heater of the Bob cryostat, while keeping the still heater at Alice idle. In this configuration, the steady-state mixing chamber temperatures reach around 53 mK at Alice, 55 mK at Eve, and 23 mK at Bob, as it can be seen from Fig. 5.4(d). The center of the superconducting microwave cable reaches a temperature of less than 97.4 mK. Notably, this temperature was only achieved after adding the low-pass filters mentioned

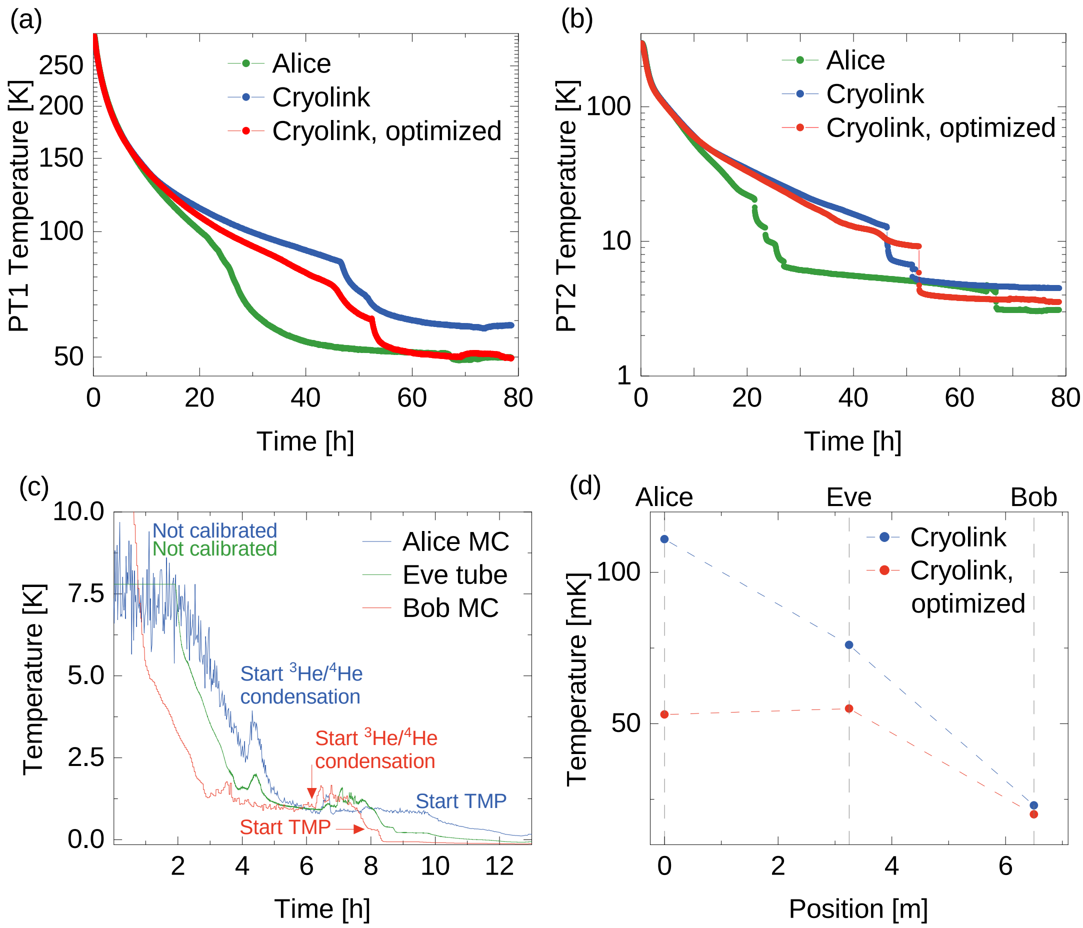

Figure 5.4: Panels (a) and (b) illustrate temperatures of the PT1 and PT2 stages of the Alice cryostat during the cryolink cooldown, respectively. (c) Mixing chamber temperature at Alice, Eve, and Bob after pre-cooling is finished (d) Mixing chamber temperature at Alice, Eve, and Bob after the cooldown procedure is completed.

in Sec. 3.1 to the input lines of Alice, connected to the QLAN. It reduces the temperature of the cable at the center of the link by roughly 5 mK. Furthermore, heating the mixing chamber of Bob to 300 mK results in an increase of the mixing chamber temperature at Alice to 85 mK and the Eve mixing chamber tube temperature to 278 mK. This shows a rather weak thermal coupling between the mixing chamber stages of Alice and Bob and allows us to run a wide variety of measurements in both cryostats, rather independently from each other. Overall, the temperatures of both the mixing chamber tube at Eve and the cable are limited by the performance of the Alice cryostat. In the near future, we hope to improve the overall cryolink performance by introducing further upgrades, such as extra heat exchangers, to the Alice cryostat.

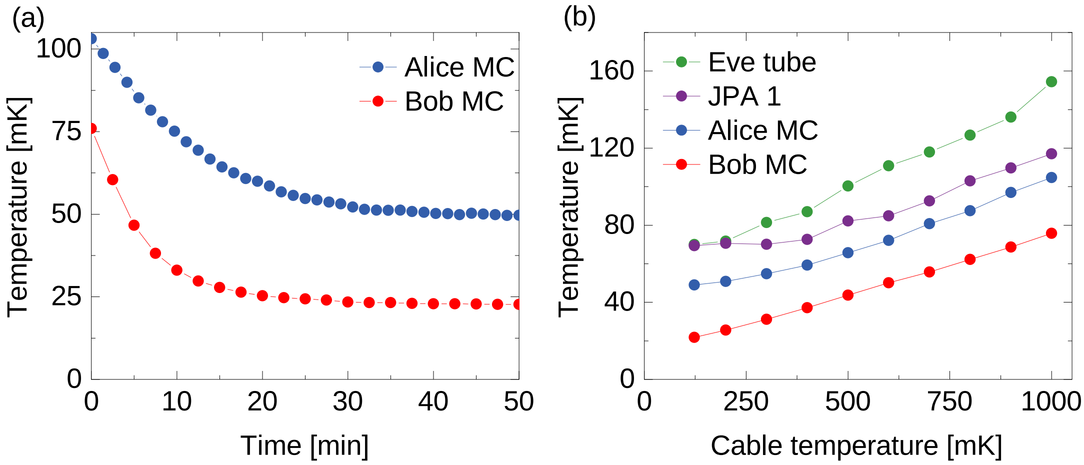

Figure 5.5: (a) Temperatures of Alice and Bob mixing chambers (MCs) after heating the cable to the temperature of 1 K as a function of time delay after turning off the heater. (b) Steady-state temperatures of various elements of the Cryolink when heating the middle of the superconducting microwave cable. The positions of the thermometers corresponding to each graph are indicated in Fig. 5.1(a)

Heating of the superconducting microwave transmission line

Here, we want to characterize the temperature distribution along various components of the cryogenic link. To this end, we utilize the heater and thermometer attached to the center of the superconducting QLAN cable. Figure 5.5(a) shows both the Alice and Bob mixing chamber temperatures as a function of time delay after heating the center of the cable to 1 K and then turning off the heater. Here, on can see that the Bob fridge drops to the mixing chamber temperature of 30 mK in less than 15 minutes and reaches its base temperature of 23 mK within half an hour, while the Alice fridge takes 45 minutes to cool down. A similar experiment can be conducted with heating the cable center to 4 K. Here, the mixing chamber stage on both sides reaches temperatures of 370 mK. However, in this case, rising condensor pressures on the Alice side did not allow for stable operation of the system even after the heater is turned off, forcing us to stop the cryolink operation and re-collect the ^{3}He/^{4}He mixture. Figure 5.5(b) shows the equilibrium temperatures of various components of the cryogenic link as a function of the temperature of cable center. Here, it can be seen that the slope of different graphs is quite similar and the offset between them stays constant. For low cable temperatures, the JPA temperature is constant, as the latter is stabilized to an elevated temperature of 70 mK.

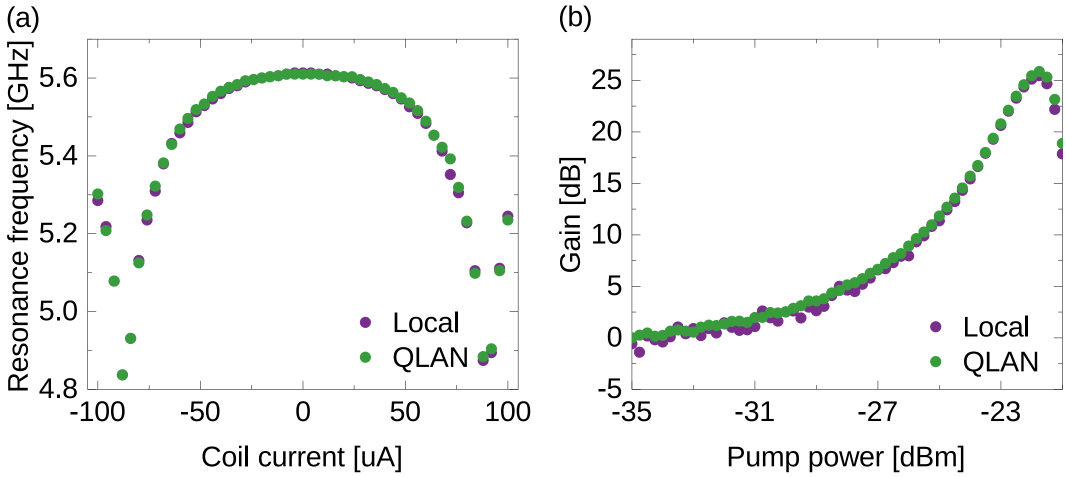

Figure 5.6: Flux dependence (a) and nondegenerate gain (b) measurements performed both locally in the Alice cryostat and over the cryogenic link. Due to good agreement between the data obtained via the two different outputs, some points corresponding to the local measurement are completely covered by the data gained from the measurement over the QLAN.

5.2 Microwave quantum communication over the cryogenic link

One of the key features of the cryogenic link is its ability to transfer microwave quantum states over macroscopic distances while preserving their quantum properties. In our experiments, we demonstrate these capabilities of the cryogenic link by using it to transfer squeezed vacuum states and distribute quantum entanglement between the two locally separated parties, Alice and Bob. We investigate robustness of the entanglement distribution by locally increasing the temperature of the superconducting microwave cable connecting Alice and Bob, thus, implementing a microwave thermal channel.

5.2.1 VNA measurements over the cryogenic link

For first measurements utilizing the cryogenic link, we perform two sets of VNA measurements with superconducting flux-driven JPAs. We compare results of such measurements implemented locally in the Alice fridge with those implemented via the microwave QLAN, using the 6 m cryolink microwave channel as an output line with the Bob cryostat. The results of these measurements, a flux sweep and nondegenerate gain measurements, are shown in Fig. 5.6. As expected, the data obtained via both outputs coincides very well. This indicates that the superconducting cable inside the cryolink is properly thermalized and does not induce significant losses.

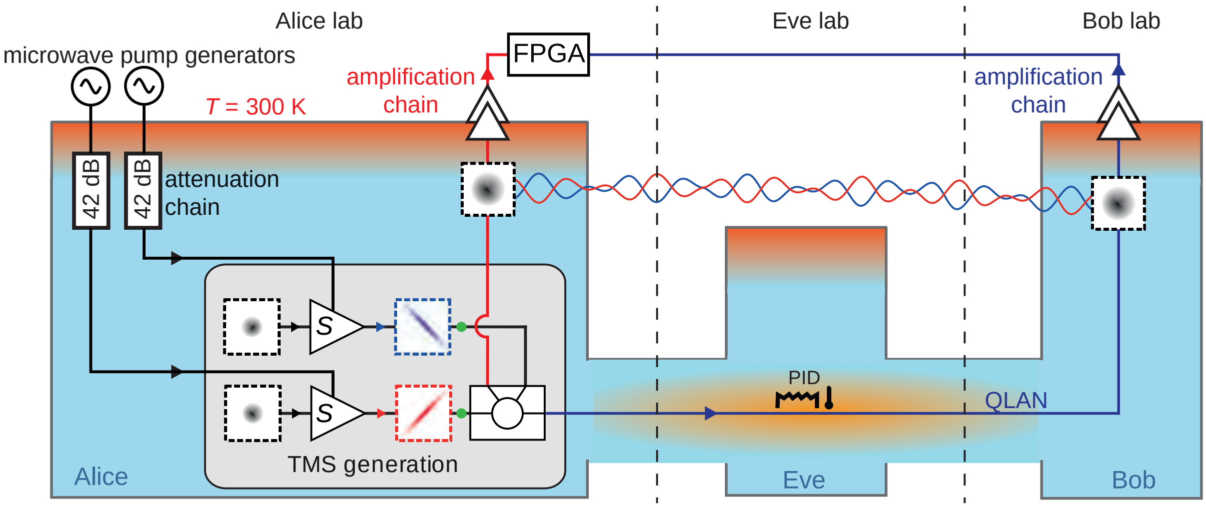

Figure 5.7: Scheme for the entanglement distribution over the cryolink. The JPAs are stabilized at the temperatures of 60 mK. Operating the JPA pump sources in a pulsed regime allows us to examine the squeezed state generated by each JPA individually, as well as the symmetric TMS state at the hybrid ring outputs when both JPAs are active. The green dots represent the reconstruction points for the "corrected" squeezing measurement in Fig. 5.8.

5.2.2 Entanglement distribution

One could note that the measurements shown previously could easily be achieved by strongly amplifying the JPA output signals and transmitting them via room temperature cables. However, this approach is not applicable for genuine quantum states, as amplifying these would eliminate their quantum features. Therefore, in the absence of quantum error correction, we have to use a genuine quantum channel with near-zero transmission losses - such as the microwave QLAN.

Quantum state transfer

To implement the quantum state transfer, we use a setup shown in Fig. 5.7. First of all, we use only one of the JPAs for generation of a propagating squeezed vacuum state. The latter propagates towards a hybrid ring, which acts as a balanced, 50:50, beam splitter. One of the hybrid ring outputs is connected to the local output line of the Alice cryostat, while the other one is connected to the output line of the Bob cryostat via the QLAN cable. The latter is at the base temperature of 100 mK. Both the amplified signals leaving the Alice and the Bob cryostat are measured with the FPGA setup in the Alice lab and reconstructed using the reference state method, identical to the previous squeezing measurements. From Fig. 5.8 we can see that the squeezing levels and purities of the squeezed states measured locally and over the QLAN coincide well. The slightly lower squeezing levels for the local output are a result of a more noisy HEMT in the Alice output

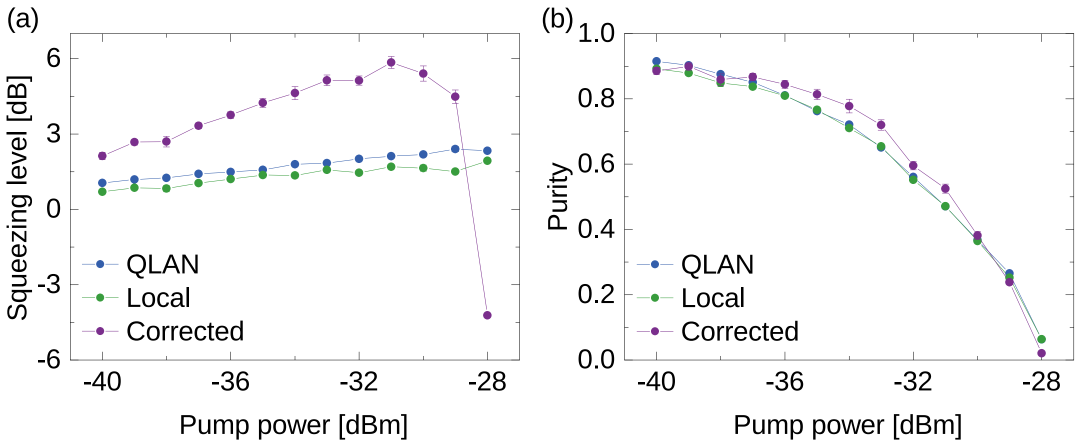

Figure 5.8: Squeezing level (a) and purity (b) as a function of the JPA pump power. The pump powers are referred to the input port of the JPA sample box and the working point is set at $f_0 = 5.6\,\mathrm{GHz}$. The detection bandwidth is 430 kHz. "QLAN" represents the state sent across the superconducting microwave cable inside the cryolink and "Local" corresponds to the one measured via the output of the Alice fridge. "Corrected" denotes the state at the reconstruction point indicated by the green dot in Fig. 5.7. For "Local" and "QLAN" the squeezed states are reconstructed at the respective output of the hybrid ring.

line as compared to the one in the Bob fridge. We note, that these squeezing levels are limited to 3 dB, due to mixing of the squeezed state (from the JPA) with a weak thermal state (the other JPA is inactive) at the hybrid ring. We can shift the reconstruction point during the data processing step by taking input-output relations of the hybrid ring into account and obtain respective input squeezing levels in excess of 6 dB, as illustrated by the trace "corrected" in Fig. 5.8.

Entanglement distribution over the cryolink

As the most important experimental step, we want to distribute microwave quantum entanglement over the cryogenic link. To this end, we employ both JPAs placed inside the Alice fridge to generate squeezed states with same frequency and equal squeezing amplitude but orthogonal squeezing angles. Sending these squeezed states to the inputs of the hybrid ring results in generation of a two-mode squeezed vacuum state. Both of the TMS paths are simultaneously detected by the FPGA and a complete covariance matrix of this two-mode signal is reconstructed. First, we balance these TMS states. To this end, we use the variance ratio, $\sigma_{\mathrm{r}}^2 = \sigma_{\mathrm{a},1}^2/\sigma_{\mathrm{s},1}^2 \cdot \sigma_{\mathrm{a},2}^2/\sigma_{\mathrm{s},2}^2$, as a measure of asymmetry of the TMS state. Here, $\sigma_{\mathrm{a,i}}^2$ and $\sigma_{\mathrm{s,i}}^2$ are the antisqueezed and squeezed variances of the local states at the hybrid ring outputs and $i = 1, 2$ denotes the path of the output signal. Here, "1" corresponds to the Alice output and "2" to the Bob output. For a perfectly

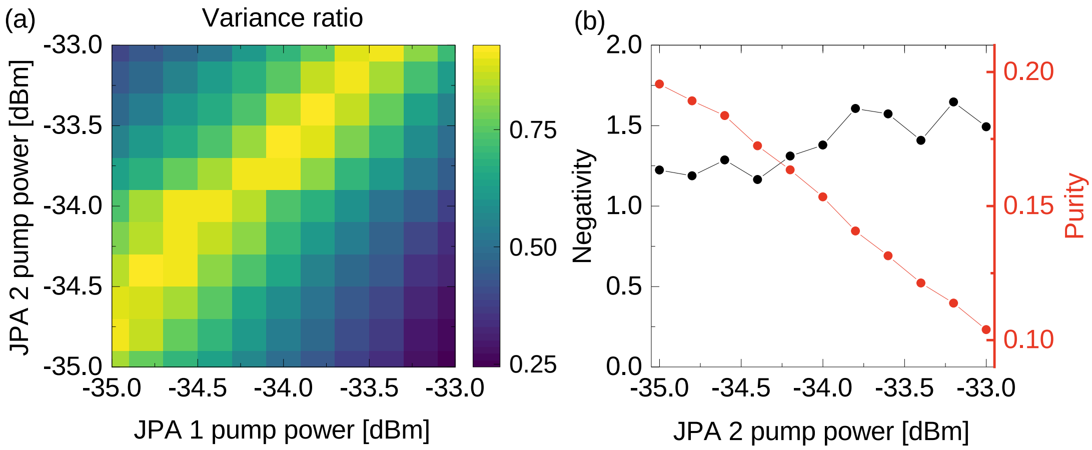

Figure 5.9: Balancing of a two-mode squeezed state over the cryolink. The pump powers are referred to the input of the sample box with the common working point at $f_0 = 5.6\,\text{GHz}$. (a) Variance ratio σ_r^2 as a function of the JPA 1 and JPA 2 pump powers. We stabilize the squeezing angles of the SMS states produced by the respective JPAs at $\gamma_1 = 45°$ and $\gamma_2 = 135°$. (b) Negativity and purity as a function of the JPA 2 pump power, while the JPA 1 pump is kept unchanged at $P_\text{p,JPA1} = -35.0\,\text{dBm}$.

balanced TMS state, we expect $\sigma_\text{r} = 1$, as we would have $\sigma_\text{a,i}^2 = \sigma_\text{s,i}^2$. However, in reality JPAs produce squeezed states with different squeezing and antisqueezing levels. At the same time the hybrid ring can be slightly asymmetric and propagation losses can differ between the different paths. All these asymmetries must be balanced by adjusting the pump powers and phase of the corresponding JPAs. Figure 5.9(a) shows the result of such a balancing measurement. Here, we see that we are able to distribute a balanced TMS state with a maximum variance ratio of $\sigma_\text{r}^2 = 0.92$. Furthermore, we use negativity as a measure of quantum entanglement according to Eq. 2.24. Negativity as a function of the JPA 1 pump power is shown in Fig. 5.9(b). With a negativity of up to $N = 1.6$, we demonstrate a successfully distribution of entanglement between the spatially separated parties Alice and Bob. The rather low purity of the TMS state is, again, a result of a more noisy HEMT in the Alice output line as compared to the one in the Bob fridge.

Entanglement distribution over the thermal channel

Lastly, we want to test the quantum state transfer of squeezed states through a microwave thermal channel. This can be achieved by elevating the temperature at the center of the superconducting cable connecting Alice with Bob to temperatures to around 1 K using the installed $100\,\Omega$ heater and the RuO_2 thermometer, as described in Sec. 5.1. As discussed for the 2D PNCF, we can model losses in this QLAN cable by utilizing the beam splitter model, where thermal noise couples to the propagating microwave

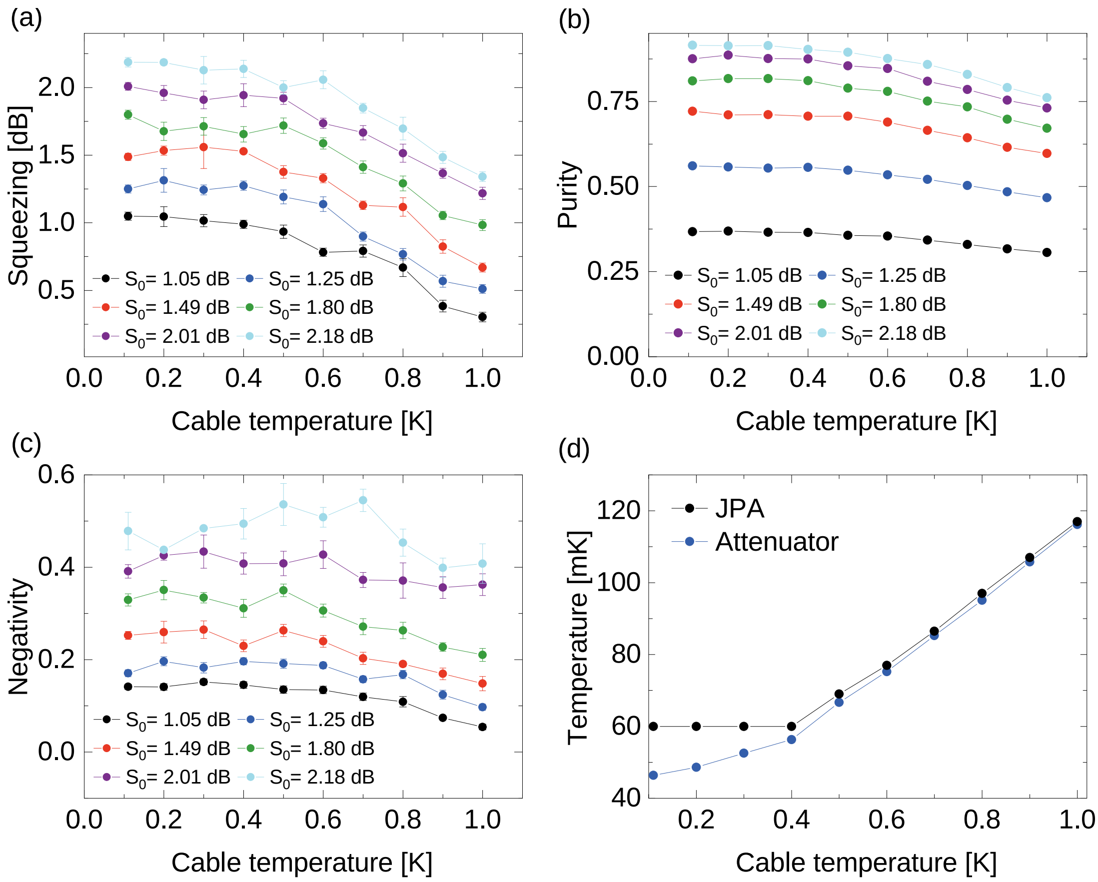

Figure 5.10: Distribution of entanglement across the QLAN at elevated cable temperatures. The carrier frequency is $f_0 = 5.6\,\mathrm{GHz}$. Squeezing level (a), purity (b), and negativity (c) stay rather constant for cable temperatures up to 0.4 K. At higher temperatures we observe a degradation of these properties as a result of direct increase of the JPA temperatures due to the thermal crosstalk. The squeezed state is reconstructed at the output of the hybrid ring connected to the QLAN. (d) JPA and attenuator temperature as a function of the cable center temperature. The JPA is stabilized to 60 mK.

signal via small but non-zero cable losses. This effective coupled thermal noise reduces quantum correlations, such as local squeezing, in the propagating signal. The propagation microwave losses in the QLAN cable are very low and only weakly change as a function of temperature around or below 1 K. Therefore, the resulting coupled number of thermal photons remain low even for the QLAN channel temperatures around 1 K. Thus, as long as the channel temperature remains much lower than the critical temperature of the related superconductor (NbTi in this case with $T_c = 9.8\,\mathrm{K}$) $T \ll T_c$, the heating of the QLAN has very small effect on quantum properties of the propagating signals. The experimental test of such measurements can be seen Fig. 5.10. Here, we repeat the same measurements over the QLAN as presented in Fig. 5.8, but increase the temperature of the center of the superconducting cable. We can see that squeezing level, purity and negativity are rather constant for temperatures of up to 0.4 K. For higher temperatures, all of the aforementioned quantities start to decrease. This is due to the fact that heating of the center of the cable leads to an increase of the temperature of the attenuator creating the input state of the JPA, as well as the temperature of the JPA itself, as can be seen from Fig. 5.10(c). The increase in the attenuator temperature can be taken into account by approximating the reference state used for the state reconstruction as a thermal state with corresponding temperature. However, the increase in JPA temperature leads to an increase of the effective noise temperature, decreasing the output squeezing levels. Overall, we observe that squeezing and entanglement stay indeed constant over a wide range of temperatures indicating that cryogenic channel is robust against the ambient thermal noise as long as the propagation losses are low and there are no direct thermal crosstalks. This can also be considered as the experimental proof of the fluctuation-dissipation theorem, which states that the linear response of a given system to an external perturbation is expressed in terms of fluctuation properties of the system in thermal equilibrium [141]. In our case, this means that any losses will couple thermal noise to the squeezed signal, degrading its purity and squeezing level. Therefore, if there are no losses present, no ambient thermal noise couples to the signal and the measured quantum state is independent of the temperature of the superconducting cable.

Chapter 6

Conclusion and outlook

In this work, we have investigated, both theoretically and experimentally, parametric amplification with two different kinds of Josephson junction-based parametric amplifiers: the resonator-based, flux-driven Josephson parametric amplifier (JPA) and the Josephson traveling wave parametric amplifier (TWPA). Here, we have considered the JPA designs featuring more than one direct current superconducting interference device (dc-SQUID), which can lead to an improvement in their 1 dB-compression point. We have introduced the superconducting nonlinear asymmetric inductive element (SNAIL) as the central building block of the TWPA. We have discussed that the SNAIL allows for three-wave mixing with a vanishing Kerr-nonlinearity for an asymmetry ratio of $\alpha = 0.3$ and a flux bias of $\Phi_{\mathrm{ext}} = 0.4\,\Phi_0$. The absence of the Kerr-nonlinearity strongly enhances the phase matching between the signal, idler, and pump tones, maximising the TWPA gain.

Next, we have implemented two experimental setups in order to compare the performance of both types of amplifiers. Here, we have studied properties of the devices such as their nondegenerate gain, bandwidth, 1 dB-compression point, and squeezing level. We found, that the TWPA can provide the nondegenerate gain of up to 25 dB over the bandwidth of more than 4 GHz. While this nondegenerate gain is lower as compared to the one of the JPA ($\approx 32\,\mathrm{dB}$), the bandwidth of the TWPA is considerably larger than the one of the JPA ($\approx 0.78\,\mathrm{MHz}$). Furthermore, we obtain a 1 dB-compression point of $P_{1\mathrm{dB}} \approx -100\,\mathrm{dBm}$ across the TWPA entire bandwidth at the gain of 25 dB. These properties make the TWPA extremely attractive for many applications, such as frequency-multiplexed readouts of qubits [77]. However, for a reasonable high gain of more than 10 dB, the current TWPA noise performance seems quite limited, adding more than 10 noise photons to the amplified signal. In the degenerate regime, we have achieved the maximum vacuum squeezing level of 3.7 dB with the purity of roughly 0.8 with the TWPA, which is considerably lower than the maximum squeezing levels obtained with the flux-driven JPA (7.4 dB). For future applications, the TWPA could also be used for generation of broadband two-mode squeezed states. This allows for generation of frequency-spaced multimode quantum-entangled states which can be employed for various quantum applications, such as continuous-variable quantum computing with cluster states [122], secure quantum communication [123], quantum illumination [124], or teleportation [37, 125].

On a more technical side, we have introduced and developed the novel concept of a two-dimensional Planck spectroscopy. It combines our standard PNCF measurement using a heatable attenuator with the simultaneous heating of the mixing chamber. This gives us the possibility to measure losses inside a closed cryogenic system at millikelvin temperatures *in-situ*. We have experimentally demonstrated that this method is capable of resolving losses of less than 0.1 dB.

Finally, we have introduced the cryogenic link connecting two dilution refrigerators spatially separated by 6.5 m. We have discussed various design choices used for this system and presented its performance with the related modifications. Here, we see that the cryogenic link performance is very similar to a single dilution refrigerator with regards to its cooldown times and minimal mixing chamber temperatures. The cryolink allows to cool down three superconducting coaxial cables to the temperatures below 100 mK, thus, forming a microwave quantum local area network (QLAN). These, nearly lossless, microwave connections allow us to directly transfer microwave quantum states between distant nodes without using any frequency conversion schemes. Here, we have performed transfer of microwave vacuum squeezed states across the cryolink. We have observed nearly identical squeezing levels and purities between the states measured locally, within one cryostat, and the states sent across the QLAN. Furthermore, we have been able to experimentally verify the fluctuation-dissipation theorem by studying the influence of a local QLAN heating on the quantum properties of the transmitted squeezed states. Finally, we have used the QLAN to distribute quantum entanglement between the distant fridges by sending balanced microwave two-mode squeezed states. Here, we have observed positive negativity values obtained by the join quantum tomography of two microwave modes measured from the outputs of these two fridges, signifying successful distribution of quantum entanglement.

All these results and observations establish the foundation for our future experiments towards studying technical and fundamental limits of microwave quantum communication. In particular, we consider further implementations of quantum microwave teleportation between the distant fridges and remote entanglement of superconducting qubits with squeezed light [142]. To this end, we plan to upgrade the cooling performance of the Alice fridge (and the cryolink) by installing extra heat exchangers and optimizing its superinsulation.

On longer timescales, one could envision an integration of the TWPA, the cryolink, and the remote entanglement of superconducting qubits into one large quantum network. Here, the TWPA could locally generate frequency-nondegenerate propagating two-mode squeezed states which can be distributed across the cryolink to a large number of spatially separated qubits. These two-mode squeezed states of light can then be used to drive these qubits into highly entangled states. This would allow us to implement remote gate operation protocols between spatially distributed qubits that then require classical communication only and bring us a step closer to implementing a true quantum internet [143].

Appendix A

Long term HEMT performance

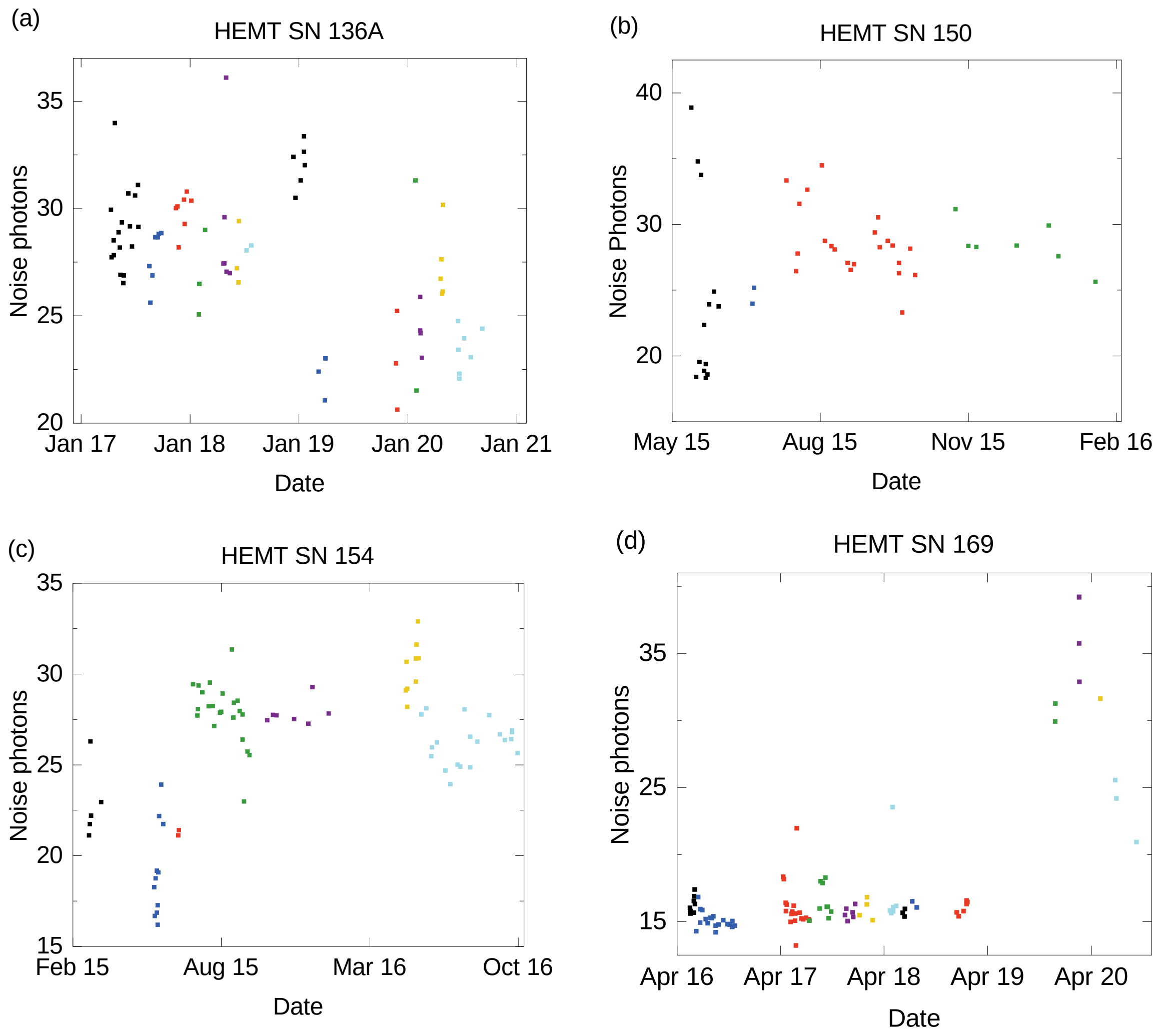

Figure A.1: Noise photons of the HEMTs with serial number 136A (a), 150 (b), 154 (c), and 169 (d) over an extended period of time. Each datapoint corresponds to one PNCF measurement and each change in color corresponds to a new cooldown.

Appendix B

Modifications to the cryolink

Overall, we have implemented three main modifications to the system. The first one, which also had the most impact on performance, was exchanging the Cryomech PT 410 PTR in the Alice cryostat for a more powerful Cryomech PT420 PTR. This lead to a nominal increase in cooling from 40 W to 55 W at 45 K on the PT1 stage and an increase from 1 W to 2 W at 4.2 K on the PT2 stage [144, 145]. The technical details regarding this modification can be found in the PhD thesis of M. Renger. Before this modification was performed, a stable operation of the cryolink could not be realized, as high temperatures permitted sustained dilution cooling. In order to remove the old coldhead, it was necessary to open some of the capillaries used for routing the ^{3}He/^{4}He mixture. We took this opportunity to install an copper radiation shield around the ^{3}He/^{4}He, 1K heat exchangers. A picture of the radiation shield can be seen in the background of Fig. B.2(b).

The second modification is adding 10 layer superinsulation to the PT1 stage at various locations of the system, that were not covered before. These include the seams between the PT1 shields of the cryostats, the blanks on the Eve cryostat (see Fig. B.1(c)) and the

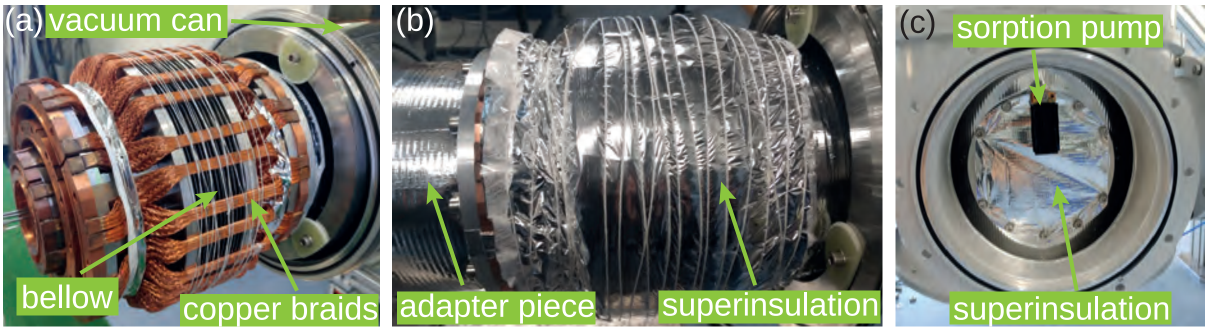

Figure B.1: Photographs of some of the modifications done to the cryolink. (a) We tie down the copper braids that are used to thermalize both sides of the stainless steel bellow on the PT1 stage to eliminate the possibility of a touch between the braids and the vacuum can. (b) Exposed parts of the PT1 stage are covered with a 10 layer superinsulation foil to minimize the heat load caused by thermal radiation from the vacuum can. (c) 10 layer superinsulation foil and sorption pumps are added to the blanks of the PT1 stage in Alice, Bob and Eve.

link arm underneath the sliding vacuum can (see Fig. B.1(b)). Here, the copper braids used to form a thermal connection between both sides of the stainless steel bellows are tied down first, to reduce the risk of a touch with the vacuum can. This touch would lead to a thermal short between the PT1 stage and the vacuum shield at room temperature. A photograph of the bellows being tied down using a wax rope can be seen in Fig. B.1(c). In regards of performance, the addition of the superinsulation manifests itself in lower temperatures reached both on the PT1 and the PT2 stage. On the PT2 stage, the temperature decreases by 0.3 K, highlighting the necessity to reduce thermal radiation from the OVC to the PT1 as much as possible.

Lastly, we added a total of five sorption pumps to the system. These pumps consist of activated charcoal pellets that are glued to a gold-plated OFHC copper rod using blue stycast[1]. We mix copper powder into the stycast to ensure a good thermal contact between the copper rod and the charcoal pellets. A picture of such a sorption pump can be seen in Fig. B.2(a). Figure B.2(b) shows the sorption pump mounted to the PT2 plate of the Alice cryostat. A copper mesh is used to protect the fragile pellets from crumbling while one is working on the cryostat. Four more of these pumps are installed on the PT1 plate and blank of the Alice cryostat and on the PT1 blanks of Bob and Eve (see Fig. B.1(c)). These pumps rely on cryosorption, the reversible binding of gas molecules by Van der Waals forces on sufficiently cold foreign substrates. As soon as a monolayer of gas has been formed, the subsequent molecules hit this monolayer and the process changes to cryocondensation. The lower binding energy of cryocondensation prevents a further growth of the condensate layer, which places a limit on capacity for adsorbed gases. However, the adsorbents used, such as activated charcoal, have a porous structure with very large specific surface areas of $1 \times 10^6\,\mathrm{m^2/kg}$ [146]. We see the need for these pumps, as we find that there accumulate gases inside the OVC amounting to a pressure of roughly 0.7 mbar after a cooldown of four weeks. Operating the system in various configurations (PTRs and dilution circuit running, PTRs running and dilution circuit evacuated, PTRs off and dilution circuit evacuated) after pumping down the OVC to the 1×10^{-2} mbar regime have all shown very similar amount of gas trapped inside the vacuum can. For all configurations, we have analyzed the accumulated gas with a leak detector[2] testing for ^{3}He and ^{4}He and by routing the gas through a cold trap placed inside a LN2 dewar. With only spurious amounts of Helium detected and gas accumulating in the cold trap for any of the configurations, this suggests that the gas is primarily atmospheric nitrogen and water vapour that is slowly being pulled through the O-rings of the vacuum shields from the ambient air surrounding the cryostat. While water vapour only contributes to a small percentage of the gases forming the ambient air at room temperature, the viton O-rings' permeation coefficient for water vapour is 4 times larger than that of Helium and more than a hundred times larger than that of nitrogen [147]. Preliminary calculations

[1] We use Stycast 2850FT, Loctite.
[2] We use QualiTest HLT 260, Pfeiffer.

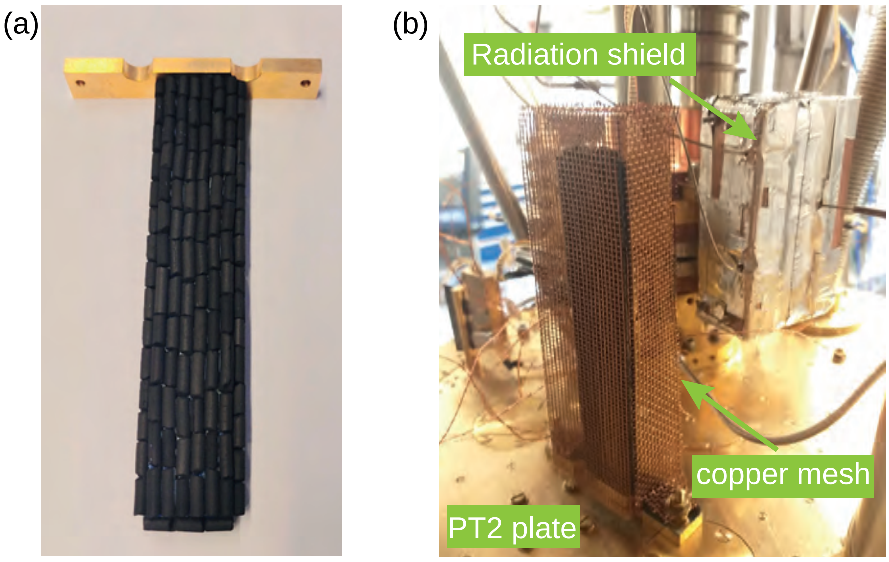

Figure B.2: (a) Photograph of the sorption pump consisting of active charcoal pellets glued to a gold-plated copper rod. (b) Photograph of the sorption pump mounted to the PT2 plate of the Alice cryostat. We install a copper mesh to protect the charcoal pellets. In the background the radiation shield containing the ^{3}He/^{4}He, 1K heat exchanger is visible.

by M. Renger have shown, that a film of LN2 or water forming on the superinsultation covering the PT1 stage can lead to the linear increase of PT1 and PT2 temperature with time that we have observed during our cooldowns. This is due to a change in the reflective properties of the superinsulation and a resulting increase in thermal load. Furthermore, this uptrend of roughly 1 mK/hr on the PT2 stage is also independent of the amount of superinsuation added to the system, which further supports this theory. Unfortunately, the charcoal sorbs do not significantly improve the temperature uptrend of the cryolink. Further testing is currently conducted to determine the characteristics of these charcoal sorption pumps.

Bibliography

[1] N. Gisin, G. Ribordy, W. Tittel & H. Zbinden. Quantum cryptography. *Reviews of Modern Physics* **74**, 145–195 (2002).

[2] N. Gisin & R. Thew. Quantum communication. *Nature Photonics* **1**, 165–171 (2007).

[3] M. H. Devoret & R. J. Schoelkopf. Superconducting circuits for quantum information: an outlook. *Science* **339**, 1169–1174 (2013).

[4] G. J. Mooney, C. D. Hill & L. C. L. Hollenberg. Entanglement in a 20-Qubit Superconducting Quantum Computer. *Scientific reports* **9**, 13465 (2019).

[5] S. Pogorzalek. *Remote State Preparation of Squeezed Microwave States*. PhD thesis, Technische Universität München, München (2020). URL `https://www.wmi.badw.de/fileadmin/WMI/Publications/Pogorzalek_Stefan_Doktorarbeit_2020.pdf`.

[6] K. G. Fedorov, M. Renger, S. Pogorzalek, R. Di Candia, Q. Chen, Y. Nojiri, K. Inomata, Y. Nakamura, M. Partanen, A. Marx, R. Gross & F. Deppe. Experimental quantum teleportation of propagating microwaves. *Science Advances* **7**, eabk0891 (2021).

[7] F. Fesquet. *Experimental implementation of a quantum key distribution with squeezed microwaves*. Master's thesis, Technische Universität München, München (2020). URL `https://www.wmi.badw.de/fileadmin/WMI/Publications/Fesquet_Florian_Masterarbeit_2020.pdf`.

[8] N. Calander, T. Claeson & S. Rudner. Shunted Josephson tunnel junctions: High–frequency, self–pumped low noise amplifiers. *Journal of Applied Physics* **53**, 5093–5103 (1982).

[9] B. Yurke, P. G. Kaminsky, R. E. Miller, E. A. Whittaker, A. D. Smith, A. H. Silver & R. W. Simon. Observation of 4.2-K equilibrium-noise squeezing via a Josephson-parametric amplifier. *Physical Review Letters* **60**, 764–767 (1988).

[10] Yurke, Corruccini, Kaminsky, Rupp, Smith, Silver, Simon & Whittaker. Observation of parametric amplification and deamplification in a Josephson parametric amplifier. *Physical review. A, General physics* **39**, 2519–2533 (1989).

[11] A. Blais, R.-S. Huang, A. Wallraff, S. M. Girvin & R. J. Schoelkopf. Cavity quantum electrodynamics for superconducting electrical circuits: An architecture for quantum computation. *Physical Review A* **69**, 062320 (2004).

[12] A. Wallraff, D. I. Schuster, A. Blais, L. Frunzio, R.-S. Huang, J. Majer, S. Kumar, S. M. Girvin & R. J. Schoelkopf. Strong coupling of a single photon to a superconducting qubit using circuit quantum electrodynamics. *Nature* **431**, 162–167 (2004).

[13] J. Koch, T. M. Yu, J. Gambetta, A. A. Houck, D. I. Schuster, J. Majer, A. Blais, M. H. Devoret, S. M. Girvin & R. J. Schoelkopf. Charge-insensitive qubit design derived from the Cooper pair box. *Physical Review A* **76**, 042319 (2007).

[14] T. Yamamoto, K. Inomata, M. Watanabe, K. Matsuba, T. Miyazaki, W. D. Oliver, Y. Nakamura & J. S. Tsai. Flux-driven Josephson parametric amplifier. *Applied Physics Letters* **93**, 042510 (2008).

[15] T. Ojanen & J. Salo. Possible scheme for on-chip element for squeezed microwave generation. *Physical Review B* **75** (2007).

[16] E. Jeffrey, D. Sank, J. Y. Mutus, T. C. White, J. Kelly, R. Barends, Y. Chen, Z. Chen, B. Chiaro, A. Dunsworth, A. Megrant, P. J. J. O'Malley, C. Neill, P. Roushan, A. Vainsencher, J. Wenner, A. N. Cleland & J. M. Martinis. Fast accurate state measurement with superconducting qubits. *Physical review letters* **112**, 190504 (2014).

[17] L. Zhong, E. P. Menzel, R. Di Candia, P. Eder, M. Ihmig, A. Baust, M. Haeberlein, E. Hoffmann, K. Inomata, T. Yamamoto, Y. Nakamura, E. Solano, F. Deppe, A. Marx & R. Gross. Squeezing with a flux-driven Josephson parametric amplifier. *New Journal of Physics* **15**, 125013 (2013).

[18] S. Pogorzalek, K. G. Fedorov, M. Xu, A. Parra-Rodriguez, M. Sanz, M. Fischer, E. Xie, K. Inomata, Y. Nakamura, E. Solano, A. Marx, F. Deppe & R. Gross. Secure quantum remote state preparation of squeezed microwave states. *Nature communications* **10**, 2604 (2019).

[19] M. Mariantoni, E. P. Menzel, F. Deppe, M. A. Araque Caballero, A. Baust, T. Niemczyk, E. Hoffmann, E. Solano, A. Marx & R. Gross. Planck spectroscopy and quantum noise of microwave beam splitters. *Physical Review Letters* **105**, 133601 (2010).

[20] Y. Cai, J. Roslund, G. Ferrini, F. Arzani, X. Xu, C. Fabre & N. Treps. Multimode entanglement in reconfigurable graph states using optical frequency combs. *Nature communications* **8**, 15645 (2017).

[21] G. K. White & J. G. Collins. Thermal expansion of copper, silver, and gold at low temperatures. *Journal of Low Temperature Physics* **7**, 43–75 (1972).

[22] S. Lloyd & S. L. Braunstein. Quantum Computation over Continuous Variables. *Physical Review Letters* **82**, 1784–1787 (1999).

[23] S. D. Bartlett & B. C. Sanders. Universal continuous-variable quantum computation: Requirement of optical nonlinearity for photon counting. *Physical Review A* **65** (2002).

[24] R. Yanagimoto, T. Onodera, E. Ng, L. G. Wright, P. L. McMahon & H. Mabuchi. Engineering a Kerr-Based Deterministic Cubic Phase Gate via Gaussian Operations. *Physical Review Letters* **124**, 240503 (2020).

[25] D. F. Walls & G. J. Milburn. *Quantum Optics* (Springer, Berlin and Heidelberg, 2010).

[26] W. Heisenberg. Über den anschaulichen Inhalt der quantentheoretischen Kinematik und Mechanik. *Zeitschrift für Physik* **43**, 172–198 (1927).

[27] E. Wigner. On the Quantum Correction For Thermodynamic Equilibrium. *Physical Review* **40**, 749–759 (1932).

[28] M. Hillery, R. F. O'Connell, M. O. Scully & E. P. Wigner. Distribution functions in physics: Fundamentals. *Physics Reports* **106**, 121–167 (1984).

[29] G. S. Agarwal & E. Wolf. Calculus for Functions of Noncommuting Operators and General Phase-Space Methods in Quantum Mechanics. II. Quantum Mechanics in Phase Space. *Physical Review D* **2**, 2187–2205 (1970).

[30] Buzek, Adam & Drobn. Quantum state reconstruction and detection of quantum coherences on different observation levels. *Physical Review A* **54**, 804–820 (1996).

[31] A. S. Holevo. *Statistical Structure of Quantum Theory*, Vol. 67 (Springer Berlin Heidelberg, Berlin, Heidelberg, 2001).

[32] S. L. Braunstein & P. van Loock. Quantum information with continuous variables. *Reviews of Modern Physics* **77**, 513–577 (2005).

[33] G. Adesso, S. Ragy & A. R. Lee. Continuous Variable Quantum Information: Gaussian States and Beyond. *Open Systems & Information Dynamics* **21**, 1440001 (2014).

[34] H. Nyquist. Thermal Agitation of Electric Charge in Conductors. *Physical Review* **32**, 110–113 (1928).

[35] C. Weedbrook, S. Pirandola, R. García-Patrón, N. J. Cerf, T. C. Ralph, J. H. Shapiro & S. Lloyd. Gaussian quantum information. *Reviews of Modern Physics* **84**, 621–669 (2012).

[36] A. Ferraro, S. Olivares & M. G. A. Paris. *Gaussian states in quantum information*, Vol. 8 of *Napoli series on physics and astrophysics* (Bibliopolis, Napoli, 2005).

[37] Furusawa, Sorensen, Braunstein, Fuchs, Kimble & Polzik. Unconditional quantum teleportation. *Science* **282**, 706–709 (1998).

[38] S. M. Barnett & P. L. Knight. Squeezing in Correlated Quantum Systems. *Journal of Modern Optics* **34**, 841–853 (1987).

[39] A. Einstein, B. Podolsky & N. Rosen. Can Quantum-Mechanical Description of Physical Reality Be Considered Complete? *Physical Review* **47**, 777–780 (1935).

[40] Peres. Separability Criterion for Density Matrices. *Physical Review Letters* **77**, 1413–1415 (1996).

[41] G. Adesso & F. Illuminati. Gaussian measures of entanglement versus negativities: Ordering of two-mode Gaussian states. *Physical Review A* **72**, 032334 (2005).

[42] A. Serafini, F. Illuminati & S. de Siena. Symplectic invariants, entropic measures and correlations of Gaussian states. *Journal of Physics B: Atomic, Molecular and Optical Physics* **37**, L21–L28 (2004).

[43] W. Meissner & R. Ochsenfeld. Ein neuer Effekt bei Eintritt der Supraleitfhigkeit. *Die Naturwissenschaften* **21**, 787–788 (1933).

[44] B. D. Josephson. Possible new effects in superconductive tunnelling. *Physics Letters* **1**, 251–253 (1962).

[45] E. Madelung. Eine anschauliche Deutung der Gleichung von Schrödinger. *Die Naturwissenschaften* **14**, 1004 (1926).

[46] E. Madelung. Quantentheorie in hydrodynamischer Form. *Zeitschrift für Physik* **40**, 322–326 (1927).

[47] R. Kleiner & W. Buckel. *Superconductivity: An Introduction* (Wiley-VCH, 2015).

[48] R. Gross & A. Marx. *Festkörperphysik*. Studium (De Gruyter, Berlin and Boston, 2014).

[49] M. Tinkham. *Introduction to Superconductivity* (McGraw-Hill Inc, New York, 1996).

[50] M. Sandberg, C. M. Wilson, F. Persson, T. Bauch, G. Johansson, V. Shumeiko, T. Duty & P. Delsing. Tuning the field in a microwave resonator faster than the photon lifetime. *Applied Physics Letters* **92**, 203501 (2008).

[51] B. Yurke & E. Buks. Performance of Cavity-Parametric Amplifiers, Employing Kerr Nonlinearites, in the Presence of Two-Photon Loss. *Journal of Lightwave Technology* **24**, 5054–5066 (2006).

[52] Y. Krupko, v. d. Nguyen, T. Weißl, É. Dumur, J. Puertas, R. Dassonneville, C. Naud, F. W. J. Hekking, D. M. Basko, O. Buisson, N. Roch & W. Hasch-Guichard. Kerr nonlinearity in a superconducting Josephson metamaterial. *Physical Review B* **98**, 094516 (2018).

[53] Mooij, Orlando, Levitov, Tian, C. H. van der Wal & Lloyd. Josephson persistent-current qubit. *Science* **285**, 1036–1039 (1999).

[54] C. H. van der Wal, A. C. ter Haar, F. K. Wilhelm, R. N. Schouten, C. J. Harmans, T. P. Orlando, S. Lloyd & J. E. Mooij. Quantum superposition of macroscopic persistent-current states. *Science* **290**, 773–777 (2000).

[55] V. E. Manucharyan, J. Koch, L. I. Glazman & M. H. Devoret. Fluxonium: single cooper-pair circuit free of charge offsets. *Science* **326**, 113–116 (2009).

[56] M. Perelshtein, K. Petrovnin, V. Vesterinen, S. H. Raja, I. Lilja, M. Will, A. Savin, S. Simbierowicz, R. Jabdaraghi, J. Lehtinen, L. Grönberg, J. Hassel, M. Prunnila, J. Govenius, S. Paraoanu & P. Hakonen. Broadband continuous variable entanglement generation using Kerr-free Josephson metamaterial. *arXiv* arXiv:2111.06145v1 (2021).

[57] N. E. Frattini, V. V. Sivak, A. Lingenfelter, S. Shankar & M. H. Devoret. Optimizing the Nonlinearity and Dissipation of a SNAIL Parametric Amplifier for Dynamic Range. *Physical Review Applied* **10**, 054020 (2018).

[58] K. G. Fedorov, L. Zhong, S. Pogorzalek, P. Eder, M. Fischer, J. Goetz, E. Xie, F. Wulschner, K. Inomata, T. Yamamoto, Y. Nakamura, R. Di Candia, U. Las Heras, M. Sanz, E. Solano, E. P. Menzel, F. Deppe, A. Marx & R. Gross. Displacement of Propagating Squeezed Microwave States. *Physical Review Letters* **117**, 020502 (2016).

[59] M. Renger, S. Pogorzalek, Q. Chen, Y. Nojiri, K. Inomata, Y. Nakamura, M. Partanen, A. Marx, R. Gross, F. Deppe & K. G. Fedorov. Beyond the standard quantum limit for parametric amplification of broadband signals. *npj Quantum Information* **7**, 160 (2021).

[60] M. Göppl, A. Fragner, M. Baur, R. Bianchetti, S. Filipp, J. M. Fink, P. J. Leek, G. Puebla, L. Steffen & A. Wallraff. Coplanar waveguide resonators for circuit quantum electrodynamics. *Journal of Applied Physics* **104**, 113904 (2008).

[61] D. M. Pozar. *Microwave engineering* (John Wiley & Sons Inc, Hoboken, NJ, 2012).

[62] S. Ramo, J. R. Whinnery & T. van Duzer. *Fields and waves in communication electronics* (Wiley, New York, 1994).

[63] M. R. Vissers, J. Gao, D. S. Wisbey, D. A. Hite, C. C. Tsuei, A. D. Corcoles, M. Steffen & D. P. Pappas. Low loss superconducting titanium nitride coplanar waveguide resonators. *Applied Physics Letters* **97**, 232509 (2010).

[64] Y. Yamamoto & K. Semba. *Principles and Methods of Quantum Information Technologies*, Vol. 911 (Springer Japan, Tokyo, 2016).

[65] M. Wallquist, V. S. Shumeiko & G. Wendin. Selective coupling of superconducting charge qubits mediated by a tunable stripline cavity. *Physical Review B* **74**, 224506 (2006).

[66] W. Wustmann & V. Shumeiko. Parametric resonance in tunable superconducting cavities. *Physical Review B* **87**, 184501 (2013).

[67] J. Bourassa, F. Beaudoin, J. M. Gambetta & A. Blais. Josephson-junction-embedded transmission-line resonators: From Kerr medium to in-line transmon. *Physical Review A* **86**, 013814 (2012).

[68] P. Bhupathi, P. Groszkowski, M. P. DeFeo, M. Ware, F. K. Wilhelm & B. L. T. Plourde. Transient Dynamics of a Superconducting Nonlinear Oscillator. *Physical Review Applied* **5**, 024002 (2016).

[69] A. A. Clerk, M. H. Devoret, S. M. Girvin, F. Marquardt & R. J. Schoelkopf. Introduction to quantum noise, measurement, and amplification. *Reviews of Modern Physics* **82**, 1155–1208 (2010).

[70] C. M. Caves. Quantum limits on noise in linear amplifiers. *Physical Review D* **26**, 1817–1839 (1982).

[71] H. A. Haus & J. A. Mullen. Quantum Noise in Linear Amplifiers. *Physical Review* **128**, 2407–2413 (1962).

[72] Movshovich, Yurke, Kaminsky, Smith, Silver, Simon & Schneider. Observation of zero-point noise squeezing via a Josephson-parametric amplifier. *Physical Review Letters* **65**, 1419–1422 (1990).

[73] X. Zhou, V. Schmitt, P. Bertet, D. Vion, W. Wustmann, V. Shumeiko & D. Esteve. High-gain weakly nonlinear flux-modulated Josephson parametric amplifier using a SQUID array. *Physical Review B* **89**, 214517 (2014).

[74] D. Arweiler. *Multi-SQUID Josephson Parametric Ampliers*. Master's thesis, Technische Universität München, München (2018). URL `https://www.wmi.badw.de/fileadmin/WMI/Publications/Arweiler%2CDaniel_Masterarbeit_2018.pdf`.

[75] M. A. Castellanos-Beltran, K. D. Irwin, G. C. Hilton, L. R. Vale & K. W. Lehnert. Amplification and squeezing of quantum noise with a tunable Josephson metamaterial. *Nature Physics* **4**, 929–931 (2008).

[76] L. Planat, R. Dassonneville, J. P. Martínez, F. Foroughi, O. Buisson, W. Hasch-Guichard, C. Naud, R. Vijay, K. Murch & N. Roch. Understanding the Saturation Power of Josephson Parametric Amplifiers Made from SQUID Arrays. *Physical Review Applied* **11**, 021021 (2019).

[77] J. Heinsoo, C. K. Andersen, A. Remm, S. Krinner, T. Walter, Y. Salathé, S. Gasparinetti, J.-C. Besse, A. Potočnik, A. Wallraff & C. Eichler. Rapid High-fidelity Multiplexed Readout of Superconducting Qubits. *Physical Review Applied* **10**, 034040 (2018).

[78] J. A. Armstrong, N. Bloembergen, J. Ducuing & P. S. Pershan. Interactions between Light Waves in a Nonlinear Dielectric. *Physical Review* **127**, 1918–1939 (1962).

[79] Kumar, Aytür & Huang. Squeezed-light generation with an incoherent pump. *Physical Review Letters* **64**, 1015–1018 (1990).

[80] C. Macklin, K. O'Brien, D. Hover, M. E. Schwartz, V. Bolkhovsky, X. Zhang, W. D. Oliver & I. Siddiqi. A near-quantum-limited Josephson traveling-wave parametric amplifier. *Science* **350**, 307–310 (2015).

[81] T. C. White, J. Y. Mutus, I.-C. Hoi, R. Barends, B. Campbell, Y. Chen, Z. Chen, B. Chiaro, A. Dunsworth, E. Jeffrey, J. Kelly, A. Megrant, C. Neill, P. J. J. O'Malley, P. Roushan, D. Sank, A. Vainsencher, J. Wenner, S. Chaudhuri, J. Gao & J. M. Martinis. Traveling wave parametric amplifier with Josephson junctions using minimal resonator phase matching. *Applied Physics Letters* **106**, 242601 (2015).

[82] A. L. Cullen. A Travelling-Wave Parametric Amplifier. *Nature* **181**, 332 (1958).

[83] P. K. Tien. Parametric Amplification and Frequency Mixing in Propagating Circuits. *Journal of Applied Physics* **29**, 1347–1357 (1958).

[84] B. Ho Eom, P. K. Day, H. G. LeDuc & J. Zmuidzinas. A wideband, low-noise superconducting amplifier with high dynamic range. *Nature Physics* **8**, 623–627 (2012).

[85] H. A. Haus. *Electromagnetic noise and quantum optical measurements: With 117 problems with 41 selected solutions*. Physics and astronomy online library (Springer, Berlin and Heidelberg, 2000).

[86] M. Houde, L. Govia & A. A. Clerk. Loss Asymmetries in Quantum Traveling-Wave Parametric Amplifiers. *Physical Review Applied* **12**, 034054 (2019).

[87] C. M. Caves & D. D. Crouch. Quantum wideband traveling-wave analysis of a degenerate parametric amplifier. *Journal of the Optical Society of America B* **4**, 1535 (1987).

[88] G. P. Agrawal. *Nonlinear fiber optics*. Optics and Photonics Ser (Academic Press, Amsterdam, 2013), 5th ed (online-ausg.) edn.

[89] A. B. Zorin. Josephson Traveling-Wave Parametric Amplifier with Three-Wave Mixing. *Physical Review Applied* **6**, 034006 (2016).

[90] K. O'Brien, C. Macklin, I. Siddiqi & X. Zhang. Resonant phase matching of Josephson junction traveling wave parametric amplifiers. *Physical Review Letters* **113**, 157001 (2014).

[91] A. L. Grimsmo & A. Blais. Squeezing and quantum state engineering with Josephson travelling wave amplifiers. *npj Quantum Information* **3**, 20 (2017).

[92] L. Planat, A. Ranadive, R. Dassonneville, J. Puertas Martínez, S. Léger, C. Naud, O. Buisson, W. Hasch-Guichard, D. M. Basko & N. Roch. Photonic-Crystal Josephson Traveling-Wave Parametric Amplifier. *Physical Review X* **10**, 021021 (2020).

[93] J. Y. Qiu, A. Grimsmo, K. Peng, B. Kannan, B. Lienhard, Y. Sung, P. Krantz, V. Bolkhovsky, G. Calusine, D. Kim, A. Melville, B. M. Niedzielski, J. Yoder, M. E. Schwartz, T. P. Orlando, I. Siddiqi, S. Gustavsson, K. P. O'Brien & W. D. Oliver. Broadband Squeezed Microwaves and Amplification with a Josephson Traveling-Wave Parametric Amplifier. *arXiv* arXiv:2201.11261v2 (2022).

[94] A. Ranadive, M. Esposito, L. Planat, E. Bonet, C. Naud, O. Buisson, W. Guichard & N. Roch. Kerr reversal in Josephson meta-material and traveling wave parametric amplification. *Nature communications* **13**, 1737 (2022).

[95] M. T. Bell & A. Samolov. Traveling-Wave Parametric Amplifier Based on a Chain of Coupled Asymmetric SQUIDs. *Physical Review Applied* **4**, 024014 (2015).

[96] M. Malnou, M. R. Vissers, J. D. Wheeler, J. Aumentado, J. Hubmayr, J. N. Ullom & J. Gao. Three-Wave Mixing Kinetic Inductance Traveling-Wave Amplifier with Near-Quantum-Limited Noise Performance. *PRX Quantum* **2**, 010302 (2021).

[97] K. Peng, M. Naghiloo, J. Wang, G. D. Cunningham, Y. Ye & K. P. O'Brien. Floquet-Mode Traveling-Wave Parametric Amplifiers. *PRX Quantum* **3**, 020306 (2022).

[98] T. Dixon, J. W. Dunstan, G. B. Long, J. M. Williams, P. J. Meeson & C. D. Shelly. Capturing Complex Behavior in Josephson Traveling-Wave Parametric Amplifiers. *Physical Review Applied* **14**, 034058 (2020).

[99] V. Vesterinen & S. Simbierowicz. Traveling wave parametric amplifier, PCT/FI2021/050283. URL `https://worldwide.espacenet.com/patent/search/family/075746653/publication/FI20205401A1?q=pn%3DFI20205401A1`.

[100] R. Desalvo, D. J. Hagan, M. Sheik-Bahae, G. Stegeman, E. W. van Stryland & H. Vanherzeele. Self-focusing and self-defocusing by cascaded second-order effects in KTP. *Optics Letters* **17**, 28–30 (1992).

[101] C. Eichler, D. Bozyigit, C. Lang, M. Baur, L. Steffen, J. M. Fink, S. Filipp & A. Wallraff. Observation of two-mode squeezing in the microwave frequency domain. *Physical Review Letters* **107**, 113601 (2011).

[102] C. Eichler, Y. Salathe, J. Mlynek, S. Schmidt & A. Wallraff. Quantum-limited amplification and entanglement in coupled nonlinear resonators. *Physical Review Letters* **113**, 110502 (2014).

[103] H. T. Friis. Noise Figures of Radio Receivers. *Proceedings of the IRE* **32**, 419–422 (1944).

[104] R. J. Glauber. The Quantum Theory of Optical Coherence. *Physical Review* **130**, 2529–2539 (1963).

[105] K. S. Kundert. Power Supply Noise Reduction. *Designer's Guide Community* (2004).

[106] S. Gandorfer. *Frequency-Degenerate Josephson Mixer Based on Josephson Parametric Amplifiers*. Bachelor's thesis, Technische Universität München, München (2020). URL `https://www.wmi.badw.de/fileadmin/WMI/Publications/thesis.pdf`.

[107] A. Marx, J. Hoess & K. Uhlig. Dry Dilution Refrigerator for Experiments on Quantum Effects in the Microwave Regime. *arXiv* arXiv:1412.3619 (2014).

[108] K. Uhlig. Dry dilution refrigerator with 4He-1K-loop. *Cryogenics* **66**, 6–12 (2015).

[109] R. Neagu. *FPGA-based Tomography of Propagating Quantum Microwaves*. Master's thesis, Technische Universität München, München (2019). URL https://www.wmi.badw.de/fileadmin/WMI/Publications/Neagu%2CRobert_Masterarbeit_2019.pdf.

[110] E. P. Menzel. *Propagating Quantum Microwaves: Dual-path State Reconstruction and Path Entanglement*. PhD thesis, Technische Universität München, München (2013). URL https://mediatum.ub.tum.de/doc/1177178/1177178.pdf.

[111] E. P. Menzel, R. Di Candia, F. Deppe, P. Eder, L. Zhong, M. Ihmig, M. Haeberlein, A. Baust, E. Hoffmann, D. Ballester, K. Inomata, T. Yamamoto, Y. Nakamura, E. Solano, A. Marx & R. Gross. Path entanglement of continuous-variable quantum microwaves. *Physical Review Letters* **109**, 250502 (2012).

[112] S. Boutin, D. M. Toyli, A. V. Venkatramani, A. W. Eddins, I. Siddiqi & A. Blais. Effect of Higher-Order Nonlinearities on Amplification and Squeezing in Josephson Parametric Amplifiers. *Physical Review Applied* **8**, 054030 (2017).

[113] B. A. Kochetov & A. Fedorov. Higher-order nonlinear effects in a Josephson parametric amplifier. *Physical Review B* **92**, 224304 (2015).

[114] L. Grönberg, M. Kiviranta, V. Vesterinen, J. Lehtinen, S. Simbierowicz, J. Luomahaara, M. Prunnila & J. Hassel. Side-wall spacer passivated sub- m m Josephson junction fabrication process. *Superconductor Science and Technology* **30**, 125016 (2017).

[115] J. Y. Mutus, T. C. White, R. Barends, Y. Chen, Z. Chen, B. Chiaro, A. Dunsworth, E. Jeffrey, J. Kelly, A. Megrant, C. Neill, P. J. J. O'Malley, P. Roushan, D. Sank, A. Vainsencher, J. Wenner, K. M. Sundqvist, A. N. Cleland & J. M. Martinis. Strong environmental coupling in a Josephson parametric amplifier. *Applied Physics Letters* **104**, 263513 (2014).

[116] Imran Mahboob, Hiraku Toida, Kousuke Kakuyanagi, Yasunobu Nakamura & Shiro Saito. A three-dimensional Josephson parametric amplifier. *Applied Physics Express* **15**, 062005 (2022).

[117] A. L. Cullen. Theory of the travelling-wave parametric amplifier. *Proceedings of the IEE Part B: Electronic and Communication Engineering* **107**, 101 (1960).

[118] G. Liu, T.-C. Chien, X. Cao, O. Lanes, E. Alpern, D. Pekker & M. Hatridge. Josephson parametric converter saturation and higher order effects. *Applied Physics Letters* **111**, 202603 (2017).

[119] C. W. Sandbo Chang, M. Simoen, J. Aumentado, C. Sabín, P. Forn-Díaz, A. M. Vadiraj, F. Quijandría, G. Johansson, I. Fuentes & C. M. Wilson. Generating Multimode Entangled Microwaves with a Superconducting Parametric Cavity. *Physical Review Applied* **10**, 044019 (2018).

[120] P. Lähteenmäki, G. S. Paraoanu, J. Hassel & P. J. Hakonen. Coherence and multimode correlations from vacuum fluctuations in a microwave superconducting cavity. *Nature communications* **7**, 12548 (2016).

[121] G. Vidal & R. F. Werner. Computable measure of entanglement. *Physical Review A* **65**, 032314 (2002).

[122] T. Hillmann, F. Quijandría, G. Johansson, A. Ferraro, S. Gasparinetti & G. Ferrini. Universal Gate Set for Continuous-Variable Quantum Computation with Microwave Circuits. *Physical Review Letters* **125**, 160501 (2020).

[123] E. Samsonov, R. Goncharov, A. Gaidash, A. Kozubov, V. Egorov & A. Gleim. Subcarrier wave continuous variable quantum key distribution with discrete modulation: mathematical model and finite-key analysis. *Scientific reports* **10**, 10034 (2020).

[124] N. Treps, U. Andersen, B. Buchler, P. K. Lam, A. Maître, H.-A. Bachor & C. Fabre. Surpassing the standard quantum limit for optical imaging using nonclassical multimode light. *Physical Review Letters* **88**, 203601 (2002).

[125] S. L. Braunstein & H. J. Kimble. Teleportation of Continuous Quantum Variables. *Physical Review Letters* **80**, 869–872 (1998).

[126] S. Barzanjeh, D. P. DiVincenzo & B. M. Terhal. Dispersive qubit measurement by interferometry with parametric amplifiers. *Physical Review B* **90**, 134515 (2014).

[127] N. Didier, A. Kamal, W. D. Oliver, A. Blais & A. A. Clerk. Heisenberg-Limited Qubit Read-Out with Two-Mode Squeezed Light. *Physical Review Letters* **115**, 093604 (2015).

[128] X. Guo, C. R. Breum, J. Borregaard, S. Izumi, M. V. Larsen, T. Gehring, M. Christandl, J. S. Neergaard-Nielsen & U. L. Andersen. Distributed quantum sensing in a continuous-variable entangled network. *Nature Physics* **16**, 281–284 (2020).

[129] S. Anton. *Magnetic flux noise in SQUIDs and qubits*. PhD thesis, University of California, Berkley (2013). URL `https://escholarship.org/content/qt5146t75k/qt5146t75k.pdf`.

[130] A. Roy & M. Devoret. Quantum-limited parametric amplification with Josephson circuits in the regime of pump depletion. *Physical Review B* **98**, 045405 (2018).

[131] S. Simbierowicz, V. Vesterinen, J. Milem, A. Lintunen, M. Oksanen, L. Roschier, L. Grönberg, J. Hassel, D. Gunnarsson & R. E. Lake. Characterizing cryogenic amplifiers with a matched temperature-variable noise source. *The Review of scientific instruments* **92**, 034708 (2021).

[132] P. Lähteenmäki, V. Vesterinen, J. Hassel, H. Seppä & P. Hakonen. Josephson junction microwave amplifier in self-organized noise compression mode. *Scientific reports* **2**, 276 (2012).

[133] S. Jebari, F. Blanchet, A. Grimm, D. Hazra, R. Albert, P. Joyez, D. Vion, D. Estève, F. Portier & M. Hofheinz. Near-quantum-limited amplification from inelastic Cooper-pair tunnelling. *Nature Electronics* **1**, 223–227 (2018).

[134] J. Y. Mutus, T. C. White, E. Jeffrey, D. Sank, R. Barends, J. Bochmann, Y. Chen, Z. Chen, B. Chiaro, A. Dunsworth, J. Kelly, A. Megrant, C. Neill, P. J. J. O'Malley, P. Roushan, A. Vainsencher, J. Wenner, I. Siddiqi, R. Vijay, A. N. Cleland & J. M. Martinis. Design and characterization of a lumped element single-ended superconducting microwave parametric amplifier with on-chip flux bias line. *Applied Physics Letters* **103**, 122602 (2013).

[135] S. Simbierowicz, V. Vesterinen, L. Grönberg, J. Lehtinen, M. Prunnila & J. Hassel. A flux-driven Josephson parametric amplifier for sub-GHz frequencies fabricated with side-wall passivated spacer junction technology. *Superconductor Science and Technology* **31**, 105001 (2018).

[136] L. Spietz, K. W. Lehnert, I. Siddiqi & R. J. Schoelkopf. Primary electronic thermometry using the shot noise of a tunnel junction. *Science* **300**, 1929–1932 (2003).

[137] L. Spietz, K. Irwin, M. Lee & J. Aumentado. Noise performance of lumped element direct current superconducting quantum interference device amplifiers in the 4–8 GHz range. *Applied Physics Letters* **97**, 142502 (2010).

[138] B. Kannan, D. L. Campbell, F. Vasconcelos, R. Winik, D. K. Kim, M. Kjaergaard, P. Krantz, A. Melville, B. M. Niedzielski, J. L. Yoder, T. P. Orlando, S. Gustavsson & W. D. Oliver. Generating spatially entangled itinerant photons with waveguide quantum electrodynamics. *Science Advances* **6**, eabb8780 (2020).

[139] M. Mirhosseini, E. Kim, X. Zhang, A. Sipahigil, P. B. Dieterle, A. J. Keller, A. Asenjo-Garcia, D. E. Chang & O. Painter. Cavity quantum electrodynamics with atom-like mirrors. *Nature* **569**, 692–697 (2019).

[140] E. Gottardi, G. Bianchini, I. Peroni, A. Peruzzi & G. Ventura. Thermal conductivity of Polyetheretherketone at low temperatures. *University of Florence* (2022).

[141] R. Kubo. The fluctuation-dissipation theorem. *Reports on Progress in Physics* **29**, 255–284 (1966).

[142] J. Agustí, Y. Minoguchi, J. M. Fink & P. Rabl. Long-distance distribution of qubit-qubit entanglement using Gaussian-correlated photonic beams. *Physical Review A* **105** (2022).

[143] S. Wehner, D. Elkouss & R. Hanson. Quantum internet: A vision for the road ahead. *Science* **362** (2018).

[144] Cryomech. PT410 - Cryomech. URL https://www.cryomech.com/products/pt410/ (26.02.2019).

[145] Cryomech. PT420 - Cryomech. URL https://www.cryomech.com/products/pt420/ (07.04.2022).

[146] W. Umrath. Grundlagen der Vakuumtechnik. URL https://www.leyboldproducts.de/media/pdf/10/0f/8b/FVT_Grundlagen_der_Vakuumtechnik_DE591eea2256c34.pdf (2016).

[147] P. Sturm, M. Leuenberger, C. Sirignano, R. E. M. Neubert, H. A. J. Meijer, R. Langenfelds, W. A. Brand & Y. Tohjima. Permeation of atmospheric gases through polymer O-rings used in flasks for air sampling. *Journal of Geophysical Research: Atmospheres* **109**, D04309 (2004).

Acknowledgments

This work would not have been possible without the help, knowledge, and support of many people accompanying me during the last year. In particular, I would like to thank:

Prof. Dr. Rudolf Gross for giving me the opportunity to complete my Master's thesis at the Walther-Meißner-Institut. His vast efforts invested in teaching the solid-state physics lecture and in the Ferienakademie inspired me at an early stage. His knowledge of physics is truly inspiring.

Dr. Kirill G. Fedorov for always encouraging me to search for new solutions on my own and to investigate every detail. The discussions about physical phenomena have remained very pleasantly in my memory. His numerous advices were particularly helpful for our experimental solutions. Especially his detailed corrections were a great help to me. I have gained a lot of valuable knowledge from him, not only about physics. Without him this work would not have become what it is.

Michael Renger for his never-ending endurance to answer my questions while simultaneously managing the cryolink and the teleportation experiment. I could always come to him for help and ideas. His dedication to the success of this project, work ethnic and intuition about physics was inspiring.

Dr. Achim Marx, Dr. Kurt Uhlig, and Sepp Höß for their technical advice. Without their help and vast cryogenic expertise, we would not have been able to get the cryolink to running condition.

William Yam for his support in the lab. He brought calmness to the lab, even during the most frustrating times.

Dr. Oscar Gargiulo for introducing me to the measurement setup in the Bob lab.

The team of the workshop for manufacturing the needed parts for the cryolink and their technical advice.

My office colleagues, *Michal Cherczynski*, *Alexander Jung*, *Christian Mang*, *Lukas Niekamp*, and *Franz Weidenhiller* and all the other master students for the productive working atmosphere and the interesting conversations.

My family, for their constant support and interest in my studies.

Finally, *Anna*, for her emotional support and helping me in stressful times. Thank you for your patience when I stayed late at WMI or started measurements during the night.